

**University of Alberta**

Optimization of Sodium MRI for the Human Knee at 4.7 Tesla

by

Alexander Watts

A thesis submitted to the Faculty of Graduate Studies and Research  
in partial fulfillment of the requirements for the degree of

Master of Science

Department of Biomedical Engineering  
Department of Electrical and Computer Engineering

©Alexander Watts  
Fall 2010  
Edmonton, Alberta

Permission is hereby granted to the University of Alberta Libraries to reproduce single copies of this thesis and to lend or sell such copies for private, scholarly or scientific research purposes only. Where the thesis is converted to, or otherwise made available in digital form, the University of Alberta will advise potential users of the thesis of these terms.

The author reserves all other publication and other rights in association with the copyright in the thesis and, except as herein before provided, neither the thesis nor any substantial portion thereof may be printed or otherwise reproduced in any material form whatsoever without the author's prior written permission.

## **Examining Committee**

Dr. Christian Beaulieu, Biomedical Engineering

Dr. Roger Zemp, Electrical and Computer Engineering,

Dr. Robert Lambert, Radiology, University of Alberta Hospital

Dr. Richard Thompson, Biomedical Engineering

**To my loved ones**

Dad

For always being there

Dana

For the long talks when things were tough

Graham

For all the laughs (may they never cease)

Lucy

For being my support, every moment of every day

Mom

For all your love

## ABSTRACT

Osteoarthritis is characterized by pain and inflammation in joints, typically weight-bearing joints such as the knee. An early warning sign of osteoarthritis is the loss of proteoglycan molecules in the cartilage matrix. A surrogate method for measuring proteoglycan loss is detection of sodium ions, which ionically bond to negatively charged glycosaminoglycan side chains. Sodium MRI has the potential to non-invasively measure proteoglycan content, and hence act as a diagnostic tool for osteoarthritis. However, as sodium MRI suffers from low sodium concentrations in vivo and reduced MR sensitivity compared to standard proton MRI, techniques are required which optimize signal. This thesis examines the hardware, software, and acquisition techniques required in order to achieve high resolution, excellent quality sodium MR images of the human knee in vivo, which has potential applications in early diagnosis as well as pharmacological treatment evaluations of osteoarthritis.

## ACKNOWLEDGEMENT

This project was funded by the Natural Sciences and Engineering Research Council (NSERC). I would also like to acknowledge the Alberta Ministry of Advanced Education and Technology, the Profiling Alberta's Graduate Students Award, the Queen Elizabeth II Graduate Scholarship: Master's Level, and the ISMRM Educational Student Stipend for helping with my funding.

In addition, I would like to gratefully acknowledge the contributions of the students and staff of the Department of Biomedical Engineering and the Peter Allen Center for the hours of help, advice, and support they have given me throughout my degree program. I would especially like to thank the following people:

Dr. Christian Beaulieu, my (excellent) advisor: Thanks for all your constructive support and advice, and for taking a chance on me as a student in the first place.

Dr. Rob Stobbe, my mentor and fellow sodium researcher: Words can't express how much you've helped me throughout the course of this research. Thanks for being an invaluable teacher, teammate, and friend.

Maisie Goh, our departmental administrator, and Benu Bawa, administrative assistant: Your help and friendship have been an incredible support to me throughout this program. Thank you.

Adrian Tsang, my office-mate and fellow sodium researcher: Thanks for being the best office-mate anyone could hope for, and for all your help and support along the way.

June Cheng-Baron and Kelvin Chow: Thanks to you both for the frequent pep-talks, without which my career (and life) might be quite different!

I can't possibly acknowledge how much everyone involved in my life has helped me during this degree, but your help and friendship has meant the world to me. You know who you are, thank you from the bottom of my heart!!

## Table of Contents

<b>1.</b>	<b>INTRODUCTION AND BACKGROUND</b>	<b>1</b>
<b>1.1</b>	<b>Thesis Introduction</b>	<b>1</b>
<b>1.2</b>	<b>Osteoarthritis</b>	<b>4</b>
<b>1.3</b>	<b>Cartilage</b>	<b>5</b>
1.3.1	Cartilage Structure	5
1.3.2	Cartilage Function	5
<b>1.4</b>	<b>Knee Anatomy</b>	<b>6</b>
<b>1.5</b>	<b>Sodium Concentrations in the Knee</b>	<b>7</b>
<b>1.6</b>	<b>Sodium in NMR</b>	<b>8</b>
1.6.1	Frequency of Resonance	8
1.6.2	Spin States of Sodium Nuclei	9
1.6.3	NMR Relaxation of Sodium	10
1.6.4	Relaxation and Spectral Density	13
<b>1.7</b>	<b>Sodium MRI as a Diagnostic Tool for OA in the Knee</b>	<b>14</b>
<b>1.8</b>	<b>Sodium MRI Acquisition Techniques</b>	<b>15</b>
1.8.1	Projection Imaging	16
1.8.2	Twisted Projection Imaging	17
1.8.3	Pulse Parameters and Tissue Sodium Concentration	19
1.8.4	Sodium MR Advantages at High Field and Specific Absorption Rate (SAR) Considerations	20
<b>1.9</b>	<b>Radiofrequency Coils</b>	<b>20</b>
1.9.1	Birdcage Coils	21
<b>1.10</b>	<b>Thesis Preview</b>	<b>24</b>
<b>2.</b>	<b>PRELIMINARY WORK: RELAXATION AND RF COILS</b>	<b>25</b>
<b>2.1</b>	<b>Introduction</b>	<b>25</b>

<b>2.2</b>	<b>Hardware and Software Specifications</b>	<b>25</b>
<b>2.3</b>	<b>RF Coil</b>	<b>25</b>
<b>2.4</b>	<b>Phantoms</b>	<b>30</b>
<b>2.5</b>	<b>Relaxation of Sodium in Knee Cartilage</b>	<b>33</b>
2.5.1	T1 Relaxation	34
2.5.2	T2 Relaxation	36
<b>2.6</b>	<b>Conclusion</b>	<b>39</b>
<b>3.</b>	<b>SIGNAL TO NOISE OPTIMIZATION FOR SODIUM MRI OF THE HUMAN KNEE AT 4.7 TESLA USING STEADY STATE</b>	<b>40</b>
<b>3.1</b>	<b>Introduction</b>	<b>40</b>
<b>3.2</b>	<b>Methods</b>	<b>42</b>
3.2.1	Simulations	42
3.2.2	Pulse Sequence Design	45
3.2.3	Phantoms	46
3.2.4	Experiments	47
3.2.5	Data Analysis	47
<b>3.3</b>	<b>Results</b>	<b>48</b>
3.3.1	Phantom Validation	48
3.3.2	Human Volunteers	48
<b>3.4</b>	<b>Discussion</b>	<b>50</b>
<b>3.5</b>	<b>Conclusions</b>	<b>55</b>
<b>4.</b>	<b>IMPROVED IN-PLANE RESOLUTION OF 3D TPI SODIUM MRI OF THE HUMAN KNEE USING ANISOTROPIC VOXELS</b>	<b>56</b>
<b>4.1</b>	<b>Introduction</b>	<b>56</b>

<b>4.2</b>	<b>Methods</b>	<b>58</b>
4.2.1	Projection Set Design	58
4.2.2	Phantoms	59
4.2.3	Experiment	61
4.2.4	Data Analysis	61
<b>4.3</b>	<b>Results</b>	<b>62</b>
4.3.1	Phantoms	62
4.3.2	Human Volunteers	63
<b>4.4</b>	<b>Discussion</b>	<b>63</b>
<b>4.5</b>	<b>Conclusions</b>	<b>67</b>
<b>5.</b>	<b>DISCUSSION AND CONCLUSIONS</b>	<b>68</b>
<b>5.1</b>	<b>Thesis Summary</b>	<b>68</b>
<b>5.2</b>	<b>Future Directions</b>	<b>71</b>
5.2.1	Concerning Relaxation	71
5.2.2	Concerning Dual-tuned Coils	72
5.2.3	Concerning PASS Optimization at 3T	74
5.2.5	Concerning Anisotropic Voxel Applications	74
<b>5.3</b>	<b>Final Commentary</b>	<b>75</b>
<b>6.</b>	<b>APPENDICES</b>	<b>76</b>
6.0	Appendix Preface	76
<b>6.1</b>	<b>Appendix 1: Projection Set Design and Construction Using NL-PRODS/AID</b>	<b>77</b>
<b>6.2</b>	<b>Appendix 2: Image Reconstruction Using TRICS/AIC</b>	<b>81</b>
<b>6.3</b>	<b>Appendix 3: Simulations Using Triple-S</b>	<b>83</b>
<b>6.4</b>	<b>Appendix 4: Simulation Display Using MARCONI</b>	<b>85</b>
<b>6.5</b>	<b>Appendix 5: ROI Analysis of Images Using Galileo</b>	<b>87</b>

## LIST OF FIGURES

1-1	Nucleus $3/2$ spin states relative to a polarizing $B_0$ field	9
1-2	Normalized transverse signal intensity decay due to relaxation	11
1-3	Normalized Z-axis magnetization recovery due to T1 relaxation	12
1-4	Example of the pulse sequence diagram for the twisted projection imaging sequence	18
1-5	Examples of TPI projections in k-space	19
1-6	A log-magnitude graph of the resonant frequencies of the single tuned sodium birdcage coil used in this thesis	22
1-7	Birdcage schematic diagrams	23
2-1	A simple series LC circuit diagram	26
2-2	A balun matching equivalent circuit diagram	28
2-3	A Smith chart displaying the method of measuring R	29
2-4	The single tuned sodium knee coil	29
2-5	Resolution phantom acrylic schematic diagram	30
2-6	The phantoms constructed during this thesis	32
2-7	Example ROI locations in inversion recovery experiments	33
2-8	T1 inversion recovery curves for sodium in the knee cartilage of two healthy volunteers	35
2-9	Least squares regression analysis of T2 relaxation data using a standard 60-40 biexponential model	37
2-10	Least squares regression analysis of T2 relaxation data using a modified 32-68 biexponential model	37
2-11	Images taken from the variable TE experiment	38
3-1	Simulations of sodium signal at 4.7T	43
3-2	Resolution phantom images for TSC and PASS parameter sets	46
3-3	ROI locations in sagittal viewing plane of sodium image	47

3-4	Sodium MRI of the knee: comparison of TSC and PASS images	49
3-5	Regional SNR values of PASS and TSC for knee cartilage	50
3-6	Percentage SNR benefit over all three cartilage regions for PASS over TSC in 10 healthy volunteers	50
3-7	Sodium images of the knee of a healthy volunteer at 4.7 T using the Na-PASS pulse sequence	53
3-8	Simulations of sodium signal in human cartilage at 3T and 7T	54
4-1	K-space projections for twisted projection imaging sodium MRI	58
4-2	Acquisition projections at various completion percentages of sampling of the top half of k-space	60
4-3	Resolution phantom images using the isotropic projection set and the anisotropic projection set	62
4-4	Sagittal sodium MR images of the human knee in vivo using the isotropic set and the anisotropic projection set	63
4-5	Sodium MR images of the human knee in vivo including out-of-plane reconstructions.	65
4.6	Sodium images of the knee of a healthy volunteer at 4.7 T using anisotropic voxels	66
5-1	Comparative sodium images of the human knee in vivo	69
5-2	The double tuned coil	72
5-3	Sodium images of knee cartilage using the concentric double tuned coil, and the single tuned coil	72
5-4	Proton image of the knee using the double-tuned coil	73
A-1	A screenshot of NL-PRODS	77
A-2	A screenshot of TRICS	81
A-3	A screenshot of Triple-S	83
A-4	A screenshot of MARCONI	85
A-5	A screenshot of GALILEO	87

## LIST OF TABLES

1-1	Literature relaxation times for sodium in cartilage	13
1-2	Previous research involving sodium MRI of the knee in-vivo	14
2-1	RF knee coil characteristics	28
2-2	Phantoms constructed during the course of this thesis	31
2-3	Signal intensity in the cartilage of two volunteers across a range of inversion times	34
2-4	Summary of signal intensity in knee cartilage of 3 healthy volunteers over a variety of scans with variable TE	36
2-5	T2 values of human cartilage based on a 32-68 fast-slow relaxation model	38
5-1	References, including voxel size, scan time, and field strength for the images displayed in Figure 5-1	70

## LIST OF SYMBOLS AND ABBREVIATIONS

AIC	Arbitrary Image Construction
AID	Arbitrary Image Development
FCD	Fixed Charge Density
FID	Free Induction Decay
$\gamma$	Gyromagnetic ratio
GAG	Glycosaminoglycan
GRE	Gradient echo
IR	Inversion Recovery
$J_0, J_1, J_2$	Spectral density parameters
$\mu$	Nuclear magnetic moment
MR	Magnetic Resonance
MRI	Magnetic Resonance Imaging
mT	Millitesla
mT/m	Millitesla/meter
$\mu$ s	Microsecond
NL-PRODS	Non-Linear Projection Design Software
NSAID	Non-Steroidal Anti-Inflammatory Drug
nH	Nanohenry
OA	Osteoarthritis
PASS	Projection Acquisition in the Steady State
PG	Proteoglycan molecules
pF	Picofarad
p	Twist: fraction of $K_{\max}$ covered radially in TPI
R	Resistance
RF	Radiofrequency
SDC	Sampling Density Compensation
SD	Sampling Density
SNR	Signal to Noise Ratio

TE	Echo time
TI	Inversion time
TKA	Total knee arthroplasty
TPI	Twisted Projection Imaging
TR	Repetition Time
TSC	Tissue Sodium Concentration
T1	Spin-lattice relaxation time constant
T2	Spin-spin relaxation time constant
T2 <sub>fast</sub>	Fast component of T2
T2 <sub>slow</sub>	Slow component of T2
Z	Impedance
2D	Two dimensional
3D	Three dimensional

# Chapter 1

## **Introduction and Background**

### **1.1 Thesis Introduction**

Osteoarthritis (OA) is a debilitating disorder whereby degradation and loss of articular cartilage in joints can result in swelling, reduced mobility, and pain. It is one of the most common reasons for disability in the United States (1), as well as being a common diagnosis amongst elderly patients visiting their primary care physician (2). The pain and reduced mobility from OA of the knee frequently have a serious adverse impact upon quality of life. Despite the prevalence and seriousness of OA, it remains incurable and difficult to treat. Pharmacological treatment options have historically been limited. The most common medication typically administered for symptom treatment is acetaminophen, followed in some cases by non-steroidal anti-inflammatory drugs (NSAID) (3). These medications reduce inflammation and pain, and ease of application (usually oral) makes them attractive to persons dealing with the affliction. However, these analgesics are a symptomatic treatment option only, and neither regenerate lost cartilage nor improve the lubricating and compressive qualities of any remaining cartilage. Some studies have found that the progression of osteoarthritis can be slowed by the application of medications with a possible structure-modifying effect (4), however a positive effect on cartilage regeneration has not been shown. Hence, early diagnosis is essential in order to make the lifestyle and activity changes which could slow the progression of the illness and reduce the need for symptomatic treatment with medications.

Early diagnosis is difficult, however. An irreversible stage of physiological deterioration can be reached before significant loss of collagen occurs. By the time a patient feels enough pain to contact a physician, changes to lifestyle and activity may have little effect. As such, a valid, non-invasive method of diagnosis would be significantly useful in both prevention and treatment of OA. Clinical proton MRI (1.5T) has been shown to be unreliable in the early

detection of OA (5-7). There are relatively small morphological changes such as a slight swelling, but variability in cartilage thickness between individuals makes conclusive diagnosis difficult. Proton MRI at 3 T has been shown to be better for diagnosis of mid to late stage osteoarthritis (when there are already lesions present) (8-9), however, 3T proton MRI has not yet been shown to provide an advantage over 1.5 T MRI in detecting OA in its earliest stages. Fortunately, there are some biochemical markers relating to the molecular structure of cartilage which can provide a clear indication of degradation even at the earliest stages of OA.

Cartilage in the knee is made up of about 70% water by mass, with collagen and a molecular 'matrix' of proteoglycans making up the rest (10). The loss of proteoglycan molecules has been demonstrated to correlate with the early stages of OA, before substantial collagen loss occurs (11). The proteoglycan molecules contain sulphide and phosphoryl residues known as glycosaminoglycans (GAG) which are negatively charged under physiological conditions, and attract sodium ions naturally present in the synovial fluid of the knee. Hence, there is a positive correlation between the amount of sodium present in the cartilage matrix, and the amount of proteoglycans present. Sodium magnetic resonance imaging (MRI) has been proposed and validated as a valid surrogate tool for evaluation of the fixed charge density (hence proteoglycan content) in both ex-vivo bovine cartilage tissue (12) and cartilage tissue in the human knee (13-14). It was suggested in the same works that sodium MRI can thus function as a valid surrogate for detection of OA in its early stages. A proton technique called dGEMRIC can be also be used to determine relative GAG content (15), however, dGEMRIC requires the injection of a contrast agent and a wait time of several minutes before imaging can commence. For these reasons, it is not patient-friendly, despite results indicating its efficacy in early detection of OA (16).

Unfortunately, sodium MRI suffers from several disadvantages which complicates its use in the clinical setting. Standard clinical MRI uses hydrogen atoms (also known as protons) to provide an MR 'visible' signal which can be

used to construct images of internal structures. Due to their presence in water and fat, protons are ubiquitous in the body, and this in combination with a high MR signal sensitivity results in an extremely high signal-to-noise ratio, which translates to high resolution images. Sodium is present in the body at far lower concentrations than protons; additionally, a lesser MR sensitivity and reduced gyromagnetic ratio combine to result in an MR signal that is about 22000 times weaker than is given by proton (17). This translates directly to a much lower SNR and low resolution images. In order to be of use clinically, sodium MR images must be of high enough quality that they could be of use in a clinical setting.

There are other complications of sodium MRI. The frequency of sodium MR (known as the Larmor frequency) is nearly a quarter that of proton. Due to this frequency difference, sodium MRI requires certain specialized hardware and software which complicates its use in a clinical setting. Hardware such as the radiofrequency (RF) coil, the RF amplifier, quarter-wavelength cabling, broadband synthesizers and quadrature hybrid splitters must be specifically designed in order to transmit and receive at this lower frequency. Most clinical scanning suites do not possess the hardware necessary for sodium MRI, which helps prevent its entry as a common clinical technique.

This work intends to focus on ways in which sodium images of the knee can be improved to the point where they may be of clinical use. A comprehensive system of acquisition and reconstruction, developed for human brain scanning using sodium MRI (18) is adapted for use scanning the human knee. Analysis of sodium MRI of the knee is developed. A specialized birdcage RF coil is designed and constructed for use in scanning sodium at 4.7 T. Optimization strategies are employed to maximize SNR, as well as selective voxel shape acquisition to ensure maximum voxel filling efficiency in the tissue. Extremely high quality images of the knee at very low resolutions ( $\sim 2.5 \text{ mm}^3$ ) are demonstrated.

Sodium MRI possesses extremely high potential in the study of osteoarthritis. In addition to the possibility of aiding in early diagnosis, sodium MRI could be used to evaluate the efficacy of new pharmacological alternatives upon the molecular state of the cartilage. The ability to quantitatively evaluate

cartilage health using a non-invasive method cannot be overstated. This work represents a significant step forward in the development of a practical method of imaging sodium in knee cartilage, and may be of significant use to physicians and researchers in the future.

## **1.2 Osteoarthritis**

Osteoarthritis (OA) is a common disease of the joints where by the cartilage tissue that cushions the bone-bone interface of joints becomes degraded. While early progression of the disease involves slight molecular alterations to the cartilage matrix, as the affliction progresses there is substantial loss of cartilage resulting in reduced cushioning and lubrication of the joint. This in turn results in pain and inflammation in the joint area. As the affliction progresses, substantial joint narrowing (reduction of the cartilage thickness between femur and tibia) occurs (19) and advanced cases may have direct bone on bone contact at joints (20). While cartilage is possibly the most visible tissue affected, there are also morphological changes to bone (especially at the joint interface), synovial capsule, ligaments, and muscle. Joint motion can be restricted, and pain may reduce mobility and quality of life for those affected.

Risk factors are thought to be systemic (such as ethnicity, gender, genetic, and nutritional) and local (such as obesity, muscle laxity, prior injuries, occupational factors, and developmental abnormalities) (21). While no pharmacological cure is known, in cases that are detected early enough, adaptation of lifestyle (including reduction of body weight, reduction of impact exercise such as running, and inclusion of medications) may help treat the symptoms.

Currently, the pharmacological treatment generally prescribed by physicians is acetaminophen followed in some cases by non-steroidal anti-inflammatory drugs (NSAID). These drugs reduce inflammation and pain, but have not been shown to regenerate cartilage (22). While health supplements such as glucosamine have been investigated as a treatment for osteoarthritis (4) they have also not been conclusively shown to affect cartilage regeneration (23).

Knee replacement surgeries, known as total knee arthroplasty (TKA) cap the femur and tibia bone ends with synthetic components, effectively replacing the cartilage tissue (24). TKA can substantially improve quality of life for subjects, but this improvement may be time-limited (25). In addition, substantial recovery times, fears of complications and anesthesia, and financial concerns may detract from TKA as an effective treatment option (26). Finally, in Canada, substantial wait times for arthroplasty (27) can complicate this as a treatment option.

### **1.3 Cartilage**

#### **1.3.1 Cartilage Structure**

Articular cartilage is basically an extracellular matrix (ECM) composed of type II collagen (15-20%), proteoglycan (PG) molecules (3-10%), and water (10). Within the ECM exist specialized maintenance cells known as chondrocytes, which maintain the various components of the ECM. Aggrecan, the most common PG molecule, is composed of a central protein core, to which side chains are attached. The side chains, known as glycosaminoglycans (GAG), are predominantly negatively charged under physiological conditions; electrostatic repulsion may form a significant part of the performance of cartilage under compression (12). This electrostatic force is also responsible for the external volume of cartilage; the GAG molecules repel and provide a stretching force which increases cartilage volume and allows additional water to enter the ECM. In addition, the negative fixed charge density (FCD) attributable to the GAG molecules attracts positively charged ions such as Na<sup>+</sup>, which then increase local water content through osmotic pressure (10). The importance of the presence of sodium ions for imaging in the knee will be further discussed later in this chapter.

#### **1.3.2 Cartilage Function**

Cartilage is generally found at the articulating termination of bones which are involved in joints. There, it acts to create a smooth surface upon which the joint can articulate. In addition to making joint movement smoother and easier, it

has some compressive qualities which act to reduce and distribute impacts to the knee from walking, running, or jumping (28). While collagen provides much of this compressive capability, the significant amount of water present as synovial fluid is also thought to contribute. The water content acts as a shock absorber; when under compression, some of the water is forced to exit through the various spaces in the cartilage matrix. This allows a controlled reduction in volume, and provides slow compression which helps distribute the force evenly. When the cartilage is no longer under compression, the matrix expands again, and water can flow back into the matrix to occupy its previous locations.

As mentioned above, the negative charge on the glycosaminoglycan side chains also attracts free sodium ions, which increase water pressure through osmosis. This increased osmotic pressure results in extra compressive properties in the cartilage. Loss of proteoglycan molecules occurs early in the progression of osteoarthritis, before the onset of large scale collagen loss (11). The loss of PG may have a multifaceted effect on cartilage utility, which include (a) reducing the negatively charged repulsive framework which is used to absorb shock, (b) reducing the size of the matrix which stores fluid that is used to reduce or redistribute force, and (c) lowering the negative fixed charge density (FCD) of the matrix. The reduced FCD results in reduced sodium ion concentration hence reduced osmotic pressure, which in turn reduces the ability of the cartilage to act as a shock absorber.

#### **1.4 Knee Anatomy**

The knee is a complex joint involving several major bones (28). The most important bones in the knee are the femur, the tibia, and the patella. The femur is the largest bone in the body; it runs from the hip joint down to the knee. The bottom (inferior termination) of the femur separates slightly into two separate domains known as condyles. The condyles are referred to as medial (closer to the centerline of the body—the inside of the knee) and lateral (farther from the centerline of the body—the outside of the knee), and are covered with a thin layer of articular cartilage.

There are two major bones in the leg below the knee, the tibia and the fibula. They run parallel to each other, from the foot up to the knee. However, the tibia is larger and more important to the weight bearing functions of the leg. The superior termination of the tibia is nearly flat and is also covered in a thin layer of articular cartilage. The knee joint, in its most basic simplification, is the sliding of the tibial articular cartilage over the femoral articular cartilage.

There are other important tissues in the knee joint. As the femoral condyles are curved, only a small portion of the femoral knee cartilage is touching the tibial cartilage at any given time. In a U-shape around the two circular contact pads are tough cartilaginous tissue known as menisci (meniscus in the singular). The menisci act to cushion the knee when it absorbs an impact, as well as to help prevent sideways sliding of the knee. They are composed of fibrocartilage, which is distinguished by structure and composition from articular cartilage. Other than this mention of their location and the distinction between the menisci and the articulating knee cartilage, this work will not further involve the menisci. A certain amount of fat is also present in the knee joint, generally anterior to the synovial capsule and just below (inferior) to the patella. The fat serves to protect the cartilage and tendons nearby and fill otherwise void spaces in the knee joint. Bursae, small sacs of synovial fluid present in most articulating joints, serve a lubricating and cushioning purpose.

Finally, the entire knee joint area is encapsulated by the synovial membrane. The function of the synovial membrane is to keep the synovial fluid (which lubricates the joint and provides some mechanical absorption capabilities) in the area of the articulating surfaces of the knee. In addition, the synovial membrane produces the synovial fluid.

## **1.5 Sodium Concentrations in the Knee**

Sodium in the knee is found at the highest concentration in the cartilage tissue itself. Typical healthy sodium concentrations in human articular knee cartilage in vivo are approximately 240-260 mM (29) and concentrations ranging from 200 to 390 mM have been found for excised bovine cartilage (30). Sodium

is also present in lower concentrations of ~40 mM in the synovial fluid (14). Sodium is also present in the muscle at concentration of approximately 30 mM (31). The high FCD of the cartilage matrix produces a charge gradient which attracts free sodium ions from the synovial fluid and/or surrounding muscle and adipose tissue.

## 1.6 Sodium in NMR

### 1.6.1 Frequency of Resonance

Sodium (also referred to here as  $^{23}\text{Na}$ ), as a atom whose nucleus contains 11 protons and 12 neutrons, produces a net nuclear magnetic moment  $\mu$ . This is a consequence of the odd number of protons, which prevents nucleonic pairing and avoids cancellation of the internal circulating currents which generate a magnetic moment (32). The  $^{23}\text{Na}$  atom is stable and is the only naturally occurring isotope. A critical parameter for MR is the gyromagnetic ratio  $\gamma$ .  $\gamma$  is a constant for any given nuclei, and is defined by the equation

$$\gamma = \frac{2\pi\mu}{\hbar} \quad [1-1]$$

where  $\mathbf{I}$  is spin angular momentum and  $\hbar$  is Planck's constant of  $6.63 \times 10^{-34}$  J-s. Implications of  $\mathbf{I}$  for sodium nuclei will be discussed later. The gyromagnetic ratio is critical to MR systems because the frequency of precession of the nuclear magnetic moment is related to it by the following equation

$$\omega_0 = \gamma B_0 \quad [1-2]$$

where  $\omega_0$  is the Larmor frequency (with units of radians/s) and  $B_0$  is static magnetic field strength in Tesla. The equation can be written equivalently as

$$f_0 = \gamma B_0 / 2\pi \quad [1-3]$$

For sodium,  $\gamma = 11.26 \text{ MHz/T}$ , so at 4.7 Tesla, the Larmor frequency of precession is 52.9 MHz (approximated to 53 MHz for convenience). This is the frequency of operation of all work presented in this thesis.

### 1.6.2 Spin States of Sodium Nuclei in $B_0$

Spin angular momentum  $\mathbf{I}$  is non-zero only for nuclei possessing non-zero magnetic moment  $\mu$ , and takes on integer or half-integer values from  $1/2$  to  $9/2$ . Sodium has a spin angular momentum of  $3/2$ . This means that the magnetic moments of sodium nuclei can exist in four states relative to a polarizing magnetic field,  $3/2$ ,  $1/2$ ,  $-1/2$ , and  $-3/2$  (Figure 1-1). The existence of these four states leads to the use of the term ‘quadrupolar’ to describe sodium in NMR systems. This is distinct from proton, which possesses only two spin states ( $1/2$  and  $-1/2$ ); the quadrupolar nature of sodium causes it to relax biexponentially at a much faster rate than proton.

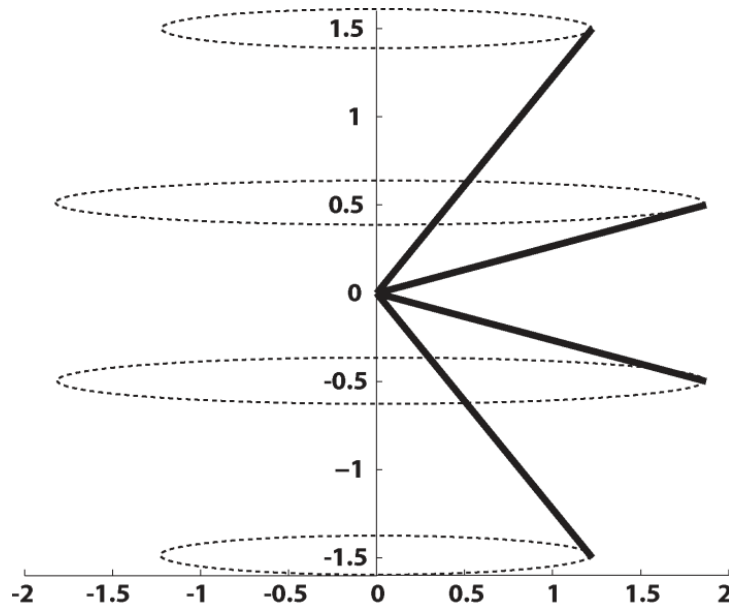


Figure 1-1: Nucleus  $3/2$  spin states relative to a polarizing  $B_0$  field (along the vertical axis). Reprinted with the permission of R. Stobbe (2010).

Signal in MRI comes from net alignment of more parallel spin states ( $3/2$ ,  $1/2$ ) than anti-parallel spin states ( $-1/2$ ,  $-3/2$ ). This net alignment occurs because

the parallel spin states are in a lower energy state than the anti-parallel states, and it is energetically favourable. Net magnetization (referred to here as  $M_z$ ) from the sum of the spin magnetic moments is aligned along the  $B_0$  field, and can provide a detectable MR signal when excited by a perpendicular  $B_1$  field.

### 1.6.3 NMR Relaxation of Sodium

Interactions with electric field gradients cause extremely rapid relaxation (both T1 and T2) in sodium nuclei. In addition, transverse relaxation in sodium in dense macromolecular environments is biexponential, with 60% of sodium signal represented by ‘fast’ relaxation, and 40% represented by ‘slow’ relaxation. Thus, signal  $S(t)$  changes due to T2 relaxation according to the relationship in equation 1-4.

$$S(t) \propto (0.6e^{-t/T2_{fast}} + 0.4e^{-t/T2_{slow}}) \quad [1-4]$$

This is a consequence of the effect that nearby ‘large’ macromolecules (such as GAG molecules in cartilage, or molecules in agarose gels) have upon the interaction of the sodium nuclei.  $T2_{fast}$  and  $T2_{slow}$  denote time constants for the fast and slow transverse relaxation processes, respectively, and  $S(t)$  represents the signal (from transverse magnetization) at time  $t$ . This biexponential relationship means that signal strength is highly dependent on echo time (TE); a choice of TE that is greater than  $T2_{fast}$  will result in high signal loss as much of the fast component (60%) will have dephased. Early sodium investigations with TE of several milliseconds (33) were unable to detect this fast component, however, the realization that biexponential relaxation was occurring as a result of interaction with electric field gradients had been made (34).

An example of the biexponential nature of T2 relaxation in cartilage can be viewed in Figure 1-2 below. Approximately 60% of the signal decays within 2 ms, but in the following 18 ms, the signal decays only about 35% more, to about 5% of its original value. Note that T2 relaxation when sodium is not influenced

by nearby macromolecular content (as in saline) closely follows monoexponential relaxation, typically with much longer T2 values (T2 ~ 60 ms at 4.7T).

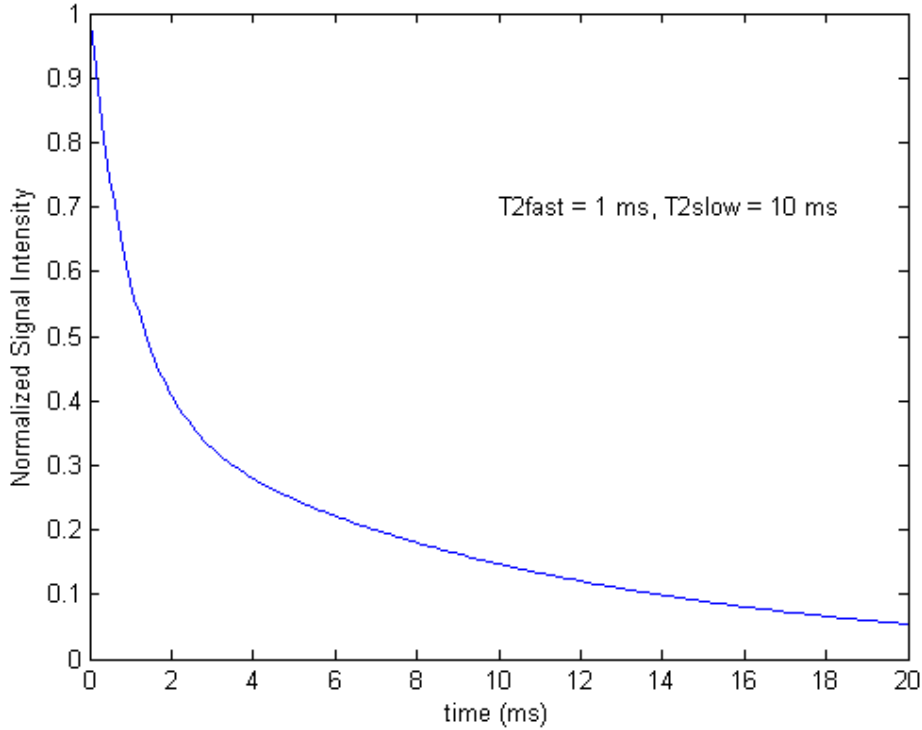


Figure 1-2: Normalized transverse signal intensity decay due to T2 relaxation

T1 relaxation is also biexponential according to the relationship in equation 1-5 (with only 20% of signal represented by a fast component, and 80% represented by a slow component).

$$M_z(t) \propto [1 - (0.2e^{-t/T1_{fast}} + 0.8e^{-t/T1_{slow}})] \quad [1-5]$$

$M_z(t)$  is the longitudinal magnetization (the magnetization in the direction of the main magnetic field that is available for the following excitation) at time  $t$ , and  $T1_{fast}$  and  $T1_{slow}$  are the time constants for the fast and slow longitudinal relaxation processes, respectively. The dominance of the slow component, which

represents 80% of the signal involved, means that the curve is, practically speaking, very similar to that denoted by the relationship

$$M_z(t) \propto [1 - (e^{-t/T_1})] \quad [1-6]$$

where  $T_1$  is the time constant of a monoexponential characterization of spin-lattice recovery.

The stronger slow component means that the relaxation properties are practically very similar to those characterized using a monoexponential relationship, as denoted in Figure 1-3.

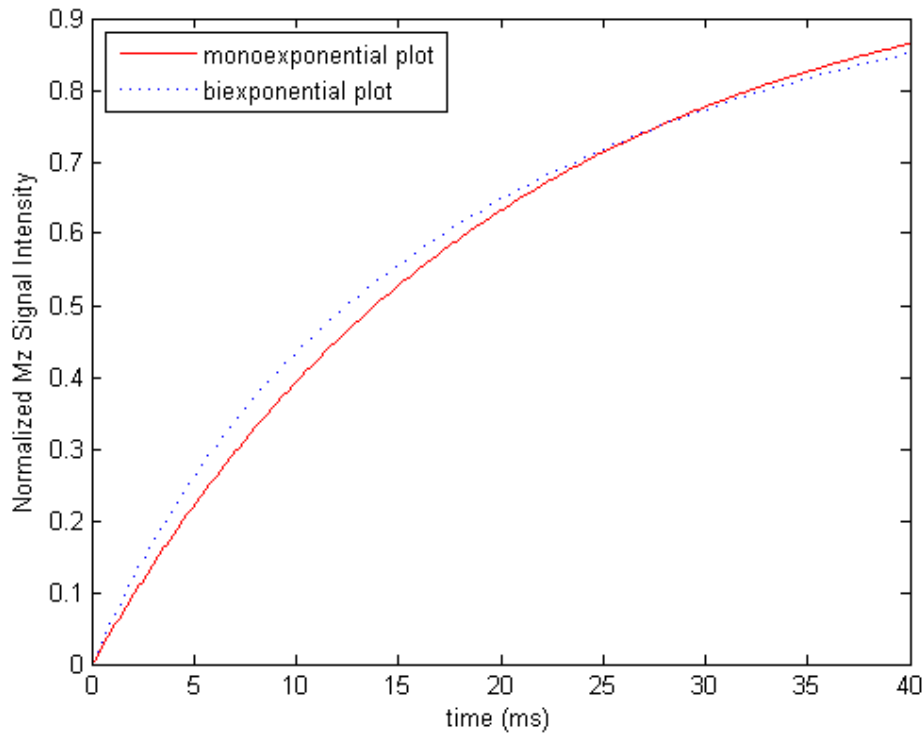


Figure 1-3: Normalized Z-axis magnetization recovery due to  $T_1$  relaxation. For the monoexponential plot,  $T_1=20$  ms was used, and for the biexponential plot,  $T_{1\text{fast}} = 6.3$  ms and  $T_{1\text{slow}} = 23.3$  ms was used.

As a result, sodium research often quantifies T1 relaxation using only one time constant, but quantifies T2 relaxation as a combination of the fast and slow time constants  $T2_{fast}$  and  $T2_{slow}$ .

Typical T1 relaxation values for field strengths of 2-7T range from 16-23 ms for sodium in excised bovine cartilage (14,30,35-38). Transverse relaxation (characterized by the time constant T2) is even more rapid. For excised bovine cartilage and at field strengths ranging from 2-4.7T,  $T2_{fast}$  has been found to range from 1.9 to 6 ms, while  $T2_{slow}$  has been found to range from 7.2 to 20 ms (30,36-38). For human cartilage in vivo, multiple quantum techniques at 2-3T have found  $T2_{fast}$  values ranging from 0.84-1 ms, and  $T2_{slow}$  values from 9.59-12 ms (39-40). These values are summarized in Table 1-1 below.

<b>Bo (T)</b>	<b>T1 (ms)</b>	<b>T2<sub>fast</sub> (ms)</b>	<b>T2<sub>slow</sub> (ms)</b>	<b>Sample</b>	<b>Reference</b>
4.7	17.4	6	20	Bovine, in vitro	Jelicks, 1993
2	n/a	1	12	Human, in vivo	Reddy, 1997
2	17.3	1.9	7.2	Bovine, in vitro	Insko, 1998
3	n/a	0.84	9.59	Human, in vivo	Borthakur, 1999
2	19.9	2.54	9.28	Bovine, in vitro	Shapiro, 2000
2	16	3.5	12.6	Bovine, in vitro	Borthakur, 2002

Table 1-1: Literature relaxation times for sodium in cartilage

#### 1.6.4 Relaxation and Spectral Density

While use of T1 and T2 parameters explains relaxation in an easily understood and classical way, relaxation can also be described through the solution of differential equations which model it as the effect of quadrupolar interactions of the sodium nucleus. For this, a spectral density model of the time-variant electric field gradients experienced by sodium nuclei can be used (41). In the spectral density model, the parameters  $J_0$ ,  $J_1$ , and  $J_2$  describe how signal power is related to frequency at 0 Hz, at  $\omega_0$ , and at  $2\omega_0$ , respectively. They are related to T1 (separated into biexponential components  $T1_{fast}$  and  $T1_{slow}$ ) and T2 (also separated into  $T2_{fast}$  and  $T2_{slow}$ ) by the following equations (18).

$$T1_{slow} = \frac{1}{2*J_2} \quad [1-7]$$

$$T1_{fast} = \frac{1}{2*J_1} \quad [1-8]$$

$$T2_{slow} = \frac{1}{J_1+J_2} \quad [1-9]$$

$$T2_{fast} = \frac{1}{J_0+J_1} \quad [1-10]$$

The spectral density model was used in the quantum mechanical simulations of sodium behavior discussed in Chapter 3, and is taken from earlier work modeling the behavior of 3/2 spin nuclei under electric field gradients (41-42).

### 1.7 Sodium MRI as a Diagnostic Tool for OA in the Knee

Sodium is the second most MR ‘useful’ nucleus after proton. The combination of relatively high concentrations of sodium in living creatures and relatively high MR sensitivity (compared to non-proton nuclei such as lithium (Li) and potassium (K)) in addition to the important role played by sodium in a

Reference	B <sub>0</sub> (T)	Voxel dimensions (mm)	Acquisition	Time
Granot (1988)	1.9	3.125*3.125*10	3D GRE	22 min
Reddy (1998)	4	1.25*2.5*4	3D GRE	10 min
Borthakur (1999)	3	4*4*4	TPI	10 min
Constantinides (2000)	1.5	6*6*6	TPI	16 min
Shapiro (2002)	4	0.75*3.125*6	3D GRE	30 min
Wheaton (2004)	4	0.6*2.4*3.8	3D GRE	22 min
Rong (2008)	7	4.7*4.7*20	2D FLASH-radial	1 min (1 slice)
Wang (2009)	7	1.5*1.5*1.5	radial PI	14 min
Staroswiecki (2010)	7	1*1*2	CONES	26 min

Table 1-2: Previous research involving sodium MRI of the knee in-vivo.

variety of biological processes in the body contribute to the attractiveness of sodium MRI as a non-invasive measurement method. It was used for the computation of FCD as early as 1992 (12), and suggested as a valid surrogate for OA in 1998 (13). Correlation between low cartilage signal intensity in sodium

MRI and depleted cartilage in osteoarthritic patients was demonstrated by Wheaton et al in 2004 (14), and sodium MRI of the knee in vivo has been demonstrated in multiple other investigations (29,31,35,43-44) (see Table 1-2). However, the relatively low SNR, long scan times, and extra hardware requirements such as RF coils and quadrature hybrids have hampered its inclusion in standard clinical MRI suites. As a result, sodium MRI has not yet ‘made the jump’ into mainstream diagnostic techniques. Optimizations which can result in excellent quality images would be beneficial in the transition of sodium MRI to mainstream clinical use.

## **1.8 Sodium MRI Acquisition Techniques**

As early as 1985, it was recognized that sodium MRI would benefit from 3D excitation pulses (45), whose ‘hard’ non-selective RF pulses reduce echo times compared to the longish sinc-shaped slice selective pulses used in 2D imaging. Much of the previous work imaging the knee in vivo using sodium has used a three dimensional gradient echo (3D GRE) approach (13-14,29,43). However, a gradient echo sequence is sub-optimal for sodium imaging due to the method in which k-space is acquired. The variable  $k$  is used to describe the accumulation of phase that a given spin or group of spins receive based on their location in real space. It is defined by the equation

$$k = \gamma \int G dt \quad [1-11]$$

where  $\gamma$  is the gyromagnetic ratio (in radians/T), and  $G$  is the applied gradient. In practical terms,  $k$  refers to the accumulation of phase through the application of gradients, and is proportional to the area under the gradient curve. In standard

‘Cartesian’ gradient echo techniques it is necessary to acquire k-space in a Cartesian manner (line by line), which implies the use of ‘rewind’ gradients in between excitation and readout in order to begin acquisition at the proper point in k-space. Since signal acquisition does not occur during the rewind gradients, they add an additional delay between the excitation of the RF pulse and readout. The rapid biexponential relaxation experienced by many sodium nuclei in biological environments makes any such unnecessary delay undesirable. As a result, k-space acquisition techniques which start readout at the center of k-space and do not require the application of rewind gradients are useful in sodium imaging.

### 1.8.1 Projection Imaging

Projection imaging (46-47) considers k-space as a sphere, and acquires it starting at the center and ending at a point in k-space some distance  $K_{\max}$  from the center. For straight radial imaging, the k trajectory travels in a straight line from the center to the outside edge of k-space. Previous work (18) has shown the sampling density (SD) required to properly (according to the Nyquist criterion) radially sample a spherical k-space volume as:

$$SD(r) \propto 1/r^2 \quad [1-12]$$

where  $r$  is a radial fraction of the maximum sampled k-space extent ( $r = 0$  at the center of k-space,  $r = 1$  at  $K_{\max}$ ). If undersampling at the edges of k-space is to be avoided, the sampling density at the edge of sampled k-space ( $r = 1$ ) must be equal to 1. This means that at any  $r$  value less than 1, SD will be greater than 1 (oversampling). Oversampling at the center of k-space, as occurs in radial projection imaging, is effectively equivalent to an increase in the standard deviation of noise; a method of k-space sampling that does not oversample at the center is desirable.

### 1.8.2 Twisted Projection Imaging

Cartesian k-space acquisition has uniform k-space sampling but negative refocusing gradients result in long TE and subsequent signal loss. Straight radial PI is capable of short TE, but effectively increases noise due to sampling inefficiencies. Twisted projection imaging (TPI) (48) was created as a compromise between these two options. It is based on a two dimensional twisted radial line (2D TWIRL) imaging (49), which in turn is based on the earlier techniques of purely radial projection imaging mentioned above. TPI begins with a ‘center-out’ radial trajectory. After a certain distance in k-space (normally designated as  $p$  (twist) —the ratio of the distance covered in a center-out trajectory to the maximum distance outwards in k-space), the k-space trajectory begins to follow a circular path with a steadily increasing radius (while maintaining a constant sampling rate). This is done so that the sampling density at any location greater than  $p$  is equal to the sampling density at  $p$ , according to equation 1-13 below (18,48).

$$SD(p) = 1/p^2 \quad [1-13]$$

For this sampling density to be maintained past  $p$ , it has been shown in the same works that projection evolution must follow equation 1-14.

$$r(\tau) = (3p^2\tau + p^3)^{1/3} \quad [1-14]$$

$\tau$  is a dimensionless fraction of the time required for a projection to reach  $K_{\max}$ . The TPI trajectory is created in the x and y planes by the application of an initial ‘rectangular’ gradient (for the radial center-out portion of the trajectory) followed by ‘sinusoidal’ gradients (for the twisting circular portion of the trajectory). The z-gradient also has an initial ‘rectangular component’, but once the evolution is twisted (with associated increase in projection length), the z-gradient must be reduced in order to maintain constant z-axis increase per unit

time. The pulse sequence diagram (see Figure 1-4) displays the pulse sequence used during most TPI acquisitions discussed in this thesis.

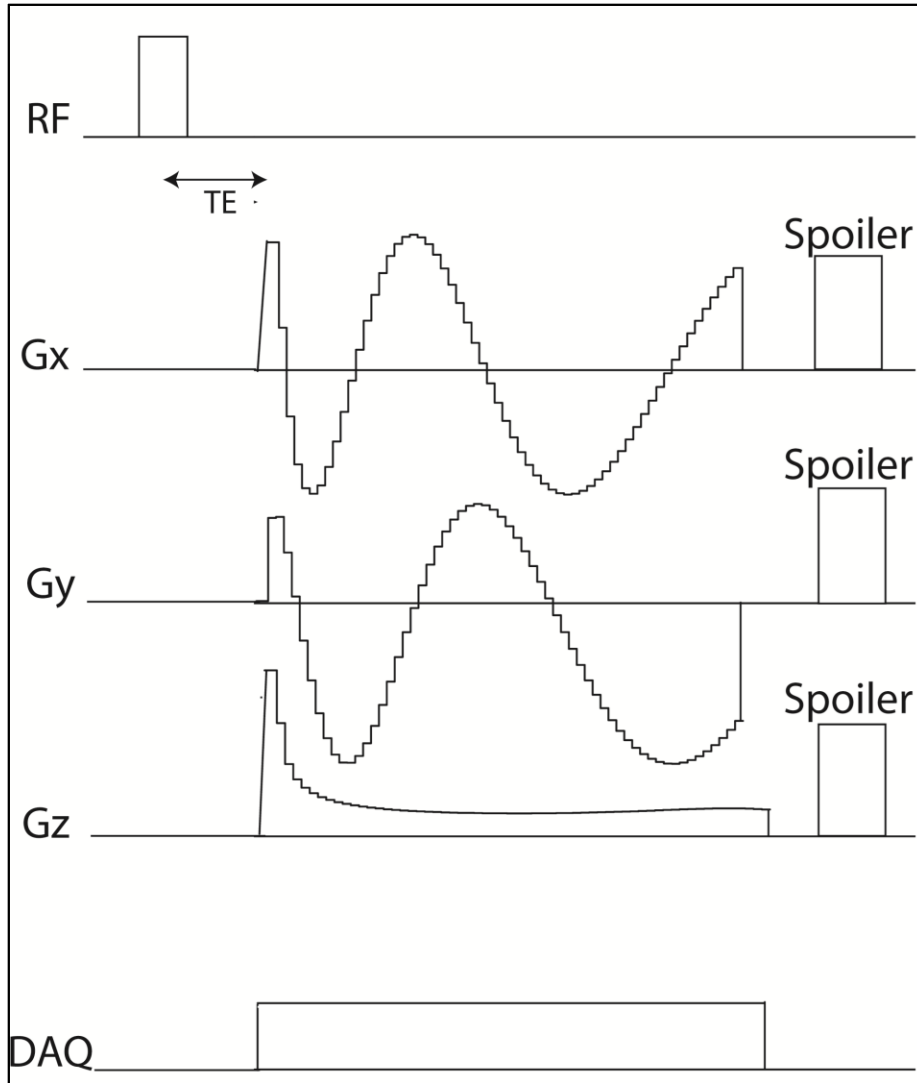


Figure 1-4: Example of the pulse sequence diagram for the twisted projection imaging used in this thesis. RF excitation is followed by a system delay, after which readout gradients follow a short radial trajectory before changing to the 'twisted' trajectory, which corresponds to the sinusoidal paths of the  $G_x$  and  $G_y$  gradients. After data acquisition (DAQ), the spins are spoiled (dephased) using spoiling gradients. Refocusing pulses (not shown here) are equal to the negative of the integral of the readout gradients and are applied simultaneously with the spoilers.

The k-space trajectories described above trace a series of cones, as described by Boda et al (1997) (48). Figure 1-5 shows an example of TPI projections.

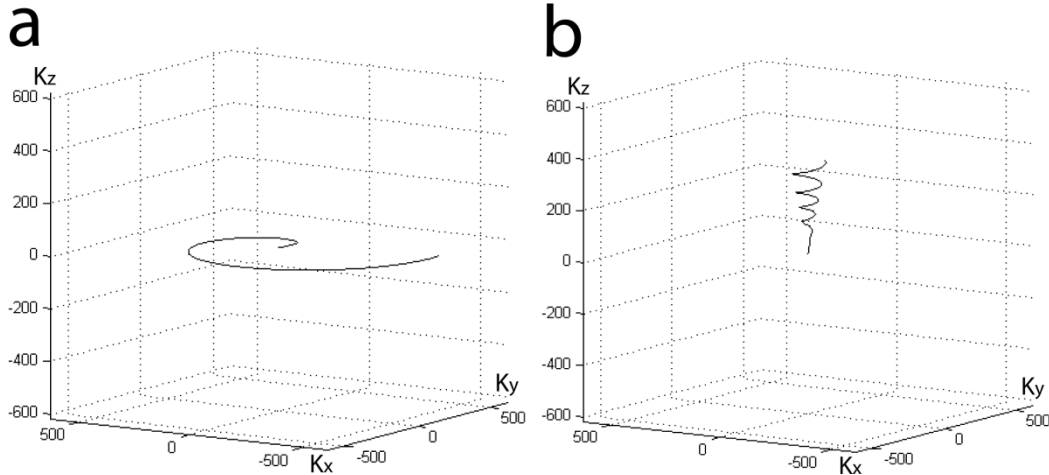


Figure 1-5: Examples of TPI projections in k-space. After a short radial component, the projection ‘twists’. (a) Initial acquisitions with no z component of evolution. (b) Later acquisitions trace out a vertical cone. As circumference increases (in the  $K_x$ - $K_y$  plane), the z-gradients must be reduced in order to accommodate ‘slowing’ of  $K_z$  coverage.

As TPI is a non-Cartesian imaging method, the free induction decays (FIDs) acquired during each projection acquisition must be regridded into standard rectilinear k-space. Then, the k-space volume can be divided into ‘virtual’ slices and the inverse Fourier transform can be applied in the same manner to achieve images. TPI is useful for sodium imaging, as it combines the short TE of radial imaging with relatively good sampling density, resulting in SNR benefits that can be traded for reduced imaging time or smaller voxels.

### 1.8.3 Pulse Parameters and Tissue Sodium Concentration (TSC)

Two of the most important parameters in any MRI protocol are echo time (TE) and repetition time (TR) (32). Echo time refers to the time in between excitation and acquisition; it is measured from the center of the RF pulse to the beginning of readout. TR refers to the time in between excitations. As different tissues have different relaxation times, alteration of TE and TR results in different

types of contrast in the tissue. For sodium, a common type of contrast is tissue sodium concentration (TSC). For this type of scan, TE is reduced to its minimum possible value, and TR is lengthened to avoid steady-state effects in the tissue of interest. In a TSC scan, relaxation weighting is minimized, and *only differences in sodium concentration* results in different contrast. Since quantification of sodium levels is of interest in many pathologies, this type of scan is common to sodium MRI, and has been used in sodium acquisitions of the knee (29,40,44).

#### **1.8.4 Sodium MR Advantages at High Field and Specific Absorption Rate (SAR) Considerations**

As discussed above, sodium suffers from poor signal to noise ratios compared to proton in MR systems. However, an increase in static magnetic field strength  $B_0$  results in increased signal and an improvement in SNR that is proportional to the increase in  $B_0$  (32). Sodium MRI benefits from scanning at higher field strengths, yet because its Larmor frequency is lower, does not suffer the same deleterious high frequency effects that affect proton MRI at high field. However, high field does have a constricting effect on sodium MR due to specific absorption rate (SAR). SAR is defined as the power absorbed (from an RF source) per mass of tissue; it has the units of watts per kilogram (50). SAR scales as to the square of  $B_0$  (51), and restricts the choice of parameters at high field, as discussed in Chapter 3.

#### **1.9 Radiofrequency Coils**

One of the key pieces of hardware in MRI is the radiofrequency (RF) coil. The coil is used both to transmit the RF excitation to the tissue and to receive the returning NMR signal. RF coils have progressed over the years from simple solenoids to saddle coils to birdcage and more complicated coils (52). However, the goal of all RF coils is basically the same: to act as a high efficiency antenna for both the transmission and reception of RF signal. In theory, the overall resistance  $R$  should be zero, the net impedance  $Z$  should be  $50 \Omega$  (in order to match with standard output impedance of transmission systems), and the

capacitive and inductive components of the coil should result in electric resonance at the desired frequency of use (in this case, the Larmor frequency of the nuclei being imaged). In practice however, the resistance  $R$  of the coil is never actually zero. Input impedance to the coil can be approximated to  $50 \Omega$ , but as this will vary according to the loading (experienced by the coil when placed on or near tissue), a constant value of  $50 \Omega$  is not practically possible. The coil can be treated as a simple RLC circuit, resistance can be ignored when  $R \ll \omega L$  (as is the case at operating frequencies of  $\sim 53$  MHz). In this case, resonant frequency can be predicted by the equation 1-15 below

$$\omega = \frac{1}{\sqrt{LC}} \quad [1-15]$$

While the coil may be tuned so that it resonates at the desired frequency, inequalities in the capacitive components and imbalances in the symmetry or inductive components will cause ‘spreading’ of the resonance valley. This means that effective transmission will be more inefficient than theoretical ‘perfect’ transmission. A measure of this is the quality factor  $Q$  as denoted in the following equation 1-16.

$$Q = \omega / \Delta\omega \quad [1-16]$$

Here,  $\omega$  is the resonant frequency in radians/s and  $\Delta\omega$  is the width between the edges of the resonant valley as defined by a loss of -3 dB (known as the full 3 dB bandwidth). As the  $Q$  value will change when sample matter is placed within it (due to dielectric effects and/or magnetically induced eddy currents), it must be measured for both loaded and unloaded conditions.

### 1.9.1 Birdcage Coils

Since its advent in 1985 by Hayes et al (53), the birdcage coil has become a mainstay of MR imaging. It boasts the advantages of high uniformity, a

transmission field  $B_1$  which is naturally perpendicular to the static magnetic field  $B_0$  when the coil is aligned with the magnet bore (as is convenient for most in vivo imaging), and the ability to be driven in quadrature, which has an SNR advantage of  $\sqrt{2}$  over non-quadrature capable coils. As is the case with most RF coils, it must be tuned to a specific frequency. In addition, the filling factor (defined as the volume inside the coil taken up by the object being imaged divided by the overall volume enclosed by the coil) of birdcage coils is poorer than surface coils. This is a consequence of the inability of the constant diameter birdcage to ‘scale down’ to smaller anatomical sizes. The poorer filling factor translates to lower SNR. An ideal situation would be to use a birdcage coil for transmission (excitation) and a surface coil or an array of surface coils for reception. This would allow the homogenous excitation of a birdcage coil while getting the SNR benefit of a surface coil. However, the use of a phased array as

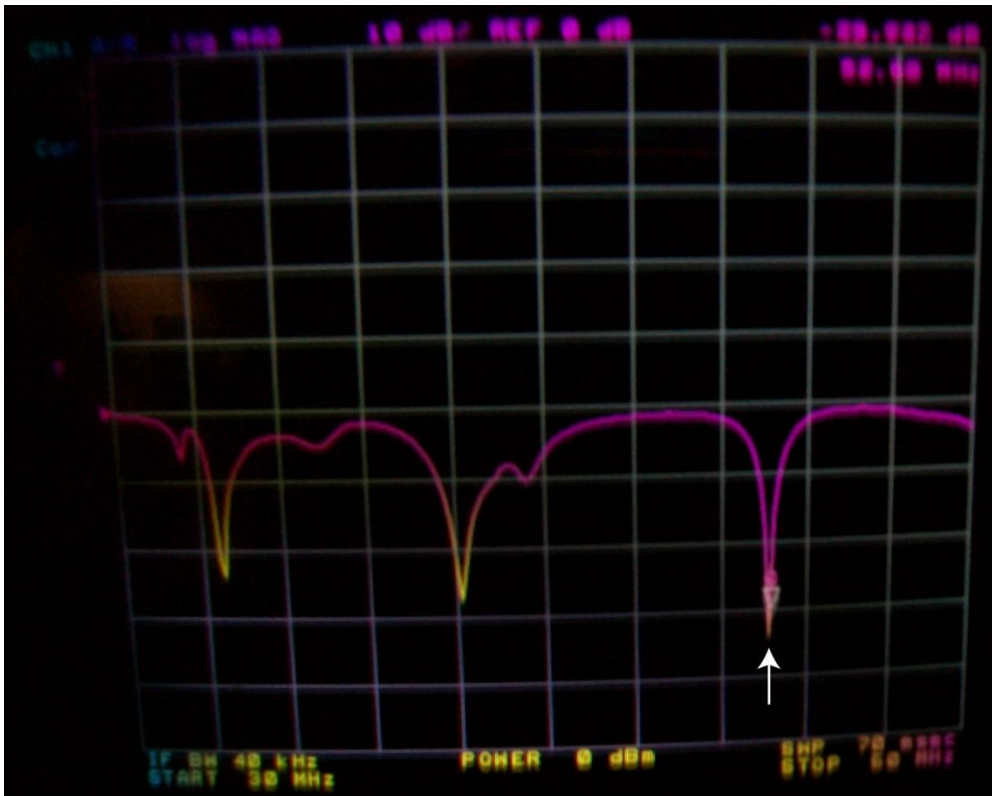


Figure 1-6: A log-magnitude graph of the resonant frequencies of the single tuned sodium birdcage coil used in this thesis. Mode number one (at right, indicated by the white triangle marker) is resonating at approximately 53 MHz.

described above requires expensive and difficult to implement circuitry such as pin diodes, and was not implemented during this thesis.

The various current paths available in a network such as a birdcage coil lead to various ‘modes’ of operation (54). End ring modes (where the current path runs through the end rings, with zero current in the legs) do not result in a useful electromagnetic field generated in the volume of the coil, and will not be discussed here. For a birdcage with  $N$  legs, the other modes (in which current runs in the legs) can range from  $k = 1$  to  $k = N/2$ , of which  $1 \leq k \leq N/2 - 1$  could be used for excitation. For MRI, the most useful mode is the  $k = 1$  mode, in which the endring currents are co-rotating and there are opposing currents in alternating legs of the coil. This mode is most homogenous, and therefore useful for excitation of signal in NMR systems. Several useful programs exist which can give a rough estimation of the operating frequency of a birdcage coil based on desired physical parameters such as number of legs, leg length and width, end ring length and width, diameter, etc. This thesis used Birdcage Builder (Penn State Hershey Medical Center, Hershey, PA). A picture of a log-magnitude graph of the frequency distributions in the birdcage coil used in this thesis is shown in figure 1-6.

The theory for construction of a single tuned birdcage resonator involves the treatment of the coil as an infinite network. It can be constructed (hence

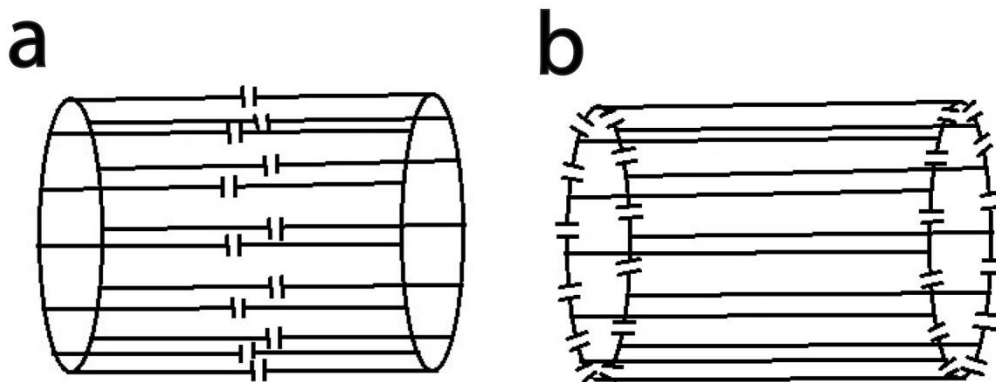


Figure 1-7: Birdcage schematic diagrams for (a) low pass configuration, and (b) high pass birdcage configuration.

analyzed) with the capacitive elements primarily in the legs (Figure 1-7a), which conforms under network transmission analysis to a low-pass filter configuration, or it can be constructed with the capacitive elements primarily in the end rings (Figure 1-7b), which conforms to a high-pass filter configuration. The types of birdcage are hence known as low-pass or high-pass depending on the placement of the capacitors. For the work of this thesis, a high-pass birdcage was used. The high pass design requires higher rung capacitances than a low-pass birdcage (for a given frequency), and both construction of the initial design and subsequent modification were easier when using the high-pass model.

### **1.10 Thesis Preview**

This thesis is composed of five chapters. Chapter 1 forms the introduction, which has attempted to give the background and some of the theory required to understand the work presented. Chapter 2 regards preliminary work involving RF coil building, phantom construction, and relaxation parameter measurements. Chapter 3 regards the optimization of sodium parameters under specific absorption rate constraints. It includes simulations and both phantom and human scanning. Chapter 4 investigates the benefits to anisotropic voxel acquisition in sodium MRI; both phantom and human scanning is conducted. Finally, Chapter 5 is the discussion and conclusion. The work of the thesis is summarized and discussed, and possible future directions are considered.

## Chapter 2

### Preliminary Work: Relaxation and RF Coils

#### 2.1 Introduction

Several preliminary undertakings were necessary in order to complete later work on the specific optimizations of SNR and resolution denoted in chapters 3 and 4. These included the construction of a suitable radiofrequency (RF) coil for the knee, construction of several phantoms for use during scanning, and measurement of the relaxation properties of the sodium of the cartilage of the knee.

#### 2.2 Hardware and Software Specifications

All image acquisitions in this thesis were performed on the 4.7 T magnet at the Peter Allen MR Research Center at the University of Alberta. The 4.7 T magnet uses a Varian Inova console; VnmrJ Version 1.1 (Revision D) was used for all acquisitions. The magnet possesses a gradient/shim set by Tesla Engineering (West Sussex, UK) with maximum gradient capabilities of 60 mT/m. The X, Y, Z and  $Z^2$  shim sets were predominantly used during scanning, up to maximum shim strengths of 0.25 mT. The RF amplifier was built by American Microwave Technology (currently owned by Herley, Lancaster, PA, USA) and has two transmit channels with maximum transmit strengths of 4 kW and 1 kW. Maximum slew rate used for acquisition was 120 mT/m/ms.

#### 2.3 RF Coil

As the primary excitation and reception antenna, the RF coil has a critical role in the acquisition of scans. Although the lab was already in possession of a functioning RF coil for operation at 52.9 MHz, this coil was sized for use in human brain scanning (diameter 28 cm, conductor leg length 18 cm). The filling factor and hence inherent performance of this coil for scanning the smaller anatomy of the knee was too poor for it to be considered as an option. As such,

an RF coil suitable for scanning of the knee was designed and built. A coil diameter of 17.8 cm was chosen. This diameter will fit most knees yet results in an acceptable filling factor. A conductor leg length of 10 cm was chosen since it gives adequate coverage of the entire knee region, including views of the full patellar, femoral, and tibial cartilage. Based on lab supplies of copper tape, an end ring width of 2.5 cm and a leg width of 1.25 cm was chosen.

Birdcage Builder (Penn State Hershey Medical Center, Hershey, PA) was used to find approximate capacitance values for a high-pass single-tuned 12 rung birdcage design at 53 MHz. The initial per rung capacitance value was 238 pF; this coil was constructed using capacitors from American Technical Ceramics (Huntington Station, NY, USA) already available in the laboratory. Capacitance values ranged from 2 pF to 220 pF, combinations of the capacitors in parallel resulted in the per rung capacitance of 238 pF. Subsequent testing of the coil in the magnet under loaded conditions resulted in a resonant frequency measurement of 53.1 MHz. This value is higher than the desired resonant frequency of 52.92 MHz.

As a result, the rung capacitance had to be increased in order to reduce the resonant frequency of the coil. As stated in the introduction, Section 1.9, the general equation for the resonant frequency of an LC circuit is

$$\omega = \frac{1}{\sqrt{LC_{series}}} \quad [2-1]$$

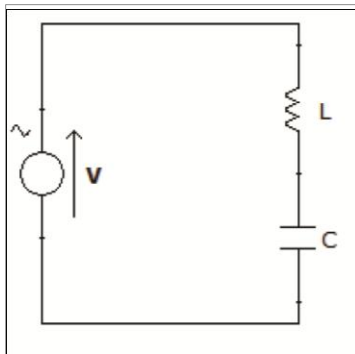


Figure 2-1: A simple series LC circuit diagram.

where  $\omega$  is angular frequency with units of radians/s, and is equal to  $2\pi f$ . However, this equation assumes the L and C are in series according to the circuit diagram in Figure 2-1.

A high pass birdcage coil equivalent circuit has parallel capacitive and inductive components (54). Thus, a rough equivalent circuit diagram for a 12 leg RF coil was developed. This equivalent circuit,

while simplistic in that it ignores the inductive impedance of the coil legs at high frequency, in addition to driving the coil from one port only instead of quadrature, was nevertheless found to fairly accurately predict the desired modifications to each rung capacitance  $C_{rung}$ . It assumes that each top end-ring capacitor is essentially in parallel with its corresponding bottom end-ring capacitor (basically assuming that the legs are short-circuiting). As such, each top and bottom capacitor can be combined into a parallel capacitance according to equation 2-2,

$$C_{parallel} = C_{top} + C_{bottom} = 2C_{rung} \quad [2-2]$$

assuming that  $C_{top} = C_{bottom} = C_{rung}$  (i.e. ignoring possible minor capacitance differences and accepting the manufacturers stated value). If this process is repeated for all the end-ring capacitance pairs, the equivalent circuit becomes a continuous circuit with 12 capacitances in series. These can be combined according to formula 2-3.

$$\frac{1}{C_{series}} = \frac{1}{C_{1parallel}} + \frac{1}{C_{2parallel}} + \dots + \frac{1}{C_{12parallel}} \quad [2-3]$$

Since  $C_{1parallel} = C_{2parallel} = \dots = C_{12parallel} = C_{parallel}$ , and each  $C_{parallel} = 2C_{rung}$ , this simplifies to equation 2-4.

$$\frac{1}{C_{series}} = \frac{12}{C_{parallel}} = \frac{6}{C_{rung}} \quad [2-4]$$

$C_{series}$  then represents the total equivalent capacitance of equation 2-1 above. Substitution and rearrangement for L results in equation 2-5.

$$L = \frac{6}{(2\pi f)^2 C_{rung}} \quad [2-5]$$

This equation, when solved using the *measured* frequency of resonance and the  $C_{\text{rung}}$  of the capacitors on the coil, results in the equivalent coil inductance  $L$ . Re-substitution of this  $L$  value into equation 2-1 above, this time using the *desired* resonant frequency, should result in a close approximation of the *desired*  $C_{\text{series}}$  value, from which the *desired*  $C_{\text{rung}}$  values can be calculated using equation 2-4.

Resonant frequency (MHz)	52.9
Diameter (cm)	17.8
Leg length (cm)	10
No of legs	12
QF (unloaded)	24
QF (loaded)	20

Table 2-1: RF knee coil characteristics

When this process was completed, it was found that the rung capacitance  $C_{\text{rung}}$  should be 240 pF. Changing capacitance to this value resulted in a coil which, when loaded and measured in the magnet, resonated at the desired frequency of 52.9 MHz. A summary of the pertinent characteristics of the coil is denoted in Table 2-1.

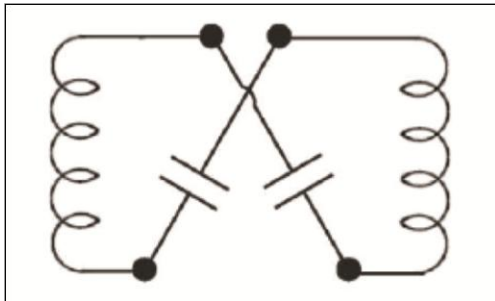


Figure 2-2: A Balun matching equivalent circuit diagram (reprinted courtesy of R. Stobbe)

The matching circuit used is the Balun circuit (55) shown in Figure 2-2.

Calculation of the  $L_{\text{balun}}$  and  $C_{\text{balun}}$  follows the formulae below.

$$Z_{\text{balun}} = \sqrt{50R} \quad [2-6]$$

$$L_{\text{balun}} = \frac{Z_{\text{balun}}}{j2\pi f} \quad [2-7]$$

$$C_{\text{balun}} = \frac{1}{j2\pi f Z_{\text{balun}}} \quad [2-8]$$

R is the resistance of the loaded coil. It is measured by finding the intercept of the coil curve with the purely resistive axis of the Smith Chart (Figure 2-3), and was found to be  $\sim 38 \Omega$ .  $j$  denotes the standard imaginary unit with the property  $j^2 = -1$ ; it is part of the mathematical formalism and was not used in the numerical calculations. The matching circuit allows the impedance of the coil to be close to the desired  $50 \Omega$ ; loaded impedances were measured at approximately  $70 \Omega$ .  $L_{\text{balun}}$  values of  $130 \text{ nH}$  and  $C_{\text{balun}}$  values of  $70 \text{ pF}$  were used.

Figure 2-3: A Smith chart displaying the method of measuring R. The point at which the coil curve crosses the horizontal axis (indicated by the white marker and arrow) gives the coil resistance value R ( $\sim 38 \Omega$ ).

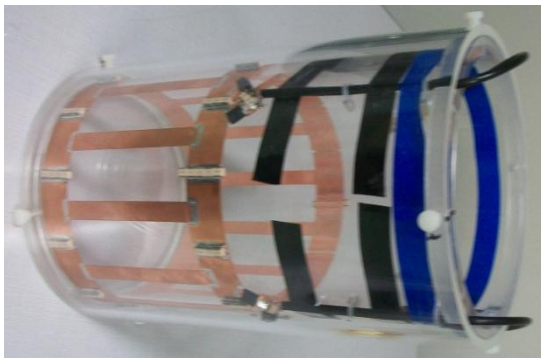
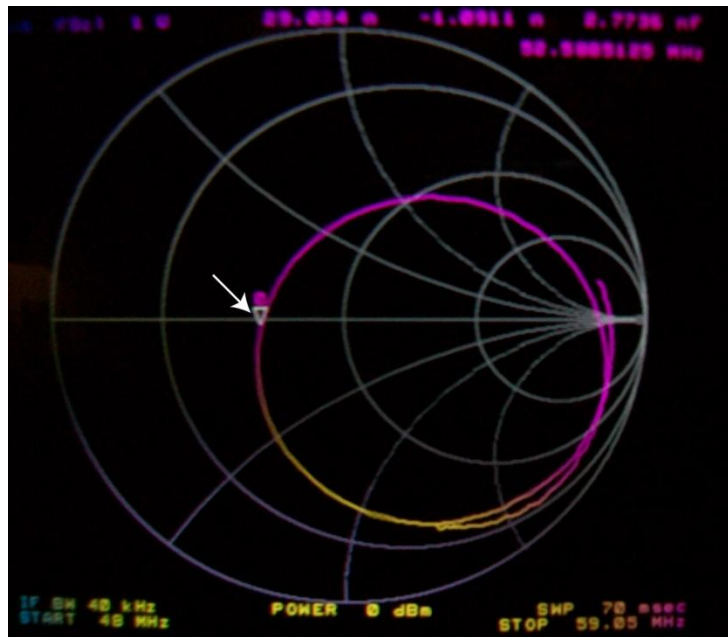


Figure 2-4: The single tuned sodium knee coil used for the bulk of scanning during this thesis.

Once the constructed coil was tested and found to be adequate, the electronics were enclosed in an additional layer of acrylic plastic, both to prevent

damage to the components and to preclude any possibility of subjects touching the electronics during scanning, which could have resulted in RF burns. A picture of the completed coil is shown in Figure 2-4.

## 2.4 Phantoms

Several phantoms were constructed during the course of this research. The first, and most widely used, was a resolution phantom used to ensure correct reconstruction of images and to determine effective spatial resolution of each projection set. The resolution phantom was constructed by drilling sequential sets of holes in a piece of acrylic plastic. The spacing (edge to edge) between the holes of each set was equivalent to their diameter (Figure 2-5).

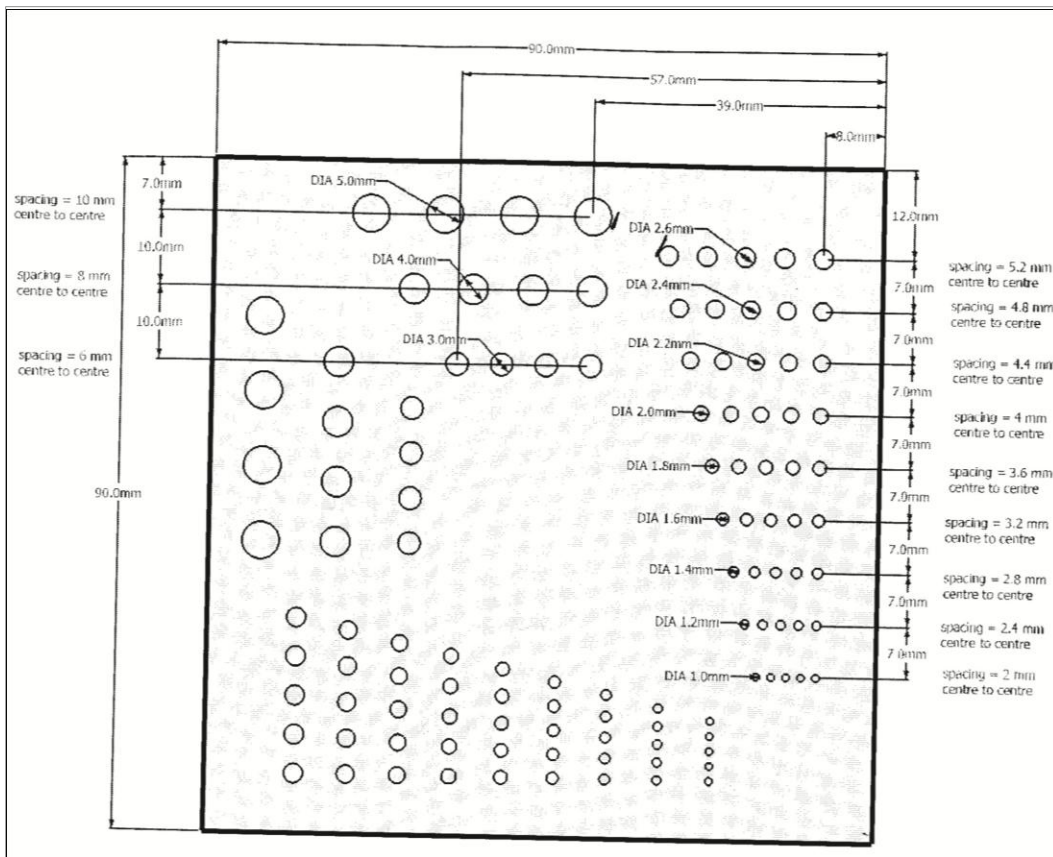


Figure 2-5: Resolution phantom acrylic schematic diagram. For convenience, hole diameters and spacing are shown only for half of the holes.

Hole spacing/diameters were as follows: 5 mm, 4 mm, 3 mm, 2.6 mm, 2.4 mm, 2.2 mm, 2.0 mm, 1.8 mm, 1.6 mm, 1.4 mm, 1.2 mm, and 1.0 mm. The acrylic was placed inside a bottle so that the acrylic face was perpendicular to the long axis of the bottle. The bottle was then filled with saline at 250 mM and bubbles were removed from the holes before the top was sealed with a cap. A picture of the resolution phantom is shown in Figure 2-6 along with the uniform spherical phantom and the quantification phantoms. All phantoms used in this thesis are listed in Table 2-2.

Name	Use	Construction	Concentration
Resolution Phantom	To ensure correct reconstruction during testing; to determine effective resolution of projection sets	Acrylic piece glued in the center of a 2L plastic bottle, then filled with saline	250 mM
Uniform Spherical Phantom	To determine relative SNR relationships between projection sets	~5 cm diameter glass sphere, filled with saline	500 mM
Quantification Phantoms	To be placed adjacent to the knee and used as known sodium reference values during scanning	Eight 2mL Eppendorf tubes, filled with agar (10%) and saline	150, 200, 250, and 300 mM

Table 2-2: Phantoms constructed during the course of this thesis.

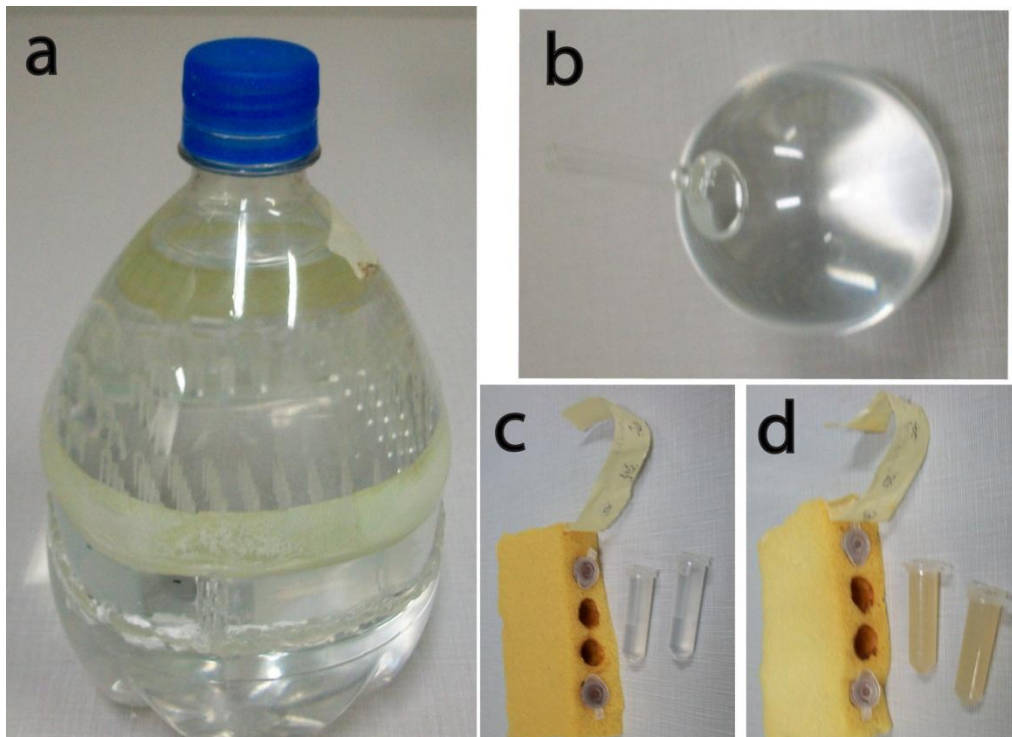


Figure 2-6: The phantoms constructed during this thesis were (a) the resolution phantom, (b) the uniform spherical phantom, (c) saline quantification phantoms, and (d) agar (10%) quantification phantoms.

A uniform spherical saline phantom was constructed in order to test SNR equivalence between projection sets with equivalent voxel sizes (see Chapter 4). A glass sphere (diameter ~5 cm) was filled with saline at 500 mM. The top of the sphere was covered with several layers of tape, which were then secured with more layers of tape. However, surface tension of the water at the top of the sphere acted to prevent loss of fluid through leakage; the tape acted as a barrier to evaporation.

Several small cylindrical phantoms were constructed from Eppendorf tubes (2 mL). These phantoms were made of both saline and agar (10%) at concentrations of 150 mM, 200 mM, 250 mM, and 300 mM. They were intended to be placed alongside the knee during in vivo scans in order to be able to quantify

the sodium content of the knee. While development has not yet reached this stage, they could certainly be put to this purpose in the future.

## 2.5 Relaxation of Sodium in Knee Cartilage

As previously discussed, sodium in knee cartilage follows biexponential relaxation in the T2 domain, and can be considered to follow monoexponential relaxation in the T1 domain. In both domains, relaxation is extremely fast. While relaxation of sodium in cartilage has been studied by other investigations (30,36-40,56), few of these measured it in vivo in the knee (39-40,56), and in those cases only T2 relaxation was studied. To the best of the author's knowledge, T1 of sodium in cartilage of the knee has not previously been measured in vivo. In addition, only one of the above investigations (non-human) was conducted at a field strength of 4.7 Tesla (38). T1 especially is affected by static magnetic field strength, and both T1 and T2 are affected by their molecular environments. As the T1 and T2 relaxation values are critical to the imaging parameter optimization carried out in Chapter 3, it was desirable to measure these in vivo at 4.7 Tesla.

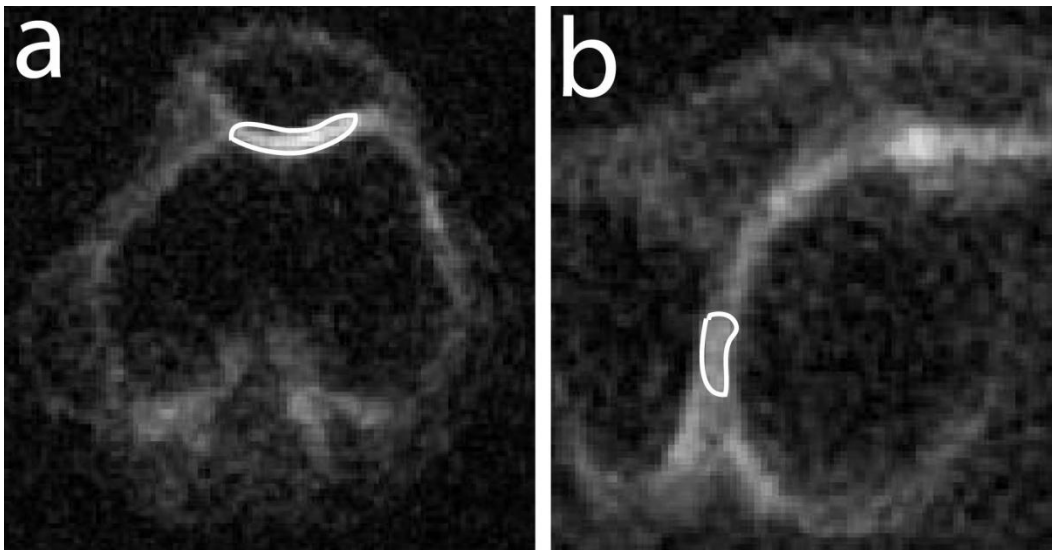


Figure 2-7: Example ROI locations in inversion recovery experiments to determine T1 of sodium in cartilage for (a) volunteer #1 (axial acquisition), and (b) volunteer #2 (sagittal acquisition). Both of these images were acquired for a TI = 70 ms.

### 2.5.1 T1 Relaxation

T1 was measured using an inversion recovery (IR) sequence. A hard 180° pulse (duration 5 ms) was applied in order to invert the sodium magnetization in the knee cartilage. After a defined inversion time TI, which ranged from 3-70 ms, a 90° excitation pulse (duration 0.4 ms) was applied to rotate the partially recovered z-magnetization into the transverse plane. After a specific system delay of 60 μs, readout began, and was carried out for the readout time of 12.95 ms. TR was adjusted so that there was a constant delay of ~100 ms after the 90° pulse (before the next 180° pulse). This ensured no differences due to changes in steady state weighting.

This experiment was conducted on two healthy male volunteers, aged 30 and 31. ROI were drawn in the visible cartilage (Figure 2-7) and mean signal was calculated as the average signal intensity of the pixels inside. A summary of the experimental data from all six acquisitions and for both volunteers is included in Table 2-3. Note that the signal intensities of the magnetizations at TI = 3 and 7 ms are negative to indicate the negative z-magnetization from which the signal derives; addition of the negative sign was done manually as the images showed magnitude data only. The projection set had a nominal resolution of 1.5 x 1.5 x 6 mm<sup>3</sup> and TE = 0.261 ms. Due to the variable TR, scan time for each acquisition ranged from 5-8.5 minutes, for a total acquisition time of approximately 38 minutes.

TI (ms)	TR (ms)	Volunteer #1 Signal Intensity	Volunteer #2 Signal Intensity
3	103	-101.1	-76.4
7	107	-45.9	-36.8
15	115	42.6	28.7
25	125	96.9	81.4
40	140	147.1	113.1
70	170	187.9	140.6

Table 2-3: Signal intensity in the cartilage of two volunteers across a range of inversion times.

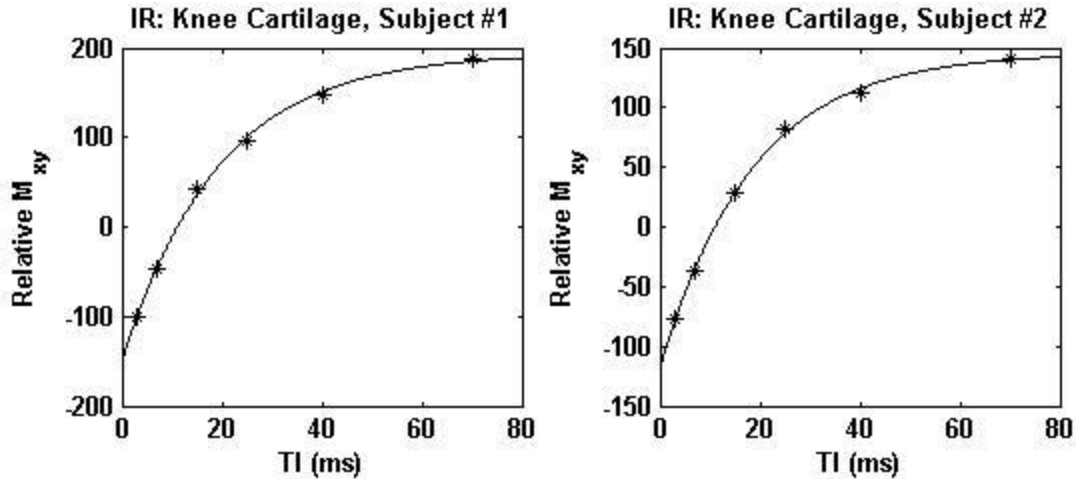


Figure 2-8: T1 Inversion Recovery curves for sodium in the knee cartilage of two healthy volunteers.

The experimental data was fitted using a regression least squares analysis, with a monoexponential model. This fitting resulted in a T1 ( $\pm$  95% regression confidence interval) of  $19.3 \pm 3.7$  ms for sodium in the knee cartilage of a healthy volunteer, aged 30. A T1 value of  $18.4 \pm 2.8$  ms was found in the same experiment on a second healthy volunteer, aged 31. The data and the fitting curves are shown below in Figure 2-7. The curves seem to demonstrate incomplete inversion; this may or may not be true. Inversion may seem to be incomplete if the estimated inversion time (ranging here from 3 to 70 ms) is not close enough to the actual inversion time. In that case, the magnetization at TI = 0 does not truly represent the fully inverted magnetization, but rather the magnetization at some point after the true zero.

If there is indeed incomplete inversion, it may be due to error in calculating the  $180^\circ$  flip angle. It may also be due to inhomogeneity across the excitation profile of the sample, which would result in some spins being ‘overflipped’ and some being ‘underflipped’, resulting in a net inverted magnetization which is less than the fully recovered magnetization. However, none of these factors should have affected measurement of the T1 constant. The value of approximately 19 ms is close to those found for bovine cartilage by other research (14,30,36-38), whose T1 values ranged from 16-23 ms.

### 2.5.2 T2 Relaxation

Several attempts were made to measure T2 relaxation of sodium in knee cartilage in vivo. Note that due to the relative insignificance of static inhomogeneities compared to dephasing from electric field gradients of sodium nuclei, T2\* can be approximated as T2. For measurement, a variable TE sequence was used, where hard excitation pulse was applied to flip the magnetization into the transverse plane. The system delay between excitation and readout was varied (effectively changing TE) in order to allow variable amounts of T2 decay before acquisition of signal. Readout length was 12.95 ms. As the ‘best’ data points for a T2 experiment were unknown, TE values were changed between experiments in an effort to find the points which would best characterize relaxation. A summary is located in Table 2-4.

TE (ms)	Subject #1	Subject #2	Subject #3
0.261	146.9	137	148
0.512			133
0.761		132	125.6
0.951	120		
1.261		127	
1.471			113.1
1.551	116.3		
2.261		114	
2.741			106.7
2.951	108.6		
3.761		109	
4.751			96.5
5.251	89.6		
6.801			87.6
7.261		91	
10.251	73.4		
12.261			65
14.261		61	
17.761			47.6
20.251	43		
23.761			34.6
28.261		41	
30.261			24.6
40.251	18.8		

Table 2-4: Summary of signal intensity in knee cartilage of 3 healthy volunteers over a variety of scans with variable TE.

Regression least squares fitting was attempted for this data. However, in none of the three cases was the standard biexponential model of sodium relaxation (which assumes a 60% contribution of the ‘fast’ component and a 40% contribution of the ‘slow’ component of T2) able to correctly fit the acquired data. Signal intensity followed a very rapid initial decline, after which a slower period of decay was experienced. The inability of the standard 60-40 biexponential

model to explain these results is demonstrated with the data for subject #3 in Figure 2-9 below.

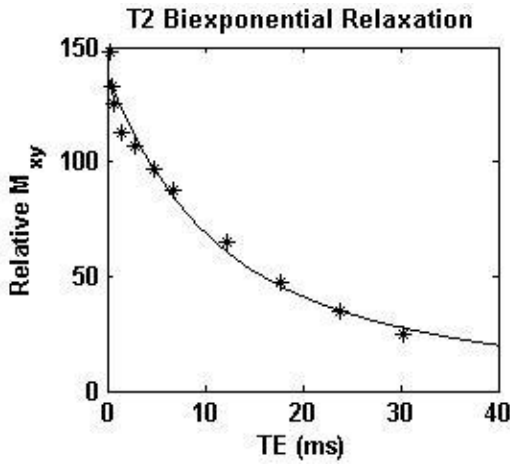


Figure 2-9: Least squares regression analysis of subject #3 T2 relaxation data using a standard 60-40 biexponential model. This fit gave T2 values ( $\pm$  95% regression confidence interval) of T2fast =  $9.0 \pm 4.7$  ms and T2slow =  $37.8 \pm 27$  ms for this data.

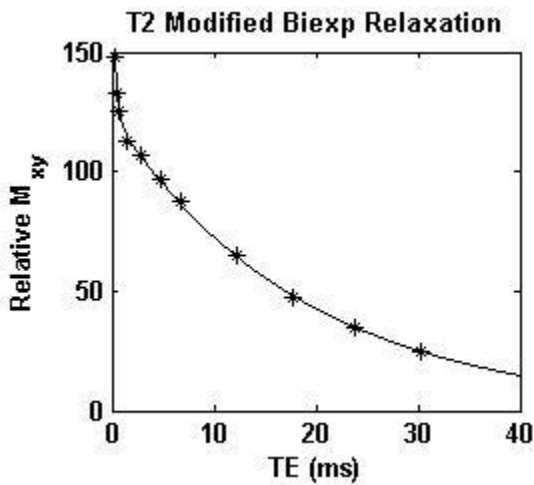


Figure 2-10: Least squares regression analysis of subject #3 T2 relaxation data using an expanded regression. A 32-68 biexponential model was found to fit the data best. It gave T2 values ( $\pm$  95% regression confidence interval) of T2fast =  $0.35 \pm 0.09$  ms and T2slow =  $18.9 \pm 0.7$  ms for this data set (subject #3).

When, however, the 60-40 (fast-slow) assumption was discarded, a new model found much better agreement with some of the observed data. New parameters were included in the regression analysis to determine the correct proportioning of signal intensities. A model resulting in a split of approximately 32-68 (fast-slow) resulted in a good fit to the experimental results of subject #3, as demonstrated by reanalysis of the same relaxation data in Figure 2-10. The unscaled images are shown in Figure 2-11 for a single slice; dephasing and loss of signal is readily evident as the TE increases.

Reanalysis of the relaxation data for the three subject resulted in the T2 relaxation data ( $\pm$  95% regression confidence interval) shown in Table 2-5. Relatively good agreement was found with the data for subject #1; however, the new model did not fit the data for subject #2 at all, and resulted in no usable T2 values. It was not determined why this fit did not work for the data set from subject 2; further study may be indicated.

Subject	T2 <sub>fast</sub>	T2 <sub>slow</sub>
1	0.33 $\pm$ 0.6	19.6 $\pm$ 3.5
2	-	-
3	0.35 $\pm$ 0.09	18.9 $\pm$ 0.7

Table 2-5: T2 values based on a 32-68 fast-slow relaxation model. This model resulted in good agreement for subjects 1 and 3, but in non-agreement for subject 2.

The problems of T2 characterization may be due to quadrupolar splitting, which has been previously found in collagen and cartilage tissue (57-58). Sodium, as a quadrupolar nucleus of spin = 3/2, possesses electric field gradients at the surface of the nucleus which can cause changes to the energy levels of the spin orientations (see Section 1.6.2). The change in the energy levels results in a ‘splitting’ of the spectrum of sodium frequency. The fast component of T2 is characterized by the -3/2 to -1/2 and the 1/2 to 3/2 transitions. Under quadrupolar splitting, the spectra associated with these transitions is separated from the central

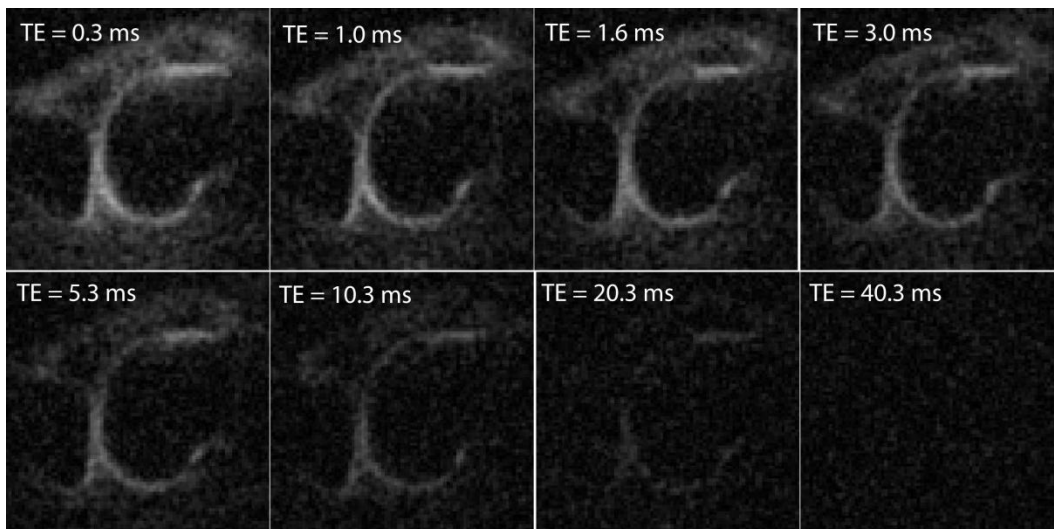


Figure 2-11: Images taken from the variable TE experiment. As TE increases, image quality deteriorates due to dephasing of spins due to T2 relaxation.

sodium Larmor frequency. If transmit bandwidth is not high enough, incomplete excitation of the fast transition may occur, resulting in less relative contribution of the fast component of T2 relaxation. This may explain the ability of the 32-68 model to partially describe our experimental results.

Due to the problems in determining a solid T2 value experimentally, it was decided to use T2 values from the literature (39-40) for the simulations and experiments of Chapter 3. These values were determined by multiple quantum methods for human cartilage *in vivo*, and had small standard deviations of measurement (~ 10%).

## **2.6 Conclusion**

While the preliminary undertakings described here were performed more in order to be in a position where research could be begun than to arrive at interesting results in and of themselves, the contents of this chapter are nevertheless somewhat illuminating. The derivation of the equation in order to recalculate rung capacitance removes many hours of trial and error work adjusting capacitor values to arrive at the correct resonant frequency. The measurement of the T1 of sodium in knee cartilage is the first one made *in vivo* known to the author. Finally, the most interesting result is that of the T2 relaxation measurements. The poor ability of the standard 60-40 biexponential curve to match the experimental data was demonstrated; in certain cases, a different distribution of 32-68 was found to better match the data. This interesting result may suggest the presence of residual quadrupolar splitting. As further discussed in Chapter 3, quadrupolar splitting has been observed in cartilage (41), and this effect may have caused the difficulty in the T2 measurements. Further study of T2 relaxation of sodium in cartilage *in vivo* and the possible effects of quadrupolar splitting are recommended.

## **Chapter 3**

### **Signal-to-Noise Optimization for Sodium MRI of the Human Knee at 4.7 Tesla Using Steady State**

*A version of this chapter has been submitted for publication*

*(A. Watts, R. S. Stobbe, C. Beaulieu, Magn Reson Med)*

#### **3.1 INTRODUCTION**

Osteoarthritis (OA) is associated with degenerative cartilage in joints that results in pain, swelling, and reduced motion and flexibility. Proper treatment of the affliction is dependent upon early diagnosis; however, the relatively small morphological changes that occur during early progression of the disease may be difficult to detect using standard clinical proton MRI (5-7). A molecular indication of the initial stages of OA is the reduction of proteoglycan molecules in the collagen matrix of the cartilage (59-60). Proteoglycans contain negatively charged glycosaminoglycan (GAG) side chains which create a negative fixed charge density (FCD) in the cartilage matrix (12). Positively charged sodium ions are attracted to the GAG chains, and as such sodium MRI has been proposed as a method to detect and quantify cartilage degradation (13-14). However, compared to water (i.e. proton), sodium suffers from low concentrations in vivo (~300 mM versus 50 M), and a four times lower gyromagnetic ratio, resulting in a much lower signal to noise ratio (SNR) that makes the acquisition of clinically useful images within an acceptable scan time difficult. Higher static magnetic field strengths and optimal pulse sequences are key to overcoming this limitation.

Sodium in knee cartilage (and other tissues) exhibits extremely rapid biexponential T<sub>2</sub> (37,61) relaxation and thus signal loss can occur if the echo time (TE) is not kept short (e.g. sub-ms). T<sub>1</sub> relaxation for sodium (37) is also very short which facilitates rapid scanning with shorter TR than typically used for proton MRI. Three dimensional gradient echo sequences have demonstrated the feasibility of sodium MRI of the human knee in vivo (13-14,29,43), however,

these approaches are suboptimal as they required a TE of 2-6.4 ms. Three dimensional projection imaging permits extremely short TE and has been implemented for sodium knee imaging either with twisted (TE=0.4 ms) (31,40) or with straight radial projections (TE=0.16 ms) (44). Non-selective hard radiofrequency (RF) pulses are also essential to achieve short TE in these 3D projection sequences. However, mere reduction of TE to the lowest possible limit is not enough to optimize SNR under biological conditions. For a given flip angle, short pulse length (hence low TE) requires high transmit power. Since specific absorption rate (SAR) is proportional to  $[B_0]^2$ , tissue heating constraints can become prohibitive at higher field strengths which are otherwise beneficial for sodium imaging. As such, an integrated optimization approach to maximize SNR is desirable.

The optimization of sodium SNR under SAR constraints has been investigated for the human brain (51). This method is known as projection acquisition in the steady state (PASS), and involves reducing the repetition time (TR) significantly which is only permissible if the excitation radiofrequency power is reduced by using smaller flip angles and/or longer pulses. Several previous sodium MRI studies of the human knee in vivo have used long TR values on the order of 80-100 ms both to minimize any signal saturation due to T1 and to satisfy SAR constraints (29,40,44). However, in a given scan time, the reduced TR of the PASS method allows the collection of extra projections which can be averaged to produce an SNR benefit over the standard higher power short TE/long TR scan, also known as a tissue sodium concentration (TSC) approach for its ability to quantify sodium content with minimal relaxation weighting. The significant SNR benefits are possible even though the pulse length (hence TE) must be increased (with associated greater T2 decay) in order to conform to SAR regulations. SNR increases of ~40% in the same scan time have been demonstrated for PASS over TSC of the human brain at 4.7T (51). The purpose of this work was to use three dimensional sampling density shaped twisted projection imaging (3D-TPI) (62) to evaluate the PASS method for enhancing SNR and yielding improved image quality for sodium MRI of the human knee in

vivo. Although the results presented are at 4.7T, the concept is valid at smaller and greater field strengths, although the potential gains could vary.

## 3.2 METHODS

### 3.2.1 Simulations

Sodium signal was simulated (51) for a range of combinations of pulse length (proportional to TE) and TR at constant SAR of approximately 6 W/kg and constant scan time. The simulations of cartilage will differ from human brain given the unique relaxation characteristics and the greater SAR permitted for extremities. TR was chosen to range from 20 ms to 100 ms. The smallest TR to accommodate the 3D-TPI pulse sequence experimentally was ~25 ms so the lower limit chosen was 20 ms. The upper TR limit was 100 ms, in order to allow full T1 recovery (based on a T1 of 19 ms) to minimize steady state effects on signal. RF pulse lengths ( $\tau_{RF}$ ) were chosen to range between 0.1 and 0.45 ms, (which with a constant system delay of 0.06 ms yields a TE range of 0.11-0.285 ms). Hardware limitations made 0.1 ms the smallest pulse length that can be used for RF excitation on our system, and rough preliminary simulation results indicated that pulse lengths greater than 0.45 ms would require a TR of less than 20 ms to provide equivalent SAR. In order to better display our simulation results for the parameters ultimately chosen, Figure 1 only shows pulse length ranging from 0.1 to 0.4 ms. For every combination pair of pulse length and TR, the simulation program calculated the flip angle needed to yield a constant SAR based on the physical relationship:

$$SAR \propto \frac{B_0^2 \cdot \theta^2}{TR \cdot \tau_{RF}} \quad [3-1]$$

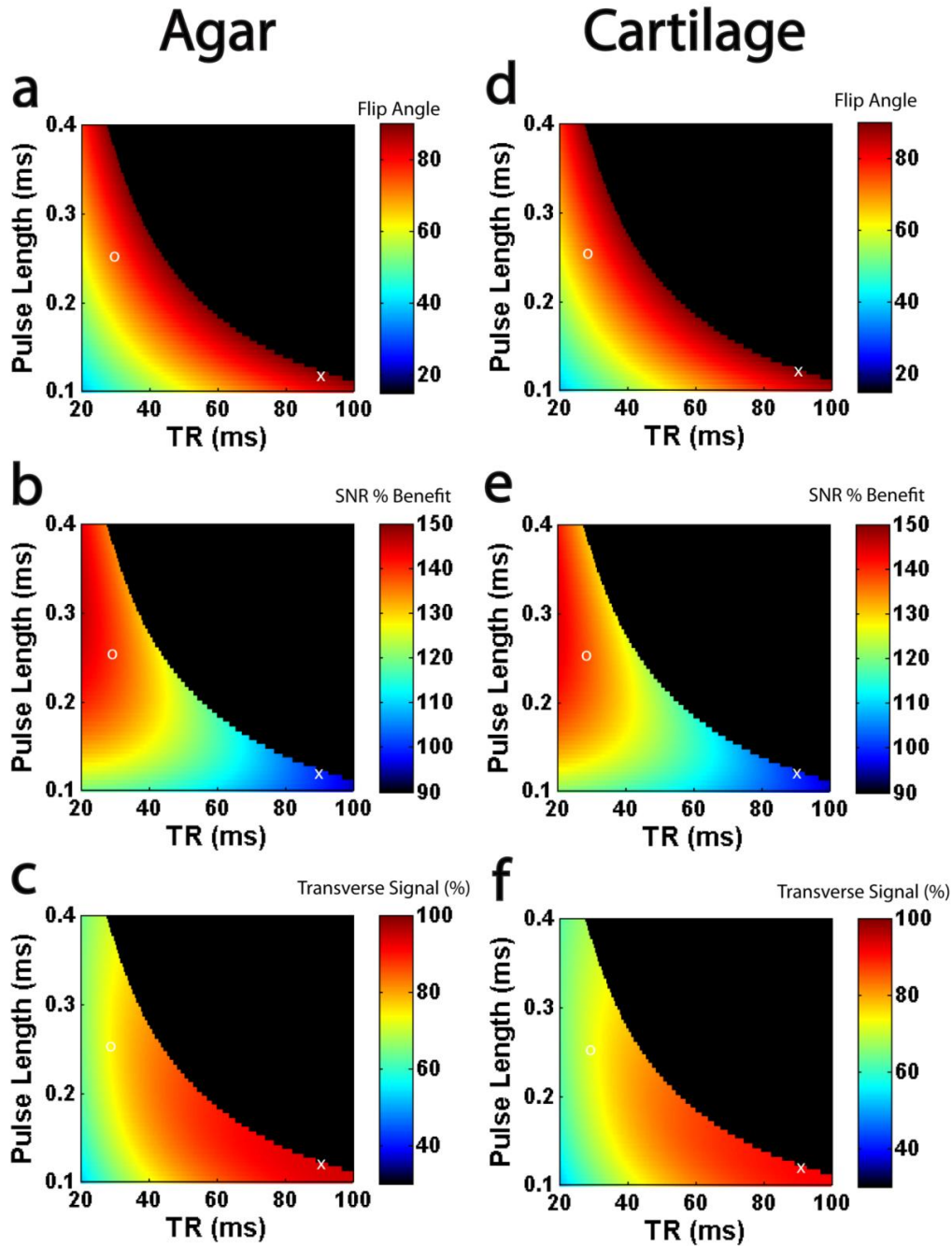


Figure 3-1: Simulations of sodium signal at 4.7T in agar phantom (a-c) and human cartilage (d-f). (a) and (d): Flip angles for a constant SAR of 6 W/kg over a range of combinations of pulse length and TR. TSC parameters (pulse length=0.120 ms, TR=90 ms, flip angle=90) are marked with an X while PASS parameters (pulse length=0.250 ms, TR=30 ms, flip angle=74) are marked with an O. (b) and (e): Predicted SNR benefit of PASS over TSC when averaging is used to equate scan time. Note that in both cases, the SNR benefit is scaled so that the TSC parameters have a relative value of 100%. (c) and (f) Transverse magnetization is expressed as a percentage of theoretical full signal (TR sufficiently long to produce zero steady state, TE infinitesimally small). Despite reduced transverse magnetization of PASS compared to TSC, PASS parameters show a significant SNR benefit due to averaging.

The value of 6 W/kg, while conservative according to RF maximum deposition guidelines (which allow 12 W/kg for extremities) was chosen because sodium protocols often involve longer duration scans, in addition to the fact that knee size and thus coil loading is highly variable.

The quantum mechanical quadrupolar spin signal simulations required the relaxation parameters of the sodium nuclei. The T1 and T2 relaxation parameters for a 10% (500 mM) agar phantom were determined by measuring normalized signal intensity during inversion recovery and variable TE experiments, respectively. Relaxation parameters of sodium in agar (n=5) were determined to be  $T1 = 19.2 \pm 0.2$  ms (mono-exponential fit),  $T2^*_{\text{slow}} = 14.4 \pm 0.9$  ms,  $T2^*_{\text{fast}} = 2.2 \pm 0.1$  ms at 4.7T. From this relaxation data, a spectral density model of  $J_0(0) = 408$  Hz,  $J_1(\omega_0) = 46$  Hz, and  $J_2(2\omega_0) = 23$  Hz was chosen for simulation. The high agar concentration of 10% was chosen due to its similarity to human cartilage for sodium relaxation characteristics (30).

Using the 3D-TPI acquisition, inversion recovery experiments measured T1 using least squares regression analysis of image intensity in cartilage in several locations in the knee. Inversion times of  $TI = 3, 7, 15, 25, 40,$  and  $70$  ms were acquired, and TR was adjusted to ensure a constant delay of 100 ms between the excitation pulse and the following inversion pulse. The projection set had a nominal resolution of  $1.5 \times 1.5 \times 6$  mm<sup>3</sup>, TE = 0.261 ms, and total acquisition time for all six inversion recovery scans was 38 min. A monoexponential fit of the T1 relaxation experiment resulted in a T1 ( $\pm$  95% regression confidence interval) of  $19.3 \pm 3.7$  ms for sodium in the knee cartilage of a healthy volunteer, aged 30. A T1 value of  $18.4 \pm 2.8$  ms was found in the same experiment on a second healthy volunteer, aged 31. Based on these results, a T1 relaxation value of 19 ms was chosen for simulation. To the best of our knowledge, the T1 of sodium in human cartilage has not been measured in vivo before. However, this value compares reasonably well to those of excised bovine cartilage encountered in the literature at field strengths of 2-7T, where the T1 ranges from 16-23 ms (14,30,35-37). Difficulty was encountered in the determination of T2 parameters in femoral-tibial cartilage using a variable TE experiment. Biexponential fitting

could not account for the very rapid initial signal decay ( $TE < 1$  ms). As such, the parameters of  $T2_{\text{slow}} = 10$  ms and  $T2_{\text{fast}} = 1$  ms that were measured using multiple quantum techniques were taken from literature (39-40). This resulted in a spectral density model of  $J_0(0) = 922$  Hz,  $J_1(\omega_0) = 78$  Hz, and  $J_2(2\omega_0) = 22$  Hz for human cartilage in vivo.

The simulations used the spectral density parameters to determine transverse magnetization (taking into account relaxation) for each combination of pulse length, TR, and flip angle. Subsequent analysis of the data set allowed extrapolation of the relative SNR benefit to be determined if averaging was used to ensure equivalent scan time despite differences in TR.

### 3.2.2 Pulse Sequence Design

Based on the results of the simulations (Figure 3-1), and using nominal anisotropic voxel dimensions of  $0.8 \times 0.8 \times 4.0$  mm<sup>3</sup>, 3D-TPI acquisition parameters were chosen for both TSC (flip angle=90°, pulse length=0.12 ms, TE=0.12 ms, TR = 90 ms, 1 average) and PASS (flip angle = 74°, pulse length = 0.25 ms, TE=0.185 ms, TR=30 ms, 3 averages). Note that TE is calculated as half of pulse length plus the system acquisition delay (equal to 0.06 ms for both protocols).

The TSC parameter set required an extremely short pulse length to minimize signal loss at the centre of k-space, resulting in a choice of 120  $\mu$ s. Also for the TSC set, a flip angle of 90 degrees was desired, as this maximizes transverse signal. Together, these factors resulted in a TR choice of 90 ms for the TSC protocol to satisfy SAR. To simplify averaging, a TR of 30 was chosen for the PASS parameter set. At this value, a choice of 250  $\mu$ s for pulse length resulted in a high predicted SNR gain while maintaining pulse length reasonably low. The flip angle value of 74° was read from the intersection of the above TR and pulse length values in the flip angle simulations (Figure 3-1d).

Both protocols had nominal voxel volume (defined by  $1/(2 * K_{\text{max}})$ ) of 2.56 mm<sup>3</sup>, and constant acquisition times of 9 minutes for each TSC or PASS data set. The number of projections was 6000, each with a twist ( $p$ ) of 0.196 and readout

length of 18.6 ms, designed for a Hamming-like sampling density shape (62). The pulse sequence involves the application of a hard non-selective RF pulse to excite the volume of interest. In order to reduce the likelihood of ringing, which can adversely affect image quality and confound analysis, acquisition was performed using sampling density weighted apodization (SDWA). This technique has been shown to produce SNR benefits over other forms of apodization (62). After the system acquisition delay (60  $\mu$ s), the readout gradients are applied for the readout length as k-space is sampled along the projection trajectory (3D center

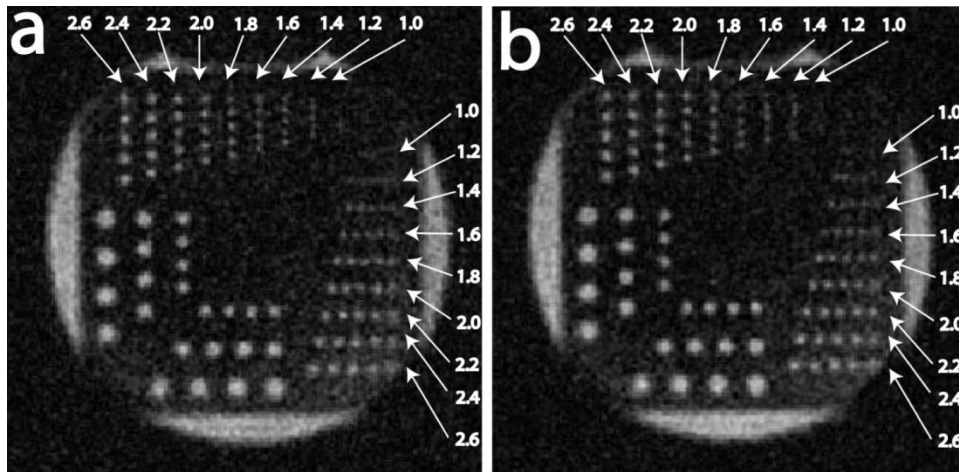


Figure 3-2: Resolution phantom images for (a) TSC and (b) PASS parameter sets. Hole spacing (in mm) are equivalent to their diameters, and are marked using the arrows. Equivalence in terms of field of view and spatial resolution is evident.

out twisted projection). Following readout, the spins are spoiled by the application of spoiling gradients; refocusing pulses equivalent to the negative of the integral of the readout gradient curve are applied simultaneously.

### 3.2.3 Phantoms

Two phantoms were constructed for use in validation of methodology. A saline resolution phantom was constructed by drilling sequential sets of holes in a rectangular piece of acrylic (90 by 90 mm, 12 mm thickness). Hole diameters were equivalent to their spacing for each set, ranging from 5.0 mm to 1.0 mm. The acrylic was placed inside a plastic bottle so that the acrylic face was perpendicular to the long axis of the bottle. The bottle was then filled with saline

at 250 mM and bubbles were removed from the hole sets. This resolution phantom was used during sequence testing to ensure correct reconstruction of images as well as to verify effective spatial resolution for each protocol (Figure 2). An agar phantom was also constructed by dissolving 10% agar by weight in boiling water and adding NaCl so that overall sodium concentration was 500 mM. The agar phantom was used to verify experimentally the predicted SNR advantage of PASS over TSC from the simulations.

### 3.2.4 Experiments

All sodium MRI experiments were performed on a Varian Inova 4.7T whole body scanner with a single tuned 53 MHz 12 rung custom birdcage knee coil (diameter 17.8 cm, leg length 10 cm). RF transmitter peak output was 2.5 kW. Maximum readout gradients applied were 9.9 mT/m, and spoiling gradients were 30 mT/m. Sodium images using both TSC and PASS parameter sets, keeping spatial resolution the same, were acquired for the saline resolution phantom and 10% agar phantoms, and the right knee of ten healthy volunteers (age 26+/-4 years). All volunteers signed informed consent forms as required by the Health and Research Ethics Board at the University of Alberta.

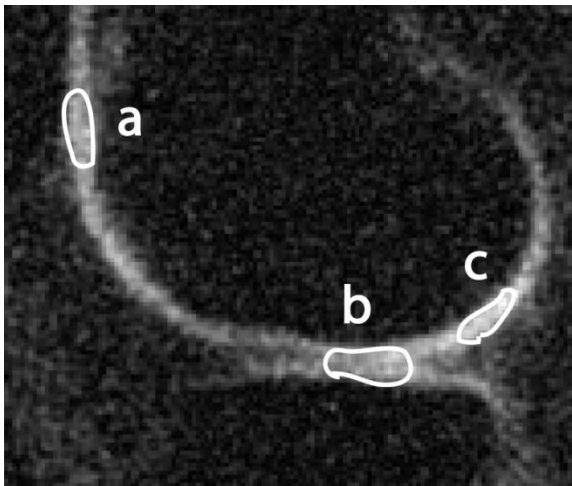


Figure 3-3: ROI locations in sagittal viewing plane of sodium image, depicting (a) patellar cartilage (b) femoral-tibial cartilage, and (c) purely femoral cartilage

### 3.2.5 Data Analysis

Projection set design (including generation of gradient and refocusing files), image reconstruction, and region-of-interest (ROI) analysis was performed

using custom software utilities (in Matlab). ROI were drawn over several slices of the reconstructed 3D volume to cover as much tissue as possible. Signal ROI (Figure 3) were drawn in three distinct locations in each sagittal knee image: in the patellar cartilage, femoral/tibial cartilage junction, and purely femoral cartilage. All signal ROI were drawn following the visible cartilage contours in the sodium images; dual windows in the analysis program allowed exactly matching ROI to be drawn for SNR comparison between the PASS and TSC images. SNR values were calculated by taking the mean value of pixels in signal ROI and divided by the standard deviation of pixel value in the noise ROI, located in the image background. As background noise in absolute value images follows a Rayleigh distribution instead of Gaussian, the SNR value was then multiplied by a correction factor of 0.665.

### **3.3 RESULTS**

#### **3.3.1 Phantom Validation**

During initial sequence testing, the resolution phantom was used to ensure proper reconstruction of the images (Figure 3-2). In addition, effective in-plane resolution was equivalent for both protocols at 1.4 mm, which is worse than the nominal voxel size of 0.8 mm in-plane. A comparison was made between the SNR gain predicted by the simulations for the agar and that observed in the sodium images of the agar phantom. The simulations predicted a 38% increase for the PASS parameters over the TSC parameters in 10% agar, which agrees well with the experimental result of 39+/-2% (n=3).

#### **3.3.2 Human Volunteers**

The human cartilage scans (Figure 3-4) display several benefits of PASS over TSC. Cartilage tissue is well delineated in both scans, but slightly smoother in the PASS images. In addition, noticeably more noise is present in the TSC than in the PASS acquisition, shown in both the central bone as well as outside the tissue area. The simulation results (Figure 1e) indicate that there should be a 37% increase in SNR when using PASS instead of TSC for the same scan time

and SAR. The SNR benefit in the 10 volunteers was  $29 \pm 4\%$  (Figure 4c) for PASS over TSC, which is lower than that predicted by simulation.

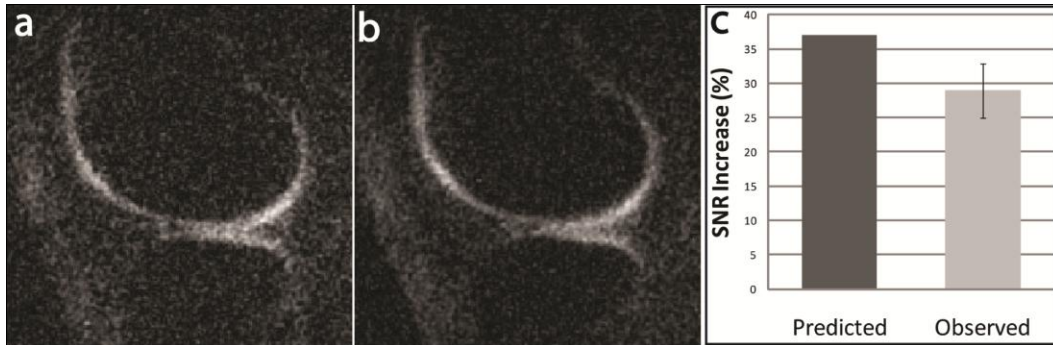


Figure 3-4: Sodium MRI of the knee, sagittal orientation, using (a) TSC parameters (flip angle=  $90^\circ$ , TE/TR = 0.120/90 ms, 1 average) (b) PASS parameters (flip angle=  $74^\circ$ , TE/TR = 0.185/30 ms, 3 averages). Both images were sampled with the identical 3D twisted projection acquisition scheme, and scan times are equivalent at 9 minutes each. (c) The observed SNR increase is significant, but unlike the agarose gel experiment does not match the value predicted by simulations.

In order to determine if there were any regional variations, the SNR of both parameter sets was evaluated in three different cartilage areas in the sagittal orientation: below the patella, at the femoral-tibial junction, and on the femur only. A significant and equivalent increase in SNR was found in all three areas (see Figure 3-5). The SNR gains correspond to consistent average percentage increases of 29% in each area.

A combined SNR increase over all three ROIs (normalized by ROI area) was calculated per subject for each protocol. Individualized analysis (per volunteer) of combined SNR values showed some variability in the results, however, there was a significant SNR benefit of 22-36% (mean of  $29 \pm 4\%$ ) in all ten volunteers (Figure 3-6). A two-tailed paired t-test was conducted; the increased SNR of PASS over TSC was statistically significant ( $p < 0.001$ ). The excellent quality of PASS images is displayed in Figure 3-7. The axial orientation (Figure 3-7a) shows clear delineation of the patellar cartilage; the popliteal artery is also shown in the bottom center of each image. In the coronal orientation (Figure 3-7b) a clear separation of the tibial and femoral cartilage in the posterior condyles is displayed. The sagittal images also demonstrate excellent image

quality; both femoral and tibial cartilage is clearly delineated, and contours of the surrounding tissue and patella are also visible.

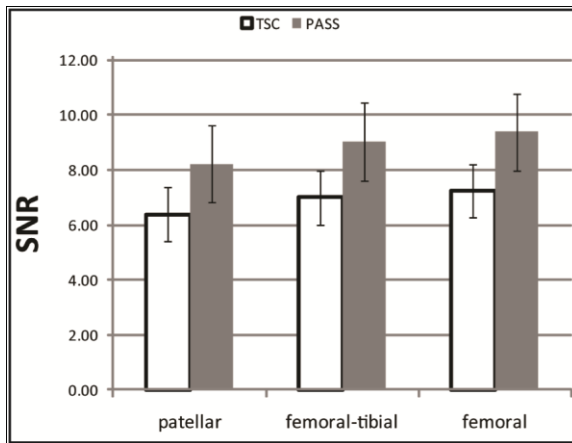


Figure 3-5: SNR values ( $\pm$ SD) in the cartilage for both TSC and PASS parameters. The PASS protocol has an SNR improvement of 29% in all three areas. A two-tailed paired t-test found that the increase in SNR of PASS over TSC was also statistically significant when divided by region ( $p = 0.002$ ). Note that the  $\pm$  bars are indicative of intersubject variability and not measurement error.

### 3.4 DISCUSSION

The use of smaller flip angles and longer RF pulse lengths (and longer TE) to offset SAR increases associated with a shorter ‘steady-state’ TR in order to allow increased averaging produced a sizeable SNR increase in sodium scans for both agar gel phantoms and human cartilage in vivo. There was excellent experimental agreement with the simulation prediction for the agar phantom. While a substantial SNR benefit was found for human cartilage in vivo, it was ~8% below that predicted by the simulations. There are several possible reasons for this.

Gaussian distributed spectral splitting, often considered relevant for biological tissue (41,63), with mean of 0 Hz and standard deviation of 450 Hz would explain the reduced SNR benefit. This value is somewhat higher than a recent measurement on excised bovine nasal cartilage that yielded a standard deviation of

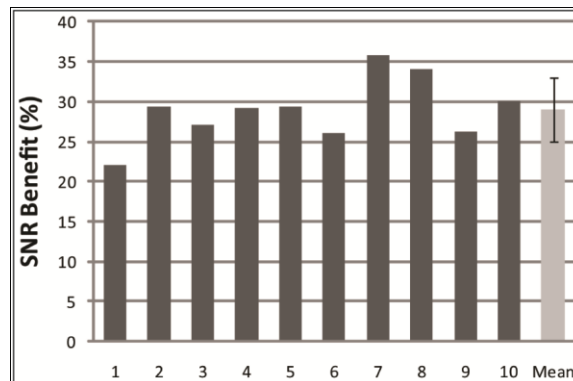


Figure 3-6: Percentage SNR benefit over all three cartilage regions of 22-36% for PASS over TSC in 10 healthy volunteers. Mean ( $\pm$ SD) value is  $29 \pm 4\%$ .

117 Hz (41). Gaussian distributed spectral splitting also explains the initial rapid decay in the cartilage T2 measurement experiment and the inability to fit a biexponential curve. Another factor which could be responsible for the discrepancy between simulation and experiment is underestimation of T1. A T1 value of ~24 ms would produce predicted SNR benefits which are in agreement with the observed results. It is likely that a combination of these effects may be responsible for the disagreement between the predicted and observed SNR benefits. Finally, the influence of partial volume effects of cartilage with surrounding tissue (including bone and synovial fluid) in conjunction with the difficulty of measuring signal intensity in a tissue that is as physically small as knee cartilage may be responsible for the inter-subject variation in the SNR benefit.

Sodium magnetic resonance image quality is affected by the ultrafast T2 relaxation, which causes blurring. As a result, *effective* spatial resolution (quantified by the ability to distinguish between objects) is worse than *nominal* spatial resolution (defined by  $1/(2 \cdot K_{\max})$ ). Our images, while nominally  $0.8 \times 0.8$  mm<sup>2</sup> in-plane, can only distinguish between holes in the resolution phantom which are 1.4 mm apart or greater. However, despite image blurring, twisted projection imaging with PASS may provide the best compromise between acceptable SNR, low TE and adequate coverage of k-space. Our results show high quality images for a nominal voxel size of 2.56 mm<sup>3</sup>, which compares favourably relative to 3D gradient echo sequences whose nominal voxel sizes range from 5.4 to 14 mm<sup>3</sup> and whose TE range from 2 to 2.4 ms (13-14,29) as well as to other results using projection reconstruction, whose nominal voxel size was 3.4 mm<sup>3</sup> and TE was 0.16 ms (44).

The PASS technique involves increasing T1 weighting significantly (from 1% to 21% based on T1 = 19 ms) and T2 weighting slightly (from 7% to 11% based on T2<sub>fast</sub> = 1 ms and T2<sub>slow</sub> = 10 ms). The increase in T1 weighting in PASS deviates from an absolute tissue sodium concentration approach, which could result in reduced quantification ability. However, some sensitivity to T1 may have an advantage. If degraded cartilage shows an increase in T1 compared

to healthy cartilage, as has been shown in bovine cartilage (37-38), then a reduction in TR would result in increased steady-state effects. This would in turn result in reduced local signal and an increased ability to determine regions of degradation. This form of contrast may prove useful; several studies have investigated different contrast mechanisms for sodium MRI of cartilage such as inversion recovery (35) or triple quantum filtered imaging (40). The relatively small increase in TE (from 0.120 ms to 0.185 ms) which results in the small T2 weighting increase mentioned above should have only a minor effect on sodium quantification capability.

The benefits of PASS are available at field strengths both stronger and weaker than 4.7T. SAR is much less restrictive at 3 Tesla, and for TSC imaging with flip angle =  $90^\circ$  and TR = 90 ms, RF pulse lengths as short as 0.05 ms could theoretically be implemented for the same SAR of  $\sim 6$  W/kg as that of this study. Simulation suggests a PASS sequence with flip angle =  $77^\circ$ , pulse length = 0.11 ms, and TR = 30 ms (the same TR as that of this study) would yield 40% more SNR than the theoretical TSC case (Figure 3-8b). At higher fields such as 7 Tesla, SAR is much more constraining, and for a TSC sequence with flip angle =  $90^\circ$  and TR = 90 ms, RF pulse lengths must be increased to 0.27 ms for the same SAR. At 7 Tesla simulation suggests a PASS sequence with flip angle =  $63^\circ$ , RF pulse length = 0.40 ms, and TR = 30 ms would yield 31% more SNR than the TSC case (Figure 3-8e). The SNR benefits stated above assume the same relaxation parameters for cartilage as used above for simulation at 4.7T and the absence of quadrupolar splitting. Note that while a 30 ms TR was used for experiment in this study, facilitating comparison at 3x the averaging of the TSC approach for the same scan duration, the PASS sequence could be implemented with even shorter TR values for increased SNR benefit at each field strength. Note also that while the relative benefit of steady-state sodium imaging of the knee with respect to TSC imaging is diminished with increasing field strength, this does not imply reduced value for imaging at 7T in general, which will benefit from  $B_0$  related magnetization increase.

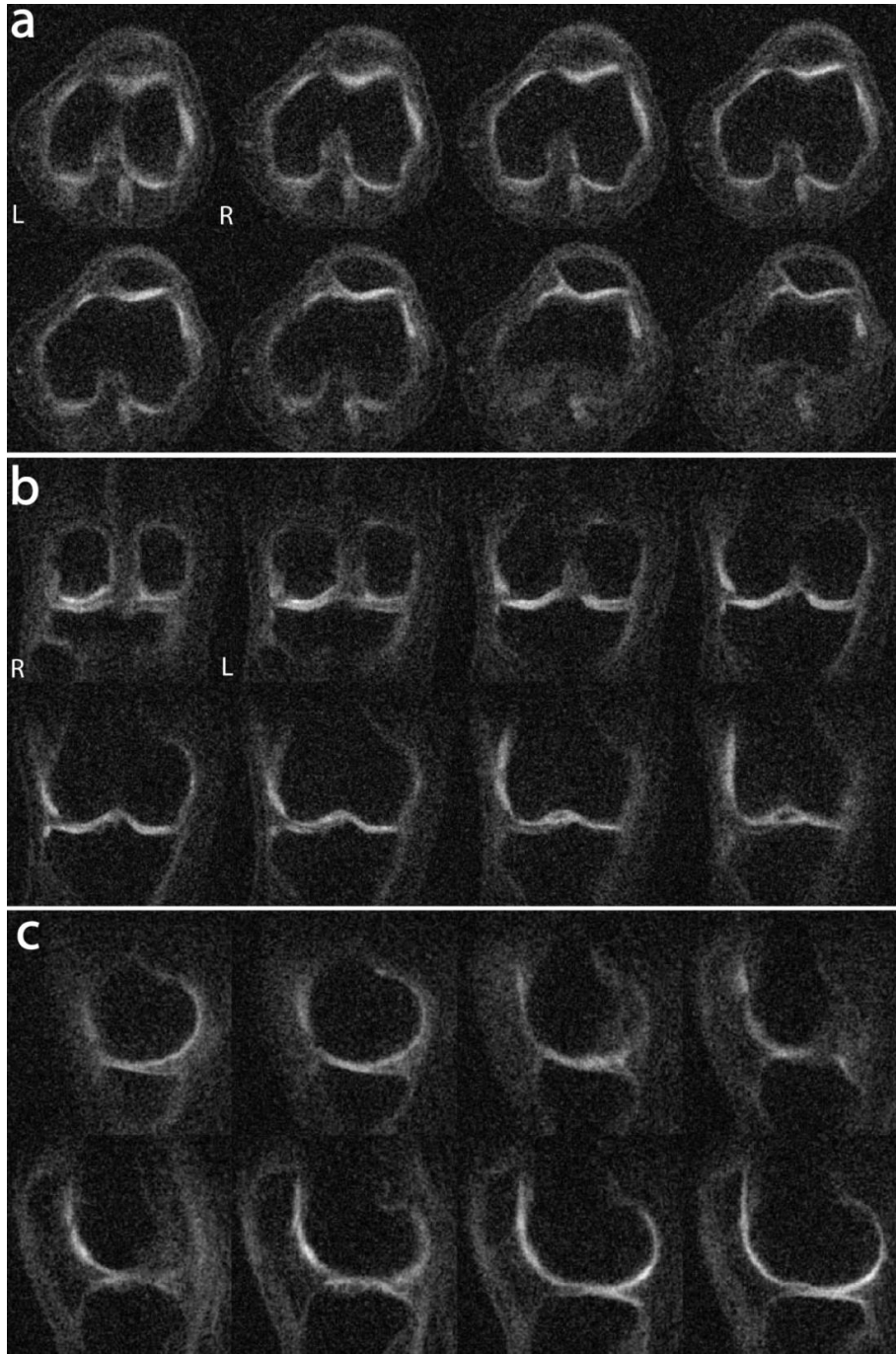


Figure 3-7: Sodium images of the knee of a healthy volunteer at 4.7 T using the Na-PASS pulse sequence (6000 projections,  $p=0.196$ , readout length 18.6 ms. (a) Axial, (b) coronal, and (c) sagittal planes were acquired separately in 9 minutes. Apparent distance between slices (calculated by taking the field of view, dividing by inverse filter size, and multiplying by the number of reconstructed slices between the displayed slices) is 8 mm for (a) and (c), and 5 mm for (b). The nominal voxel size is  $0.8 \times 0.8 \times 4.0 \text{ mm}^3$ . SNR in the cartilage is  $\sim 12$ . Left and right sides are marked by L and R letters for the axial and coronal orientations.

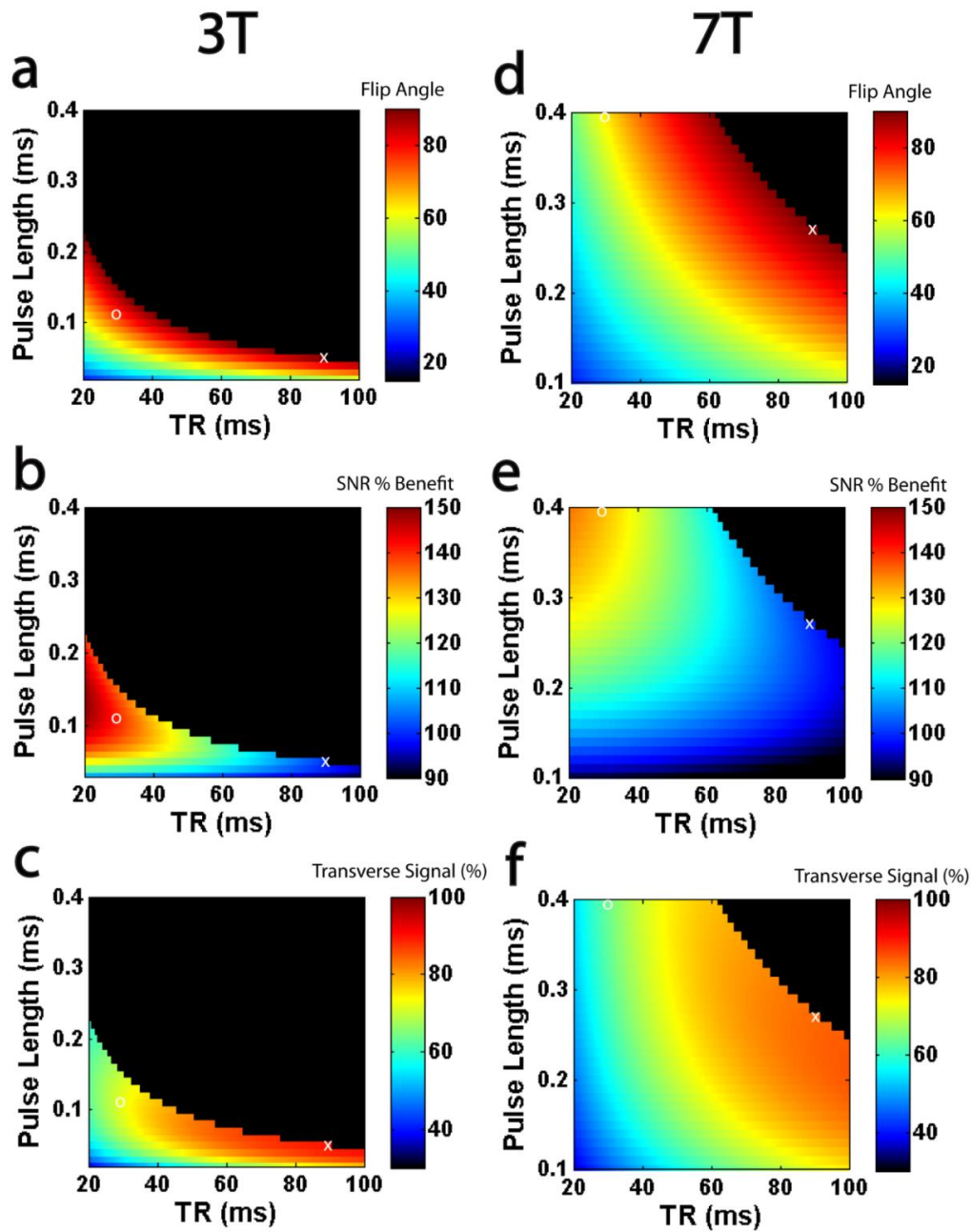


Figure 3-8: Simulations of sodium signal in human cartilage at 3T and 7T: (a) and (d) Flip angles for a constant SAR of  $\sim 6$  W/kg over a range of combinations of pulse length and TR. TSC-like parameters for each field strength are marked with an X while PASS-like parameters are marked with an O. (b) and (e) Predicted SNR benefit of PASS over TSC at 3T (40%) and 7T (31%). Note that in both cases, the SNR benefit is scaled so that the TSC parameters have a relative value of 100%. (c) and (f) Transverse magnetization is expressed as a percentage of theoretical full signal (TR sufficiently long to produce zero steady state, TE infinitesimally small).

### **3.5 CONCLUSIONS**

Excellent quality images of the cartilage in the human knee within a reasonable scan time of 9 minutes at 4.7T were demonstrated using the Na-PASS technique in which longer RF pulses and smaller flip angles, together with shorter TR are used to allow increased averaging within specific absorption rate constraints. While there was a significant SNR benefit with the use of PASS instead of TSC at 4.7T, the experimental measurements in human cartilage in vivo fell short of the predictions made by simulations. This may have been due to interference from quadrupolar splitting, inaccurate T1 relaxation parameters, or partial volume effects from the inclusion of synovial fluid in the cartilage ROI. The SNR benefit that was demonstrated can enable improved resolution and/or reduced scan time. Future work will concentrate on the evaluation of the PASS versus TSC approaches with respect to detecting reduced sodium content in the knee cartilage of patients with confirmed osteoarthritis.

## **Chapter 4**

### **Improved In-Plane Resolution of 3D TPI Sodium MRI of the Human Knee Using Anisotropic Voxels**

*This work was presented at the Annual Conference for the International Society of  
Magnetic Resonance in Medicine (ISMRM), Stockholm 2010*

*(A. Watts, R. Stobbe, and C. Beaulieu, Anisotropic Twisted Projection Sodium  
MRI of Articular Cartilage in the Human Knee, program number 4966)*

#### **4.1 INTRODUCTION**

Sodium is an important metabolite whose physiological interaction in living systems can be highly important to their proper functioning. Knowledge of sodium concentration and location can be extremely useful in the study of many disorders and diseases. With the ability to non-invasively determine sodium information in vivo, sodium magnetic resonance imaging (MRI) has been proposed as a tool for medical and research studies for decades (43,64). In the knee, sodium content has been found to correlate with cartilage glycosaminoglycan (GAG) content (14,29), the lack of which may be an early sign of cartilage degeneration and osteoarthritis. However, complications relating to imaging sodium nuclei have prevented its widespread use.

The combination of high proton availability (e.g. as in water at concentrations of ~50 M throughout the body) and high MR sensitivity give proton MRI an adequate signal to noise ratio (SNR), which can be exploited to yield high resolution images. On the other hand, sodium concentrations in vivo are relatively low and the gyromagnetic ratio of sodium is one fourth that of proton. Combined with sensitivity differences, the result is a sodium MR signal that is ~22,000 weaker than proton (17). In addition, sodium experiences extremely rapid biexponential relaxation in the T<sub>2</sub> domain (39-40), resulting in rapid signal loss at the center of k-space. In order for sodium images to be of use

both in clinical settings and in research studies, the naturally lower MR signal must be compensated for as much as possible.

Several studies have already investigated sodium MRI of the knee. Early acquisition strategies have used 3D gradient echo sequences (13-14,29,43), these strategies were undesirable due to longish TE (2-6.4 ms). More recently, straight radial projection imaging has been used (44), which has reduced TE (0.16 ms) and improved SNR. Despite complications of acquisition and reconstruction, three dimensional twisted projection imaging (3D-TPI) (48) and similar acquisition trajectories (65-66) have been shown to have SNR, resolution and/or imaging time benefits over sampling-inefficient radial imaging, and represent the current 'state of the art' in sodium MRI. However, the intrinsic spherical k-space trajectories of 3D-TPI results in an acquisition mode which ignores one of the simplest and oldest ways to increase SNR while maintaining high in-plane resolution: anisotropic voxels.

MR signal is directly proportional to the number of spins included in the voxel, which increases with voxel size. Since the advent of slice selection, proton MRI has frequently used a thicker out-of-plane dimension to maximize signal while reducing in-plane dimensions as much as possible. While this technique was used largely to provide full coverage of the tissue of interest using a limited number of slices (and the associated reduction in scan time), it yields increased signal yet results in excellent in-plane resolution, which allows clinicians to view smaller structures of internal anatomy (assuming that the structure is the same throughout the slice plane). The same benefits and restrictions should apply to sodium MRI, even when using a three dimensional acquisition. By giving up out-of-plane resolution, anisotropic voxels can maintain SNR while improving in-plane resolution. This may result in images of increased utility for the knee, whose cartilage thickness is only a couple of millimeters thick (67). Higher in-plane resolution could allow regions of local GAG loss to be more easily observed, allowing earlier diagnosis of the onset of osteoarthritis. The purpose of this work is to evaluate the use of anisotropic voxels versus standard isotropic

voxel selection in three dimensional twisted projection imaging of the human knee.

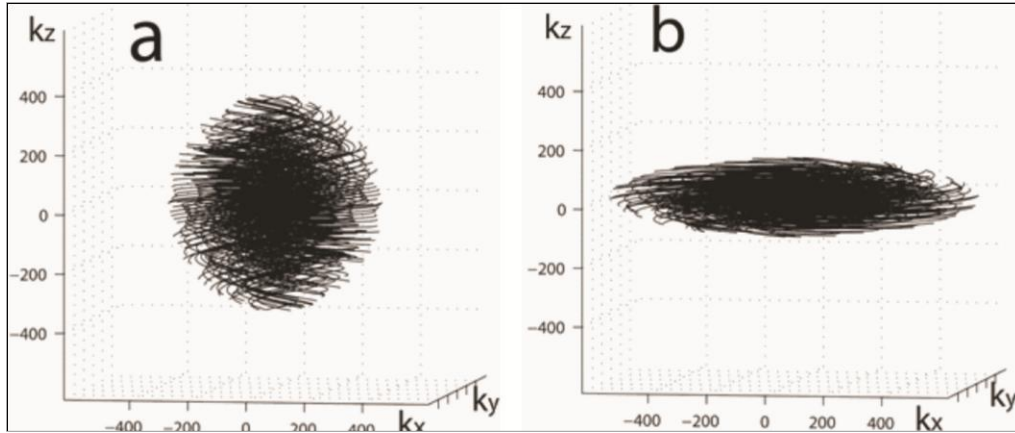


Figure 4-1: K-space projections for twisted projection imaging sodium MRI, including an (a) isotropic set (sphere), and (b) anisotropic set (oblate spheroid).

## 4.2 METHODS

### 4.2.1 Projection Set Design

Two sampling density shaped (62) 3D-TPI projection sets were designed, including one isotropic (nominal voxel size  $1.37 \times 1.37 \times 1.37 \text{ mm}^3$ ) and one anisotropic (nominal voxel size  $0.8 \times 0.8 \text{ mm}^2$  in-plane, and  $4.0 \text{ mm}$  out-of-plane). Both projection sets had the same sampled k-space volume and nominal voxel volume (defined by  $1/(2 * K_{\text{max}})$ ) of  $2.56 \text{ mm}^3$ , as well as equivalent twist ( $p = 0.198$ ) and readout length ( $17.6 \text{ ms}$ ). Both sets used the same scan parameters (pulse length= $0.3 \text{ ms}$ , TE= $0.21 \text{ ms}$ , TR= $25 \text{ ms}$ , flip angle= $74^\circ$ ). Voxel volumes ( $2.56 \text{ mm}^3$  for both projection sets) were chosen based on empirical determination of an acceptable SNR of sodium MRI of the knee of  $\sim 12$  at  $4.7\text{T}$ . The anisotropic 3D TPI voxels were attained by multiplying the out-of-plane gradient of each projection by a scaling factor of  $0.2$ , thus sampling k-space to an oblate spheroid (Figure 4-1b). The isotropic set used  $6750$  projections (4 averages), while the anisotropic set used  $9000$  projections (3 averages), to yield scans with the same number of total projection acquisitions ( $27000$ ) and the same total imaging time ( $11 \text{ minutes}$ ). In order to reduce the likelihood of ringing, which can adversely

affect image quality and confound analysis, acquisition was performed using sampling density weighted apodization (SDWA). This technique has been shown to produce SNR benefits over other forms of apodization (62).

The progression of k-space sampling is further demonstrated in Figure 4-2; projections at 0%, 60%, 85%, and 98% of sampling of the top half of k-space are shown for each set. While the anisotropic set samples much farther than the isotropic set in the  $K_x$  and  $K_y$  axes (resulting in better resolution along those dimensions), it samples nearly three times less far than the isotropic set in the  $K_z$  axis (resulting in poor out-of-plane resolution).

#### **4.2.2 Phantoms**

Two phantoms were used during this experiment. A uniform spherical saline phantom (diameter ~ 5 cm) was filled with saline at 500 mM concentration. In addition, a saline resolution phantom was constructed by drilling sequential sets of holes in a rectangular piece of acrylic (90 by 90 mm, 12 mm thickness). Hole diameters were equivalent to their spacing for each set, ranging from 5.0 mm to 1.0 mm (Figure 2-5). The acrylic was placed inside a plastic bottle so that the acrylic face was perpendicular to the long axis of the bottle. The bottle was then filled with saline at 250 mM and bubbles remaining in the holes were removed. This phantom was used to determine the effective in-plane resolution of each protocol.

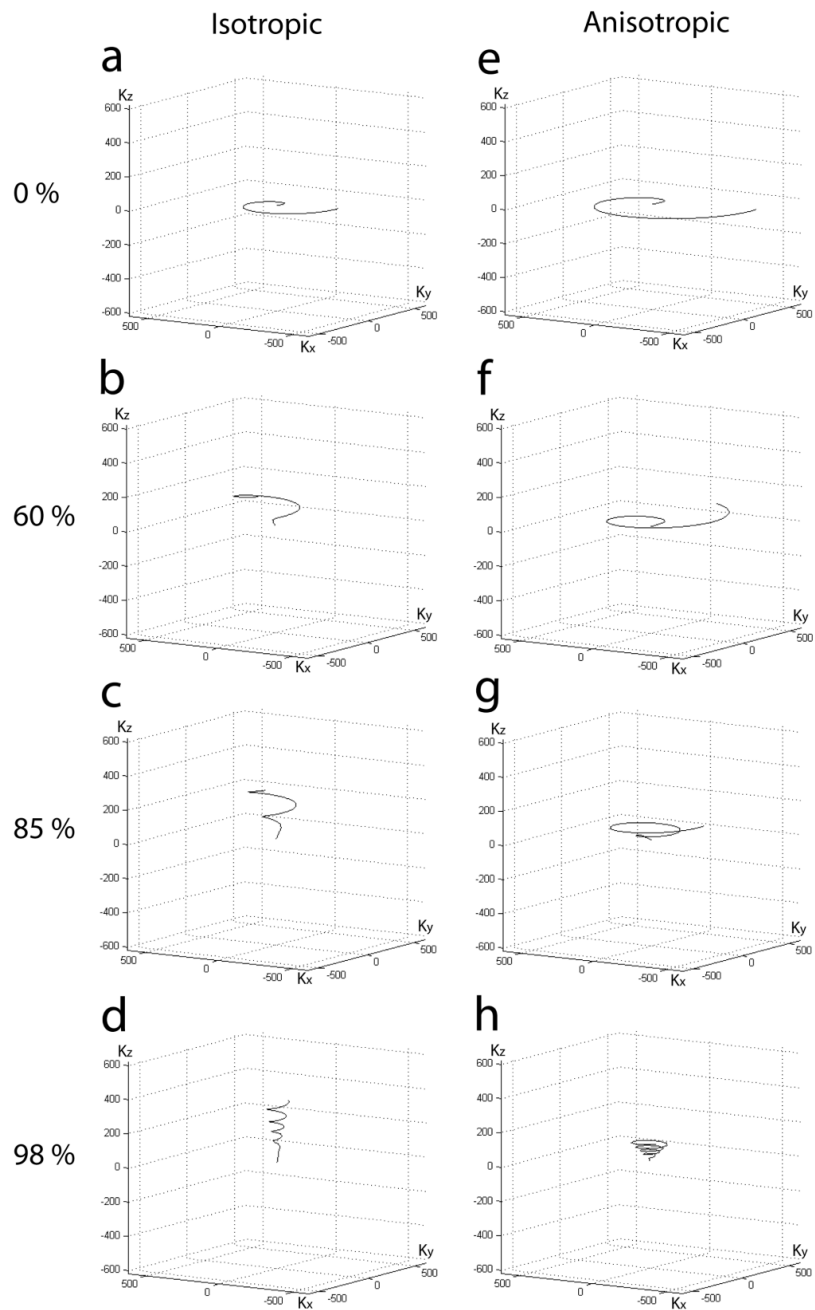


Figure 4-2: Acquisition projections at various completion percentages of sampling of the top half of k-space. (a,e) The first projection for each set demonstrates that the anisotropic set samples much farther in  $K_x$  and  $K_y$  than the isotropic set. Projections at (b,f) 60% and (c,g) 85% demonstrate the differing rates of  $K_z$  sampling. (d,h) A projection at 98% completion shows that the isotropic set samples the  $K_z$  plane almost three times farther than the anisotropic set.

### 4.2.3 Experiment

All sodium MRI experiments were performed on a Varian Inova 4.7T whole body scanner with a single tuned 53 MHz 12 rung custom birdcage knee coil (diameter 17.8 cm, leg length 10 cm). RF transmitter peak output power was  $\sim 0.5$  kW, the maximum gradients applied (during spoiling) were  $\sim 35$  mT/m, and the maximum gradients applied during readout were  $\sim 10$  mT/m. The imaging sequence involved the application of a non-selective RF pulse followed by a constant system delay of 60  $\mu$ s, after which the readout gradients were applied. Following readout, the spins were spoiled by the application of spoiling gradients; refocusing pulses equivalent to the negative of the integral of the readout gradient curve were applied simultaneously.

Images were acquired of the spherical saline phantom to ensure SNR equivalence between the sets. In addition, images of the resolution phantom were also acquired using both sets. Finally, sagittal images using both sets were also acquired of the right knees of six healthy volunteers (age  $26 \pm 4$  years). The sagittal plane was chosen because tibial, femoral, and patellar cartilage can be viewed 'edge on' in that orientation. For image comparisons, anisotropic axial and coronal images were also acquired for one volunteer. All volunteers gave informed consent in accordance with the requirements of the Health and Research Ethics Board at the University of Alberta.

### 4.2.4 Data Analysis

Projection set design (including generation of gradient and refocusing files), image reconstruction, and ROI analysis was performed using custom software utilities (in Matlab). As each projection set acquired a different field of view, image coregistration was done using SPM8 to ensure exactly overlapping images for the dual-window SNR analysis in the human subjects. ROI were drawn over several slices of the reconstructed 3D volume to cover as much tissue as possible. Signal ROI were drawn to cover three locations in each sagittal knee image: the patellar cartilage, the femoral/tibial cartilage junction, and purely femoral cartilage; the ROI were weight-averaged to produce a single SNR value

per subject. All signal ROI were drawn following the visible cartilage contours in the sodium images; coregistration and dual windows in the analysis program allowed exactly matching ROI to be drawn for SNR comparison between the anisotropic and isotropic images. SNR values were calculated by taking the mean value of pixels in signal ROI and divided by the standard deviation of pixel value in an ROI drawn in the image background. As background noise from absolute value images follows a Rayleigh distribution instead of Gaussian, the SNR value was then multiplied by a correction factor of 0.665.

### 4.3 RESULTS

#### 4.3.1 Phantoms

Four sets of images using both protocols were taken of the uniform spherical saline phantom; SNR was calculated for each image. The isotropic projection set produced an average SNR ( $\pm$  SD) of  $114 \pm 3$ , and the anisotropic set produced an SNR of  $113 \pm 3$ . Sodium images of the resolution phantom (Figure 4-3) display the improved in-plane resolution of the anisotropic set over the isotropic set. The anisotropic set was able to achieve  $1.4 \times 1.4 \text{ mm}^2$  effective in-plane resolution, compared to  $2.0 \times 2.0 \text{ mm}^2$  for the isotropic set. The anisotropic

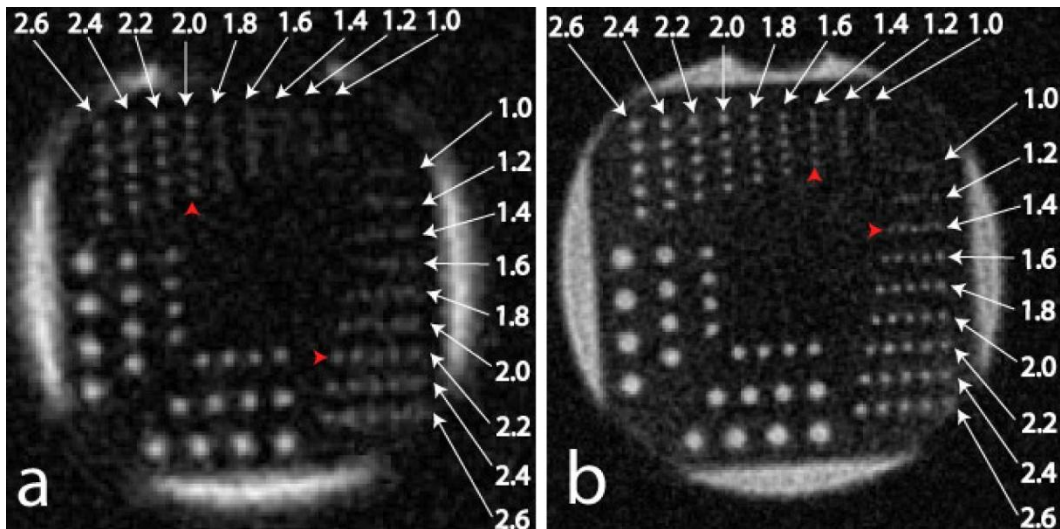


Figure 4-3: Resolution phantom images of (a) the isotropic projection set, and (b) anisotropic resolution set. Effective in-plane resolution is indicated by the red arrows; it is 2.0 mm for the isotropic set compared to 1.4 mm for the anisotropic set. Out-of-plane effective resolution was not measured, however, nominal out-of-plane resolution was 4 mm in (b) compared to 1.3 mm in (a). Nominal voxel volume is equivalent at  $2.56 \text{ mm}^3$  for both projection sets.

set also gives visibly sharper and clearer images.

#### 4.3.2 Human Volunteers

Sagittal sodium imaging of the knee in vivo (Figure 4-4) further demonstrated the benefits of the improved in-plane resolution of the anisotropic acquisitions. The anisotropic images are sharper and clearer than the isotropic images. Furthermore, in the isotropic acquisition, certain areas (e.g. superior lateral condyle) were obscured due to low signal intensity and/or thin cartilage. However, the higher in-plane resolution of the anisotropic scans allowed better discernment of the tissue in these areas. SNR values of the cartilage for both the anisotropic and isotropic protocols were compared using a two-tailed paired t-test; no statistically significant differences were found ( $n = 6$ ,  $p = 0.46$ ).

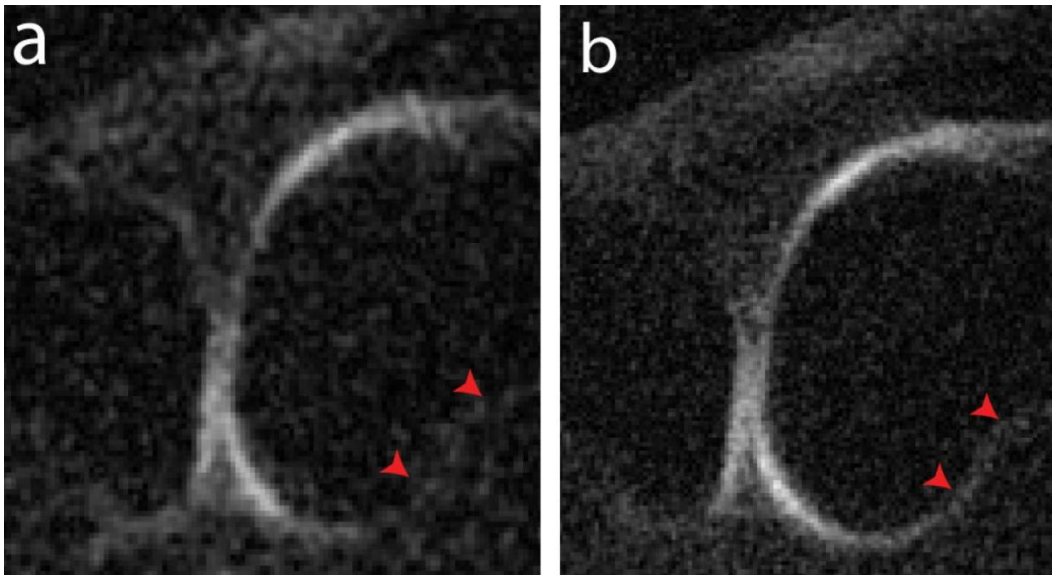


Figure 4-4: Sodium MR images of the human knee in vivo. (a) Isotropic set, and (b) Anisotropic set. Arrows indicate the superior lateral femoral condyle, where tissue is obscured in the isotropic set but not in the anisotropic set.

#### 4.4 DISCUSSION

The experiments on the resolution phantom and the in vivo experiments on the knees of six healthy subjects demonstrated the improved in-plane

resolution of the anisotropic voxels. This voxel shape is especially beneficial for sagittal acquisitions of the knee, as cartilage presented from this orientation is ‘edge-on’, in other words, thin in-plane but running generally perpendicular out-of-plane. As a result, long and skinny voxels should be better fitted to placement in the cartilage tissue than isotropic voxels. This should improve visualization and discernment of structure of the cartilage. To the best of our knowledge, work using anisotropic voxels in 3D-TPI sodium acquisitions has not been previously published.

A major disadvantage of anisotropic voxels in 3D acquisitions is that reconstructions of the acquired volume in other planes (e.g. axial, coronal) will not show the same resolution benefits. While the anisotropic voxels show excellent in-plane resolution, their out-of-plane dimension is almost three times larger than the corresponding dimension in the isotropic scans. The isotropic scans can be reconstructed in any visualization plane and achieve equivalent resolution in all of them (Figure 4-5a-c). In contrast, reconstruction of a sagittal anisotropic scan in another plane results in significant blurring (Figure 4-5e and f). However, if scan time is not an issue, the anisotropic scans can provide superior resolution in any acquisition plane (Figure 4-5g-i).

A challenge of quantification using sodium MRI is the large amount of blurring during reconstruction. This effect is related to the ultrafast T2 relaxation experienced by sodium nuclei. As a result, sodium ‘effective’ resolution (as measured by distinguishing holes in a resolution phantom) is always poorer than ‘nominal’ resolution (as defined by the distance traversed in k-space). In this work, in-plane effective resolution (1.4 and 2.0 mm, for anisotropic and isotropic projection sets respectively) was shown to be at least 1.5 times worse than stated nominal resolution (0.8 and 1.37 mm, respectively). The reduced effective resolution of sodium MRI in relation to anatomy or pathology should be a consideration in future studies involving quantification and/or tissue discernment.

Previous work has displayed sodium 3D-TPI images of the knee (31,40) with isotropic resolutions from 4 to 6 mm (scan times 10-16 min), and one recent work at 7 Tesla (44) has acquired straight radial projection sodium images of the

knee at 1.5 mm isotropic resolution (scan time 14 min). A recent publication showed sodium images of patellar cartilage at 7T using anisotropic voxels of  $1 \times 1 \times 2 \text{ mm}^3$ , with a scan time of 26 minutes and using the CONES acquisition method (56). Anisotropic voxel selection as demonstrated in our research (Figure 4-6) has demonstrable advantages for sodium MRI of the knee, and could improve the already significant benefits of 3D projection imaging demonstrated in the above research.

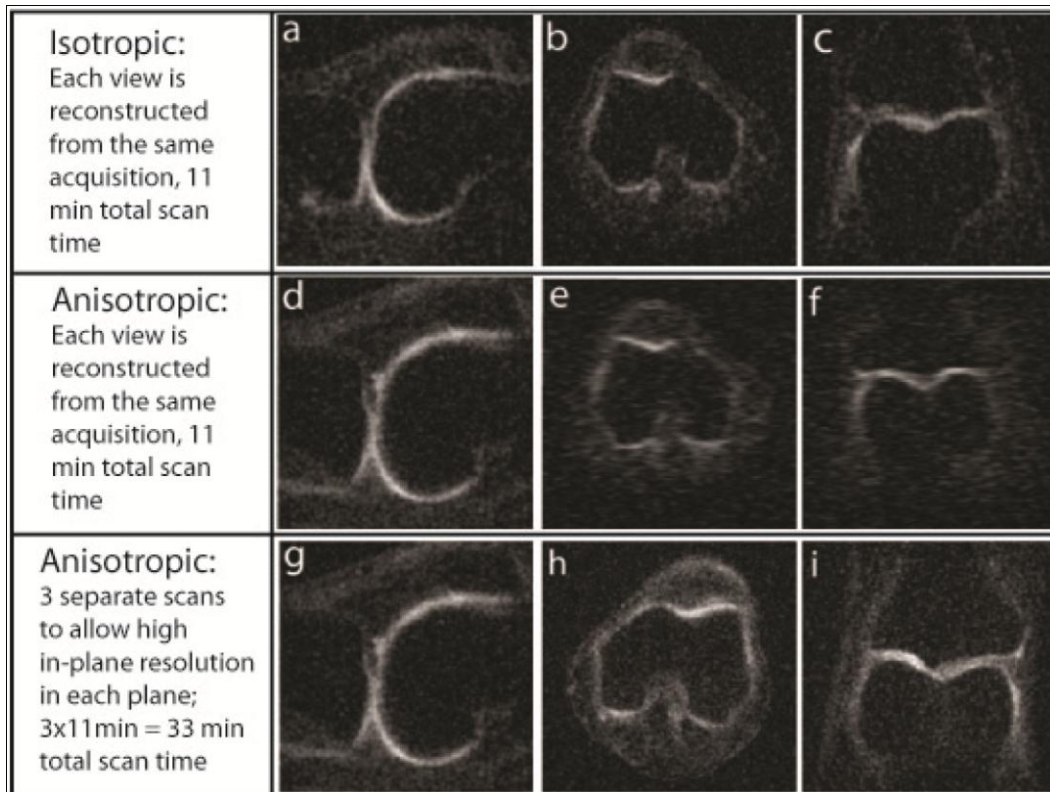


Figure 4-5: Sodium MR images of the human knee in vivo. (a) to (c) Isotropic set; (d) to (e) Anisotropic set from one acquisition of 11 minutes; (g) to (i) Anisotropic set from three separate acquisitions of  $3 \times 11 \text{ min} = 33 \text{ minutes}$  total. As expected, the out-of-plane resolution of the single anisotropic acquisition (e,f) is poorer than that of the single isotropic scan. However, the superior resolution of anisotropic acquisition for any given plane of acquisition is evident by the images in the (h) axial and (i) coronal planes.

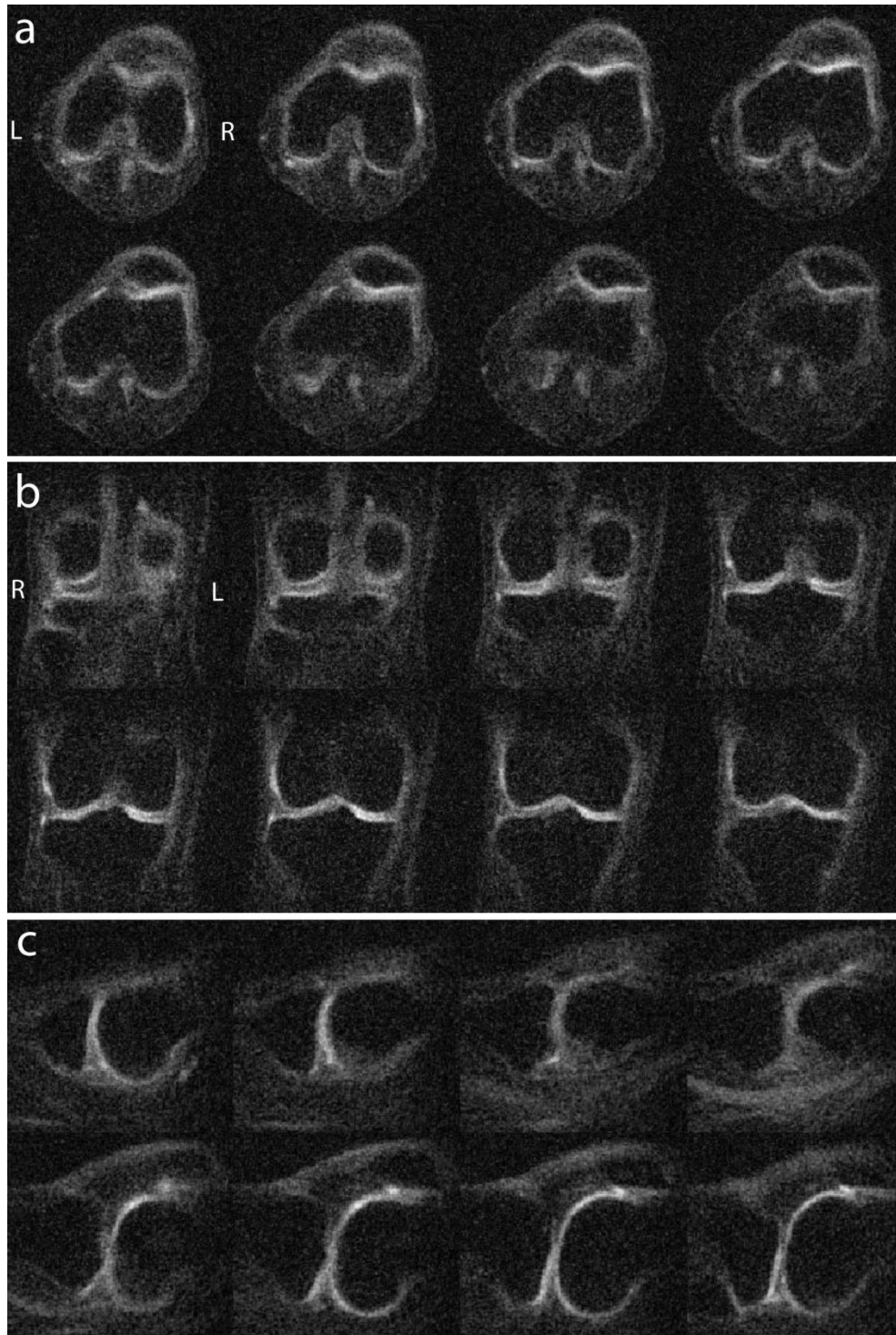


Figure 4-6: Sodium images of the knee of a healthy volunteer at 4.7 T using anisotropic voxels (9000 projections, nominal voxel size  $0.8 \times 0.8 \times 4.0 \text{ mm}^3$ ). (a) Axial, (b) coronal, and (c) sagittal planes were acquired separately in 11 minutes each. Apparent distance between slices (calculated by taking the field of view, dividing by inverse filter size, and multiplying by the number of reconstructed slices between the displayed slices) is 5 mm for (a) and (b), and 4 mm for (c). SNR in the cartilage is  $\sim 8$ . Left and right sides are marked by L and R letters for the axial and coronal orientations.

## **4.5 CONCLUSIONS**

Anisotropic voxel acquisition using 3D-TPI for sodium imaging of the human knee can produce excellent results in terms of visualization and improved tissue discernment. While it has a disadvantage in that it displays extra blurring in out-of-plane reconstructions due to a larger out-of-plane dimension, it can be useful in specific acquisitions where damage/lesion location is already suspected and better in-plane resolution is required without sacrificing signal, or if the natural contours of the tissue support high voxel fitting efficiency over isotropic scans. Future work will concentrate on investigating any quantitative benefits of anisotropic voxels for characterization of degraded cartilage in the human knee.

## Chapter 5

### Discussion and Conclusions

#### 5.1 Thesis Summary

In this thesis, the methods, materials and optimizations necessary to produce high quality sodium MR images of the human knee in vivo were examined. The images have the potential to allow early diagnosis of osteoarthritis in vulnerable patient populations, or to evaluate the efficacy of new pharmacological treatments of osteoarthritis. The optimization techniques presented here allow the acquisition of extremely high quality images. To the best of the author's knowledge, only one publication on sodium MRI (56) exists with images at better resolution than the  $2.56 \text{ mm}^3$  presented here, and that work was done at 7T (much higher than the 4.7T magnet at the University of Alberta). A summary of sodium images of the human knee in-vivo is given in Figure 5-1.

Chapter 2 deals with the preliminary steps taken during the course of this thesis. Considerations for the practical construction of a high pass birdcage coil were explained, and a formula for efficient modifications of resonant frequency was derived. An explanation of the design and construction of all phantoms in use in this research was given, including materials, examples of use, and possible future applications. Finally, a detailed examination of sodium relaxation in cartilage for both the T1 and T2 domains was shown. T1 values for sodium in cartilage in vivo were determined for the first time (to the best of the authors knowledge) at any field strength. T2 relaxation was examined, and the determination was made that significant impediments exist for the accurate measurement of T2 with the methodology used. A possible reason for the problems was given as quadrupolar splitting.

Chapter 3 examines the benefits of sacrificing low relaxation weighting (known as tissue sodium concentration or TSC scans) in order to collect extra averages through a steady state acquisition protocol known as projection

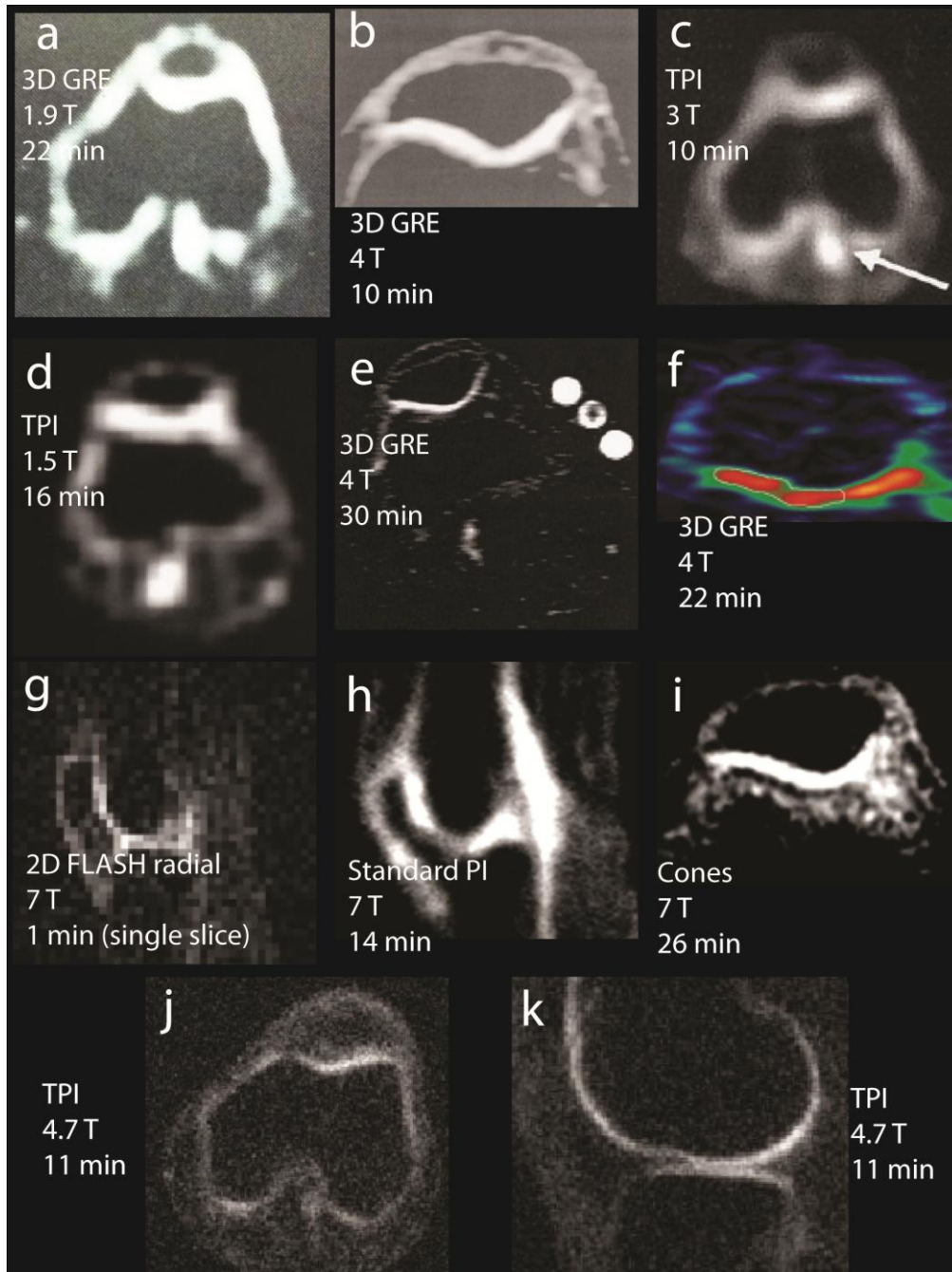


Figure 5-1: Comparative sodium images of the human knee in vivo, adapted from (a) Granot (1988), (b) Reddy (1998), (c) Borthakur (1999), (d) Constantinides (2000), (e) Shapiro (2002), (f) Wheaton (2004), (g) Rong (2008), (h) Wang (2009), and (i) Staroswiecki (2010). Images displayed in (j) and (k) are taken from the anisotropic protocol in Chapter 4.

Reference	Voxel Size (mm <sup>3</sup> )	Time	B <sub>0</sub> (T)
Granot (1988): A	97.7	22 min	1.9
Reddy (1998): B	12.5	10 min	4
Borthakur (1999): C	64.0	10 min	3
Constantinides (2000): D	216.0	16 min	1.5
Shapiro (2002): E	14.1	30 min	4
Wheaton (2004): F	5.5	22 min	4
Rong (2008): G	441.8	1 min (1 slice)	7
Wang (2009): H	3.4	14 min	7
Staroswiecki (2010): I	2.0	26 min	7
Watts (2010) axial: J	2.6	11 min	4.7
Watts (2010) sagittal: K	2.6	11 min	4.7

Table 5-1: References, including voxel sizes, imaging times, and field strengths for the images in Figure 5-1.

acquisition in the steady state, or PASS. This was done under the radiofrequency power constraints (also known as specific absorption rate or SAR constraints) imposed by scanning at high field. The relaxation parameters for sodium were used to conduct quantum mechanical simulations of sodium behavior. Based on the simulations, two protocols were chosen, each with equal SAR deposition and scan time. A significant SNR benefit of 27% was determined through the use of the PASS protocol, which, despite the requirement to use a longer pulse length (hence longer TE) to remain below SAR restrictions, is able to improve image quality through the increased averaging possible when a lower TR is used. This technique was used to produce high quality sodium images of the knee at 4.7T in a clinically feasible scan time of 9 minutes.

Chapter 4 involved the acquisition of k-space while scaling the out-of-plane gradient. This produced an anisotropic acquisition of k-space, which translated to a voxel shape that was physically anisotropic (smaller in-plane dimensions, with a longer out-of-plane dimension). Two projection sets were created, one isotropic and one anisotropic, with equivalent voxel volume, readout length, projections, and twist. These sets were used to acquire images of a uniform saline phantom, a saline resolution phantom, and of the right knees of six

healthy human volunteers. SNR equivalence was determined between the sets for both the phantoms and the human scans, and higher in-plane resolution using the resolution phantom was demonstrated. In addition, higher quality in-plane images of the human knee were demonstrated using the anisotropic set. Out-of-plane reconstructions of the anisotropic acquisition were demonstrated to be poorer than those of the isotropic acquisition.

## **5.2 Future Directions**

The methods and optimizations outlined in this thesis, while a good start towards practical achievement of high quality sodium MRI of the knee, are far from representing a finished product. The following concerns could be among the first addressed in order to achieve even more benefit from sodium scanning of the knee.

### **5.2.1 Concerning Relaxation**

The interesting results regarding sodium relaxation in the knee, in both the T1 and T2 domains, may deserve more attention. Some regional variations were noted in relaxation values dependent on where the ROI were drawn; a complete T1 and T2 mapping project of all the cartilage in the knee area may give interesting results as well as prove useful in further research. In addition, to the best of the author's knowledge, the relaxation properties of synovial fluid have never been experimentally determined. The assumption has been made that, as a free moving fluid, synovial fluid must relax monoexponentially at longish T1 and T2 (saline at 4.7T relaxes at  $T1 = T2 = \sim 53$  ms). However, this may not necessarily be the case. Partial volume effects with synovial fluid may be partly responsible for the disagreement between observation and simulation of PASS SNR benefits in Chapter 3; knowledge of the relaxation of synovial fluid may help to reconcile this disparity. It might also allow the use of optimized inversion recovery sequences to suppress the interference of fluid in other applications; inversion recovery has been used by other research in sodium knee imaging (44).



Figure 5-2: The double tuned coil used to acquire the images in Figures 5-3a and 5-4.

### 5.2.2 Concerning Dual-tuned Coils

The ability to acquire a proton anatomical scan in conjunction with a sodium scan is advantageous. The proton scan allows pathology and small anatomies to be more easily distinguished; the sodium scans can be later co-registered to the proton scans. In such a scheme, the ‘best of both worlds’ could be achieved; all the resolution and high image quality of a proton scan, but the biological information given by a sodium scan.

While two separate coils can be used to acquire the scans, this is problematic both in terms of time and quality. Patient time is significantly increased by the need to remove the patient, change coils (possibly including changing cabling or other hardware), and re-insert the patient back into the magnet. In addition, the action of moving the anatomy into a new

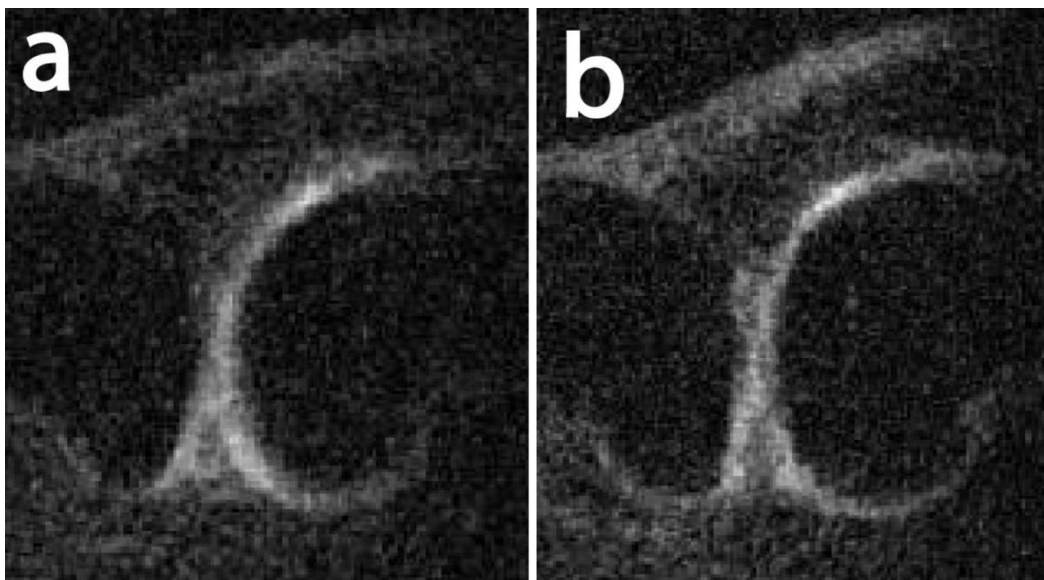


Figure 5-3: Sodium images of knee cartilage using (a) the concentric double tuned coil, and (b) the single tuned coil. As different subjects were used for the acquisition, SNR was not compared, but image quality can be seen to be comparable.

coil may result in changes to orientation or flexion that could result in losing the benefits of co-registration. As such, a dual or double-tuned coil would be desirable.

Several such designs have been proposed by other research (68-71); at the time of this writing, investigations here are being conducted into both a double tuned concentric design (69) (see Figure 5-2) and a dual-tuned design which allows identical  $B_1$  field (71). Preliminary images for the concentric design show excellent promise, the sodium images are of comparable quality to those obtained with a single tuned coil (see Figure 5-3). The proton images, while serviceable, are not spectacular; significant homogeneity problems are present. This is noticeable by the marked differences in brightness in certain areas of the tissue (Figure 5-4). Contrast may not be optimized for cartilage.



Figure 5-4 (left): A proton image (fast spin echo, TE = 15 ms, TR = 4 s) of a knee using the double tuned concentric coil. Variations in signal strength are seen within similar tissues, indicating imperfect homogeneity in the coil.

The ability to conduct both proton and sodium scans of the knee without changing coils will vastly improve the patient friendliness of the protocol, in addition to a significant savings of ‘in-magnet’ time. The study of cartilage at 4.7 T may have intrinsic value of its own; previous research has found clinical benefits to cartilage imaging at field strengths greater than 1.5 T. (8-9)

### **5.2.3 Concerning PASS optimization at 3T**

As the Peter Allen MR Research Center in Edmonton currently houses a 3T magnet and a single tuned sodium knee coil has already been built, it would be a relatively simple matter to conduct the same PASS versus TSC experiment of Chapter 3 there. The 3T magnet has a dual Varian Inova/SMIS console, along with gradients from Magnex (Oxford, UK). The RF amplifier is made by American Microwave Technology (currently Herley, Lancaster, PA, USA) and has one transmit channel capable of a maximum transmit power of 8 kW. Porting of the PASS and TSC protocols to the 3T machine would allow verification of the 3T simulations, and provide a more practical protocol for clinicians, who may decide to take advantage of sodium scanning in the shift of clinical scanning to 3T. Imaging benefits of 3T over 1.5T have already been determined for proton scans of middle to late stage osteoarthritis (8,72).

### **5.2.4 Concerning Anisotropic Voxel Applications**

As explained in Chapter 4, there was no SNR benefit associated with the use of anisotropic voxels in cartilage at 4.7T; however, it was better able to distinguish the cartilage. The voxels used had a length/width ratio of 5, and are quite long and thin. While this was done to improve in-plane resolution to the best value possible, it may not represent the best option for voxel fitting within the tissue. A length/width ratio of 3 or even 2 may allow ‘best’ fitting efficiency for the cartilage of the knee. In that event, partial volume effects may be reduced to the point where a significant SNR benefit can be measured of anisotropic voxels over isotropic ones. Where dual or double tuned coils can be used for the acquisitions, the ability to ‘match’ anisotropy of the sodium voxels with their

proton counterparts can be advantageous during co-registration, as explained in other work (18).

### **5.3 Final Commentary**

The optimizations presented in this thesis have been demonstrated to produce excellent quality sodium MR images of human knee cartilage in vivo. Based on these results, and with further development and research, there should be no reason why technical issues relating to image quality should prevent the future use of sodium MRI in a clinical environment.

As a final note, the practical aspects of sodium MR imaging discussed here and applied specifically to knee imaging are not necessarily limited to such. It is hoped that this thesis can serve as a ‘roadmap’ for further study of sodium MRI of the knee, or for a project involving the study of sodium in other pathologies or anatomies. Possibilities for new projects include breast imaging (sodium has been studied in cancer in several investigations (73-76)) and wrist imaging, among others.

## APPENDICES

### **6.0 Appendix Preface**

Throughout the course of this thesis, the software designed and implemented by R. Stobbe was extremely useful. It was used for projection set design and implementation, for image reconstruction and display, for the simulation completion and display, and for ROI analysis of images. The purpose of this appendix is to provide a short “user’s guide” for each of the main programs used with respect to sodium imaging of the knee in particular.

# Appendix 1

## 6.1 Projection set design + construction using NL-PRODS/AID

The program used for projection set design and construction in this thesis was NL-PRODS (non linear projection design software) v. 8.7. NL-PRODS is now known as AID (arbitrary image development). The key parameters of any projection set are first listed below.

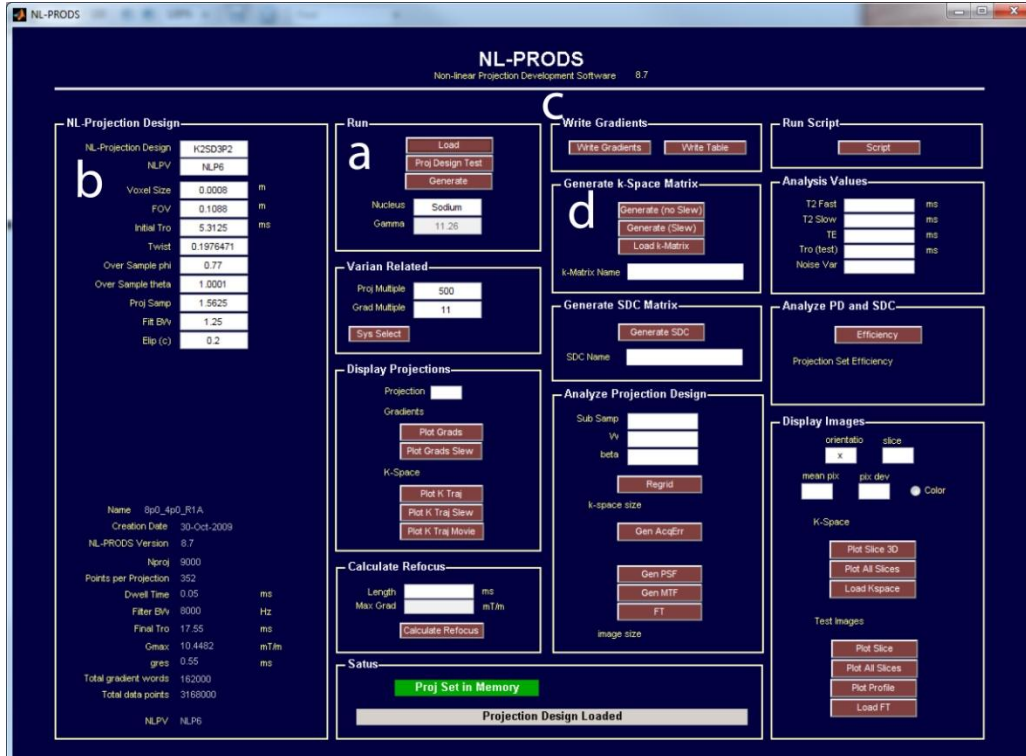


Figure A-1: A screenshot of NL-PRODS.

Voxel Size: defines in-plane resolution. For example, voxel size = 0.001 means in-plane resolution is 1mm\*1mm.

FOV: defines the field of view of the projection set. Ex: 0.12 means there is a 12 cm FOV in the isocentre.

Initial Tro: affects final Tro, which is the time spent during readout.

Twist: the fraction of the projection that is 'straight', as opposed to being 'twisted'. For example, 0.1 twist means the projection goes straight for 10% of the distance, then twists around for the rest of the k space.

Oversample Phi: the ratio of ‘extra’ cones that there are, compared to what there should be in an isotropic voxel k-space. Theoretically, this should match the Elip value if the Elip value is greater than 1.

Oversample Theta: the ratio of ‘extra’ projections there are within a given cone. A value of 1 is usually best.

Proj Samp: A ratio of the number of points taken along a certain projection to a reference value. A higher proj samp value means more points per projection.

Filt BW: relates to the bandwidth of the anti-aliasing filters on the receive channel. This value must always be  $> 1.1$ .

Elip (c): refers to the scaling factor for the out-of-plane gradients (i.e. distance travelled in the out-of-plane dimension in k-space relative to the in-plane dimensions). A value of 1 means that out-of-plane resolution equals in-plane resolution (i.e. isotropic voxels). A value between 0 and 1 indicates greater out-of-plane size (pencil voxels), while a value greater than 1 indicates lesser out-of-plane size (pancake voxels). Ex: voxel size 0.001, elip =2 means true voxel size is 1mm\*1mm\*0.5mm. Ex2: voxel size = 0.001, elip = 0.25, true voxel size = 1mm\*1mm\*4mm.

#### STEPS TO CREATING A NEW PROJECTION SET

1. Under the ‘run’ box (denoted by (a) in Figure A-1), click ‘load’ to get the parameter file for a previously created projection set in memory. It is simpler and faster to modify an existing projection set than to create a new one from scratch.
2. Choose your system file by clicking the ‘sys select’ in the ‘Varian related’ box just under the ‘Run’ box.
3. Once loaded, the projection set parameters will arise in the NL projection design box (denoted by (b) in Figure A-1). These parameters define the salient properties of the projection set. The following order is suggested when modifying a design.
  - a. Choose your voxel size and elip values. These define the basic parameters of your set, and are ‘nonnegotiable’.

- b. Choose your FOV.
  - c. Choose your twist value. This will depend on the application. Low twist is generally better, but at times high twist can be a good way to get 'space' so that other parameters can be reduced. Example: for high res applications, high gradients are needed, but if they're too high (and you need to reduce them) you can do it by increasing twist, then you can increase readout, and this will reduce the level of gradient needed.
  - d. Choose your initial Tro value. Should result in a final Tro that is 'ballpark' for the TR wanted.
  - e. Choose your Filt BW value. This should put your Filter BW (bottom) near to but just under a multiple of 1000.
  - f. Choose your proj samp value. Dwell time should be manageable (no more than 3-4 decimal places) and Nproj (number of projections) is 'ballpark'. Higher is better, but it increases gradient words.
  - g. Choose your oversample phi value. This should be greater than one and not less than your elip value. But sometimes you have to reduce it below in order to get your Nproj right. Reduce it to a point where Nproj is just less than you need.
  - h. Choose your oversample theta value. This should be slightly increased to get to the number of projections you want, according to what you did in step g.
  - i. Look at your Final Tro and your Gmax and readjust, starting from step c.
4. After changing parameters, click on 'proj design test' in the 'Run' box. This updates the final set parameters in the bottom left.
  5. Once the desired projection set has been achieved (also ensuring that 'Proj Multiple' under 'Varian Related' can be evenly divided into Nproj-this will define how the projections are acquired during scanning later), click 'Generate' under 'Run'.
  6. Create a new design folder (naming it appropriately) and save the projection design file in it.
  7. Click 'ok' when the program asks to write the gradients. A folder in the newly created design folder will automatically be created for them. The gradients can be created later using 'write gradients' in the 'Write Gradients' box (denoted by (c) in Figure A-1).

8. Click 'generate (Slew)' in the 'Generate k-space matrix' box (denoted by (d) above). Choose the appropriate slew rate file.
9. Click on the projection design folder and save the k-matrix.
10. Click 'Generate SDC' in the 'Generate SDC matrix' box (under the 'Generate k-space matrix' box). Select the design folder, then 'Refocus and Regrid', then 'Regrid', then click 'ok'. For 'Use Initial SDC Matrix?' click 'No'. Then go to SDC Methods and click on the desired method.
11. In the 'Calculate Refocus' box, enter a variety of lengths (lengths of 1, 2, 3, 5, and 10 were commonly used) and click 'calculate refocus'. Save each refocus pulse in the design folder.

Once a projection set has been created, the gradient and refocus files must be transferred over to the Varian console and a macro created to run the scan. The preferred program for the file transfer was WinSCP.

## Appendix 2

### 6.2 Image Reconstruction using TRICS/AIC

The program used for image reconstruction in this thesis was Three Dimensional Image Creation Software (TRICS), version 6.3. This program is now known as Arbitrary Image Creation (AIC). TRICS takes the raw data FIDs of the acquisitions and imports them into processing memory. The FID data is regridded onto a three dimensional k-space volume, which is then divided into a series of slices according to the size of the inverse filter desired. Inverse filters were created in NL-PRODS.

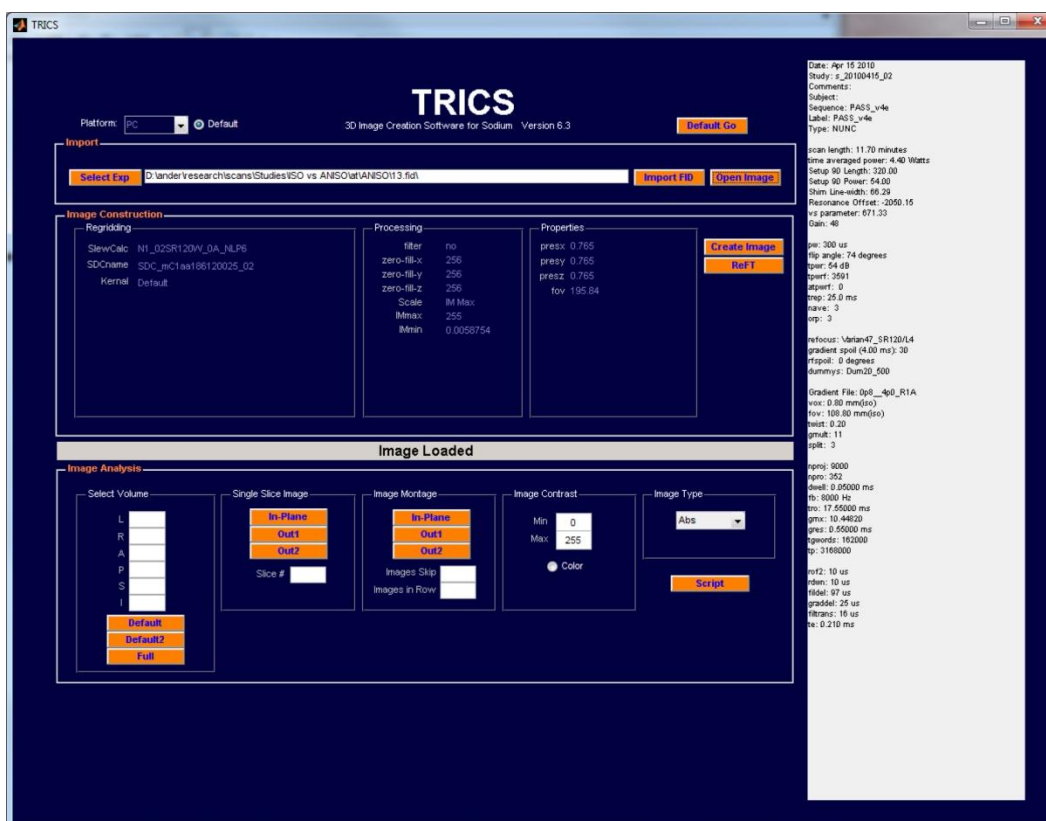


Figure A-2: A screenshot of TRICS.

### STEPS TO RECONSTRUCTING AN IMAGE

1. First, the FID of the acquired data should be transferred to the host computer.

2. Click 'select experiment' under the 'Import' box. Select the FID of the experiment whose image is desired.
3. Click 'Import FID' under the 'Import' box.
4. Once the FID is imported, click 'Create Image' under the 'Image Construction' box.
5. Select the correct 'regrid SDC' from under the Regrid folder in the projection design folder.
6. Answer the following questions:
  - a. User defined operation? No.
  - b. Filter? No.
  - c. Zero-fill? Here, choose a number greater than the numbers displayed, for which there is an inverse filter created in NL-PRODS and stored in NL-PRODS/Inversion Filters/Current Files.
  - d. Scaling? Choose 'IM max' for most reconstructions. This scales the brightest pixel as 255 and the darkest pixel as 0. A choice of 'User Max' allows absolute scaling, choose a value greater than the absolute value displayed. 'User Max' is most useful for relaxation experiments, as constant scaling can be maintained.
7. Save image.
8. Choose display parameters under 'Select Volume' in the 'Image Analysis' box. Single slices or image montages can be seen, view them by clicking 'In-plane'. Out of plane reconstructions are possible by clicking 'Out1' and 'Out2'.
9. External scripts can be run by clicking 'Script' on the bottom right of the 'Image Analysis' box.
10. Previously created images can be viewed using 'Open Image' in the 'Import' box.

## Appendix 3

### 6.3 Simulations Using Triple-S

For the simulations of sodium behavior explained in Chapter 3, a program called Triple-S, v 1.B, was used. In triple-S, a spectral density model of sodium relaxation can be created and used along with a specific sequence to model sodium behavior.

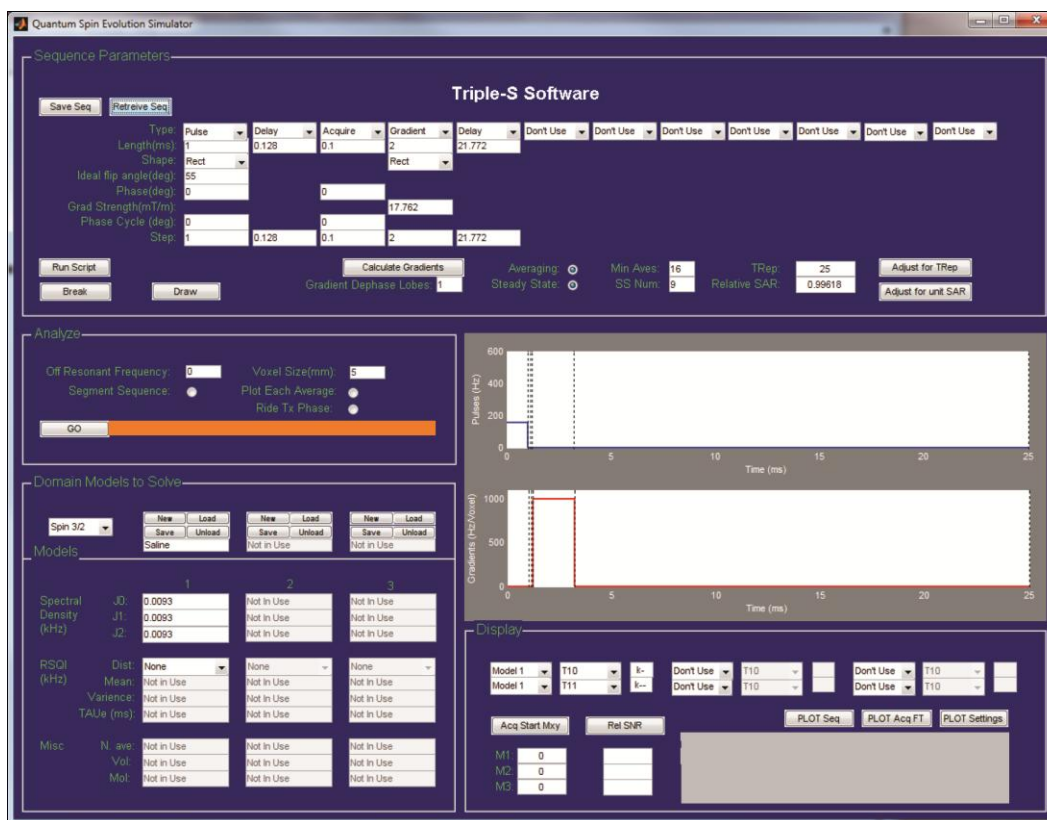


Figure A-3: A screenshot of Triple-S.

Several actions are possible in Triple-S.

1. A spectral density model can be created by entering the parameters J0, J1, and J2 under the 'Models' box. This model can be saved by clicking 'save' under 'Domain Models to Solve.'
2. A previous sequence can be retrieved by using the 'Retrieve Seq' button under the 'Sequence Parameters' box.

3. A new sequence can be designed by changing the value and order of the parameters type, length, and shape under 'Sequence Parameters'. A new sequence can be saved by clicking 'Save Seq' in the same box.
4. To run a script, click 'Run Script' under 'Sequence Parameters'.
5. While a script is most efficient for bulk simulations, the simulation of a specific set of parameters can be entered manually. Click 'load' under 'domain models to solve' to load a relaxation model. Click 'GO' under the 'Analyze' box to simulate the point. Click 'Acq Start Mxy' to see the value of magnetization for that point.

## Appendix 4

### 6.4 Simulation Display using Marconi

The simulations of Triple-S were displayed using a program called Marconi v 1.0. It loads the sequence produced by Triple-S, then, based on a set of display parameters, outputs a display based on a script analysis of the sequence. SNR benefit, optimal flip angle, and relaxation weighting are some of the scripts available for use; these are displayed in Chapter 3.

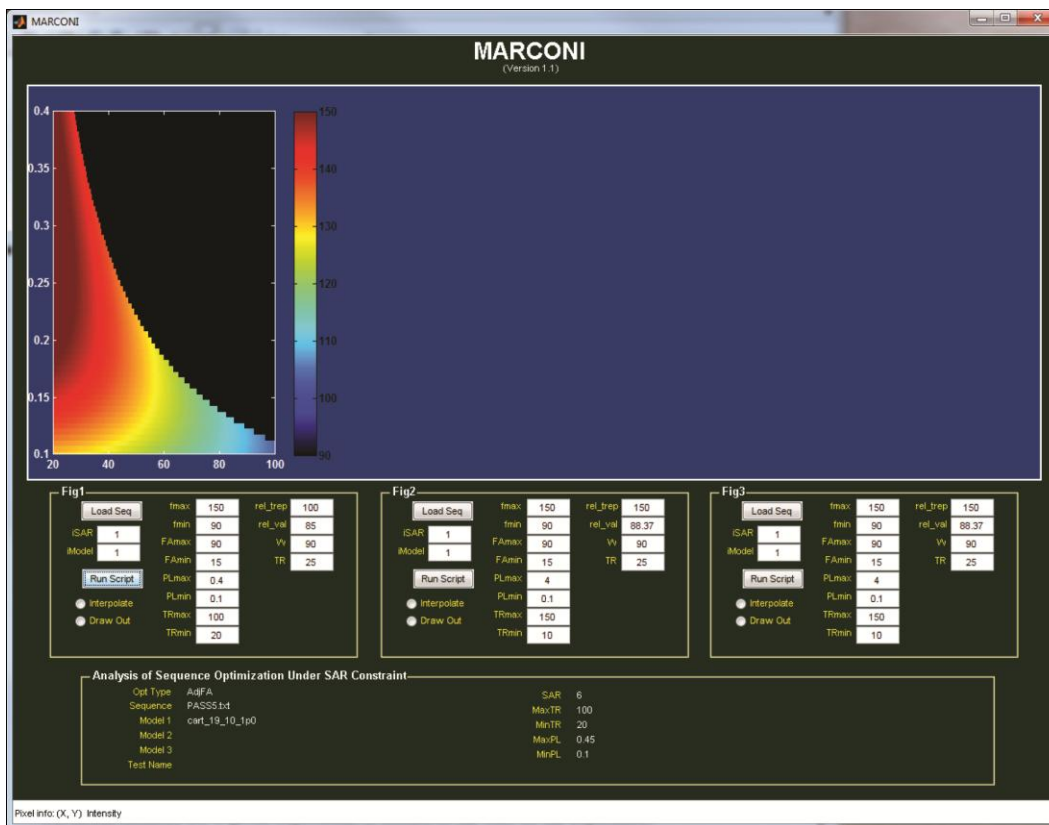


Figure A-4: A screenshot of MARCONI.

#### TO VIEW A SET OF SIMULATIONS

1. Load the sequence by clicking 'Load Seq'.
2. Change the display parameters to those which will best show the results.
  - a. Fmax: refers to the upper limit of the simulation display parameter.
  - b. Fmin: the lower limit of the simulation display parameter.

- c. F<sub>Amax</sub>: the maximum flip angle for which simulation values are displayed.
  - d. F<sub>Amin</sub>: the minimum flip angle for which simulation values displayed
  - e. PL<sub>max</sub>: Pulse length display maximum.
  - f. PL<sub>min</sub>: Pulse length display minimum.
  - g. TR<sub>max</sub>: maximum TR displayed.
  - h. TR<sub>min</sub>: minimum TR displayed.
  - i. Rel<sub>trep</sub>: The TR value for which a relative reference value of 100% is desired.
  - j. Rel<sub>val</sub>: the value of Acq Start Mxy (see action 5 under Appendix 3 above) at TR = Rel<sub>trep</sub> for which a relative reference value of 100% is desired.
3. Display a given set of simulations by clicking 'Run Script'. Then, choose the desired analysis script. Scripts used in this thesis fell under Scripts/Version2/3D Plots/.
  4. For SNR benefit display, in order to have one protocol at a relative value of 100%, follow action 5 of Appendix 3 above. Once the Acq Start Mxy value is determined, enter that value for rel\_val and the TR value used in action 5 as rel\_trep. Then run the SNR script again; the data point simulated in action 5 will be at a relative value of 100%.
  5. Note too that three separate windows can be used to simultaneously display the results of 3 separate analysis scripts. However, the sequence must be loaded separately as in step 1 each time.
  6. Click 'draw out' as an option before running a script to have the results written to a outside figure which can be more easily saved for use in a manuscript.

## Appendix 5

### 6.5 ROI Analysis of Images using Galileo

The program used for all ROI analysis in this thesis was Galileo v 2.D. Galileo possesses dual windows for matching analysis, as well as a variety of ROI drawing tools and the ability to run external scripts. It accepts as input only the ANALYZE file format, which can be exported from TRICS using the ‘script’ function (Appendix 2, step 9).

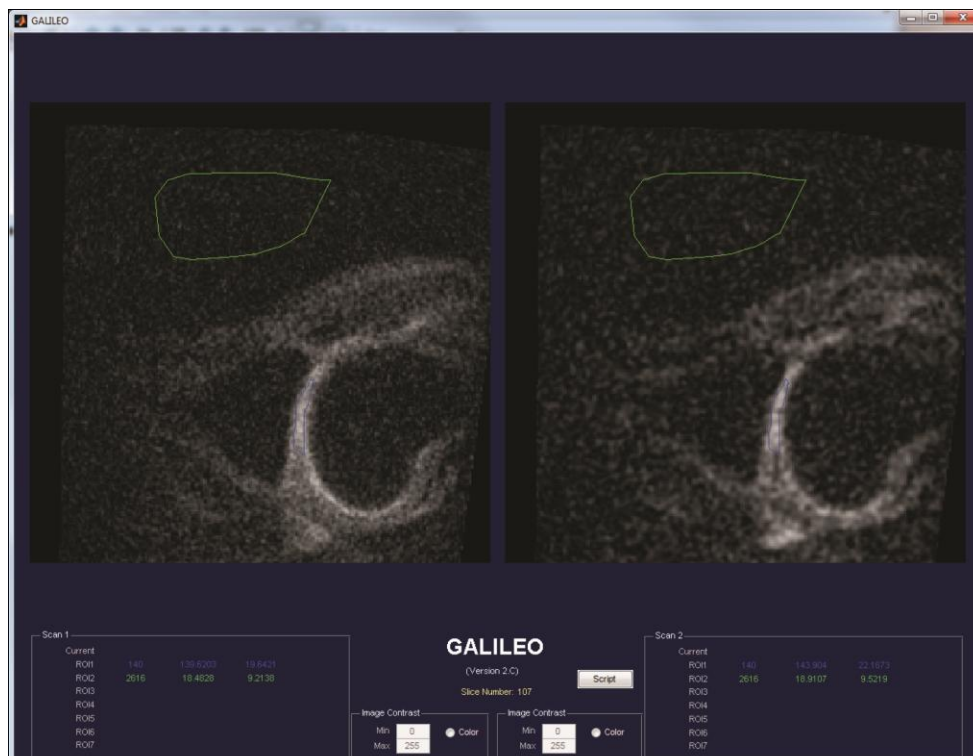


Figure A-5: A screenshot of GALILEO.

1. To load an image, right click inside either the ‘Scan 1’ or ‘Scan 2’ box. Select the desired image.
2. Once an image is loaded, a variety of ROI tools can be used for analysis. The ROI tools and their keyboard shortcuts are listed below.
  - a. ‘z’: new ROI
  - b. ‘d’: drawing tool (left click starts draw, right click finishes)
  - c. ‘a’: seeding (values > entered value)

- d. 's': seeding (values < entered value)
  - e. 'f': calculation
  - f. 'v': discard ROI
  - g. 'c': keep ROI
  - h. 'l': load ROI
  - i. 'p': plot
  - j. 'h': hide ROI
  - k. 'g': show ROI
3. To save a given ROI, right click on the ROI name (e.g.ROI1) in the 'Scan' box for that ROI. Click 'save'.
  4. To delete a given ROI, right click on the ROI name (e.g.ROI1) in the 'Scan' box for that ROI. Click 'delete'.
  5. To move a given ROI on the image without changing its shape, right click on the ROI name (e.g.ROI1) in the 'Scan' box for that ROI. Click 'edit'. Use the keys i, j, k, and m to move the ROI up, left, right, and down respectively.

## REFERENCES

1. Centers for Disease Control A. Prevalence of disabilities and associated health conditions among adults: United States, 1999. *Morbidity and Mortality Weekly Report* 2001;50(7):120-125.
2. Peat G, McCarney R, Croft P. Knee pain and osteoarthritis in older adults: a review of community burden and current use of primary health care. *Ann Rheum Dis* 2001;60(2):91-97.
3. Flood J. The role of acetaminophen in the treatment of osteoarthritis. *Am J Manag Care* 2010;16 Suppl Management:S48-54.
4. Reginster JY, Deroisy R, Rovati LC, Lee RL, Lejeune E, Bruyere O, Giacovelli G, Henrotin Y, Dacre JE, Gossett C. Long-term effects of glucosamine sulphate on osteoarthritis progression: a randomised, placebo-controlled clinical trial. *Lancet* 2001;357(9252):251-256.
5. Recht MP, Resnick D. MR Imaging of Articular Cartilage - Current State and Future Directions. *Am J Roentgenol* 1994;163(2):283-290.
6. Borthakur A, Shapiro EM, Beers J, Kudchodkar S, Kneeland JB, Reddy R. Sensitivity of MRI to proteoglycan depletion in cartilage: comparison of sodium and proton MRI. *Osteoarthritis and Cartilage* 2000;8(4):288-293.
7. Reichenbach S, Yang M, Eckstein F, Niu J, Hunter DJ, McLennan CE, Guermazi A, Roemer F, Hudelmaier M, Aliabadi P, Felson DT. Does cartilage volume or thickness distinguish knees with and without mild radiographic osteoarthritis? The Framingham Study. *Ann Rheum Dis* 2010;69(1):143-149.
8. Link TM, Sell CA, Masi JN, Phan C, Newitt D, Steinbach L, Majumdar S. 3.0 vs 1.5 T MRI in the detection of focal cartilage pathology - ROC analysis in an experimental model. *Osteoarthritis and Cartilage* 2006;14(1):63-70.
9. Wong S, Steinbach L, Zhao J, Stehling C, Ma CB, Link TM. Comparative study of imaging at 3.0 T versus 1.5 T of the knee. *Skeletal Radiol* 2009;38(8):761-769.
10. Borthakur A, Mellon E, Niyogi S, Witschey W, Kneeland JB, Reddy R. Sodium and T-1 rho MRI for molecular and diagnostic imaging of articular cartilage. *NMR Biomed* 2006;19(7):781-821.
11. Bacic G. MRI Contrast Enhanced Study of Cartilage Proteoglycan Degradation in the Rabbit Knee. *Magnetic Resonance in Medicine* 1997;37:764-768.
12. Lesperance LM, Gray ML, Burstein D. Determination of Fixed Charge Density in Cartilage using Nuclear Magnetic Resonance. *J Orthop Res* 1992;10(1):1-13.
13. Reddy R, Insko EK, Noyszewski EA, Dandora R, Kneeland JB, Leigh JS. Sodium MRI of human articular cartilage in vivo. *Magnetic Resonance in Medicine* 1998;39(5):697-701.
14. Wheaton AJ, Borthakur A, Shapiro EM, Regatte RR, Akella SVS, Kneeland JB, Reddy R. Proteoglycan loss in human knee cartilage: Quantitation with sodium MR imaging - Feasibility study. *Radiology* 2004;231(3):900-905.
15. Bashir A, Gray ML, Boutin RD, Burstein D. Glycosaminoglycan in articular cartilage: In vivo assessment with delayed Gd(DTPA)(2-)-enhanced MR imaging. *Radiology* 1997;205(2):551-558.
16. Tiderius CJ, Olsson LE, Leander P, Ekberg O, Dahlberg L. Delayed gadolinium-enhanced MRI of cartilage (dGEMRIC) in early knee osteoarthritis. *Magnetic Resonance in Medicine* 2003;49(3):488-492.

17. Parrish TB, Fieno DS, Fitzgerald SW, Judd RM. Theoretical basis for sodium and potassium MRI of the human heart at 1.5 T. *Magnetic Resonance in Medicine* 1997;38(4):653-661.
18. Stobbe R. Sodium MRI Optimization for the Human Head with Application to Acute Stroke. Edmonton: University of Alberta; 2010.
19. Dieppe P, Cushnaghan J, Young P, Kirwan J. Prediction of the Progression of Joint Space Narrowing in Osteoarthritis of the Knee by Bone-Scintigraphy. *Ann Rheum Dis* 1993;52(8):557-563.
20. Sarzi-Puttini P, Cimmino MA, Scarpa R, Caporali R, Parazzini F, Zaninelli A, Atzeni F, Canesi B. Osteoarthritis: An overview of the disease and its treatment strategies. *Semin Arthritis Rheum* 2005;35(1):1-10.
21. Garstang SV, Stitik TP. Osteoarthritis - Epidemiology, risk factors, and pathophysiology. *Am J Phys Med Rehabil* 2006;85(11):S2-S11.
22. Towheed TE, Hochberg MC. A systematic review of randomized controlled trials of pharmacological therapy in osteoarthritis of the knee, with an emphasis on trial methodology. *Semin Arthritis Rheum* 1997;26(5):755-770.
23. Hochberg MC, Dougados M. Pharmacological therapy of osteoarthritis. *Best Pract Res Clin Rheumatol* 2001;15(4):583-593.
24. Palmer SH. Total Knee Arthroplasty. 2009.
25. Rat A-C, Guillemin F, Osnowycz G, Delagoutte J-P, Cuny C, Mainard D, Baumann C. Total hip or knee replacement for osteoarthritis: mid- and long-term quality of life. *Arthritis Care Res (Hoboken)* 2010;62(1):54-62.
26. Suarez-Almazor ME, Richardson M, Kroll TL, Sharf BF. A Qualitative Analysis of Decision-Making for Total Knee Replacement in Patients With Osteoarthritis. *JCR-J Clin Rheumatol* 2010;16(4):158-163.
27. Bohm ER, Dunbar M, Pitman D, Rhule C, Araneta J. Experience with physician assistants in a Canadian arthroplasty program. *Can J Surg* 2010;53(2):103-108.
28. Martini T, and McKinley. *Human Anatomy: Prentice-Hall, Inc.*; 2000.
29. Shapiro EM, Borthakur A, Gougoutas A, Reddy R. Na-23 MRI accurately measures fixed charge density in articular cartilage. *Magnetic Resonance in Medicine* 2002;47(2):284-291.
30. Shapiro EM, Borthakur A, Dandora R, Kriss A, Leigh JS, Reddy R. Sodium visibility and quantitation in intact bovine articular cartilage using high field Na-23 MRI and MRS. *Journal of Magnetic Resonance* 2000;142(1):24-31.
31. Constantinides CD, Gillen JS, Boada FE, Pomper MG, Bottomley PA. Human skeletal muscle: Sodium MR imaging and quantification-potential applications in exercise and disease. *Radiology* 2000;216(2):559-568.
32. Allen P. BME 564 Course Notes.
33. Maudsley AA, Hilal SK. Biological Aspects of Na-23 Imaging. *Br Med Bull* 1984;40(2):165-&.
34. Shporer M, Civan MM. Effects of Temperature and Field Strength on NMR Relaxation Times of Na-23 in Frog Striated Muscle. *Biochimica Et Biophysica Acta* 1974;354(2):291-304.
35. Rong P, Regatte RR, Jerschow A. Clean demarcation of cartilage tissue Na-23 by inversion recovery. *Journal of Magnetic Resonance* 2008;193(2):207-209.
36. Borthakur A, Shapiro EM, Beers J, Kudchodkar S, Kneeland JB, Reddy R. Effect of IL-1 beta-induced macromolecular depletion on residual quadrupolar

- interaction in articular cartilage. *Journal of Magnetic Resonance Imaging* 2002;15(3):315-323.
37. Insko EK, Kaufman TH, Leigh JS, Reddy R. Sodium NMR evaluation of articular cartilage degradation. *Magnetic Resonance in Medicine* 1999;41(1):30-34.
  38. Jelicks LA, Paul PK, Obyrne E, Gupta RK. H-1, Na-23, and C-13 MR Spectroscopy of Cartilage Degradation in Vitro. *JMRI-J Magn Reson Imaging* 1993;3(4):565-568.
  39. Reddy R, Insko EK, Leigh JS. Triple quantum sodium imaging of articular cartilage. *Magnetic Resonance in Medicine* 1997;38(2):279-284.
  40. Borthakur A, Hancu I, Boada FE, Shen GX, Shapiro EM, Reddy R. In vivo triple quantum filtered twisted projection sodium MRI of human articular cartilage. *Journal of Magnetic Resonance* 1999;141(2):286-290.
  41. Hancu I, van der Maarel JRC, Boada FE. A model for the dynamics of spins 3/2 in biological media: Signal loss during radiofrequency excitation in triple-quantum-filtered sodium MRI. *Journal of Magnetic Resonance* 2000;147(2):179-191.
  42. Vandermaarel JRC. Relaxation of Spin 3/2 in a Nonzero Average Electric Field Gradient. *Chem Phys Lett* 1989;155(3):288-296.
  43. Granot J. Sodium Imaging of Human Body Organs and Extremities in Vivo. *Radiology* 1988;167(2):547-550.
  44. Wang LG, Wu Y, Chang G, Oesingmann N, Schweitzer ME, Jerschow A, Regatte RR. Rapid Isotropic 3D-Sodium MRI of the Knee Joint In Vivo at 7T. *Journal of Magnetic Resonance Imaging* 2009;30(3):606-614.
  45. Feinberg DA, Crooks LE, Kaufman L, Watts J, Arakawa M, Hoenninger JC. A Performance Comparison for Hydrogen and Sodium MRI. *Invest Radiol* 1985;20(6):S45-S45.
  46. Ra JB, Hilal SK, Cho ZH. A Method for In Vivo MR Imaging of the Short T2 Component of Na-23. *Magnetic Resonance in Medicine* 1986;3(2):296-302.
  47. Glover GH, Pauly JM, Bradshaw KM. B-11 Imaging with a 3 Dimensional Reconstruction Method. *JMRI-J Magn Reson Imaging* 1992;2(1):47-52.
  48. Boada FE, Gillen JS, Shen GX, Chang SY, Thulborn KR. Fast three dimensional sodium imaging. *Magnetic Resonance in Medicine* 1997;37(5):706-715.
  49. Jackson JI, Nishimura DG, Macovski A. Twisting Radial Lines with Application to Robust Magnetic Resonance Imaging of Irregular Flow. *Magnetic Resonance in Medicine* 1992;25(1):128-139.
  50. Jin J. *Electromagnetic Analysis and Design in Magnetic Resonance Imaging*. Boca Raton, Florida: CRC Press; 1999.
  51. Stobbe R, Beaulieu C. Sodium imaging optimization under specific absorption rate constraint. *Magnetic Resonance in Medicine* 2008;59(2):345-355.
  52. Hayes CE, Edelstein, W. A., Schenck J. F. . Radio frequency coils. In: S. R. Thomas RLD, editor. *NMR in Medicine*. New York: American Association Physicists Med; 1986. p 142-165.
  53. Hayes CE, Edelstein WA, Schenck JF, Mueller OM, Eash M. An Efficient, Highly Homogenous Radiofrequency Coil for Whole Body NMR Imaging at 1.5 T. *Journal of Magnetic Resonance* 1985;63(3):622-628.
  54. Leifer MC. Resonant modes of the birdcage coil. *Journal of Magnetic Resonance* 1997;124(1):51-60.

55. Frankel S. Reactance Networks for Coupling between Unbalanced and Balanced Circuits. *Proceedings of the IRE* 1941;29(9):486-493.
56. Staroswiecki E, Bangerter NK, Gurney PT, Grafendorfer T, Gold GE, Hargreaves BA. In Vivo Sodium Imaging of Human Patellar Cartilage With a 3D Cones Sequence at 3 T and 7 T. *Journal of Magnetic Resonance Imaging* 2010;32(2):446-451.
57. Eliav U, Navon G. Analysis of Double-Quantum Filtered NMR Spectra of Na-23 in Biological Tissues. *J Magn Reson Ser B* 1994;103(1):19-29.
58. Ling W, Regatte RR, Schweitzer ME, Jerschow A. Behavior of ordered sodium in enzymatically depleted cartilage tissue. *Magnetic Resonance in Medicine* 2006;56(5):1151-1155.
59. Stiller D. Pathology of Osteoarthritis: Histology, Histochemistry, and Ultrastructure. *Zentralblatt fuer Allgemeine Pathologie und Pathologische Anatomie* 1982;126(5-6):425-446.
60. Inerot S, Heinegard D, Olsson SE, Telhag H, Audell L. Proteoglycan Alterations during Developing Experimental Osteoarthritis in a Novel Hip-Joint Model. *J Orthop Res* 1991;9(5):658-673.
61. Reddy R, Li SC, Noyszewski EA, Kneeland JB, Leigh JS. In vivo sodium multiple quantum spectroscopy of human articular cartilage. *Magnetic Resonance in Medicine* 1997;38(2):207-214.
62. Stobbe R, Beaulieu C. Advantage of sampling density weighted apodization over postacquisition filtering apodization for sodium MRI of the human brain. *Magnetic Resonance in Medicine* 2008;60(4):981-986.
63. Woessner DE, Bansal N. Temporal characteristics of NMR signals from spin 3/2 nuclei of incompletely disordered systems. *Journal of Magnetic Resonance* 1998;133(1):21-35.
64. Perman WH, Turski PA, Houston LW, Glover GH, Hayes CE. Methodology of In Vivo Human Sodium MR Imaging at 1.5 T *Radiology* 1986;160(3):811-820.
65. Gold GE, Chen CA, Koo S, Hargreaves BA, Bangerter NK. Recent Advances in MRI of Articular Cartilage. *Am J Roentgenol* 2009;193(3):628-638.
66. Nagel AM, Laun FB, Weber MA, Matthies C, Semmler W, Schad LR. Sodium MRI Using a Density-Adapted 3D Radial Acquisition Technique. *Magnetic Resonance in Medicine* 2009;62(6):1565-1573.
67. Shepherd DET, Seedhom BB. Thickness of human articular cartilage in joints of the lower limb. *Ann Rheum Dis* 1999;58(1):27-34.
68. Alecci M, Romanzetti S, Kaffanke J, Celik A, Wegener HP, Shah NJ. Practical design of a 4 Tesla double-tuned RF surface coil for interleaved H-1 and Na-23 MRI of rat brain. *Journal of Magnetic Resonance* 2006;181(2):203-211.
69. Fitzsimmons JR, Beck BL, Brooker HR. Double Resonant Quadrature Birdcage. *Magnetic Resonance in Medicine* 1993;30(1):107-114.
70. Lu DF, Joseph PM. A Technique of Double Resonant Operation of F-19 and H-1 Quadrature Hybrid Birdcage Coils. *Magnetic Resonance in Medicine* 1991;19(1):180-185.
71. Shen GX, Boada FE, Thulborn KR. Dual-frequency, dual-quadrature, birdcage RF coil design with identical B-1 pattern for sodium and proton imaging of the human brain at 1.5 T. *Magnetic Resonance in Medicine* 1997;38(5):717-725.

72. Notohamiprodjo M, Horng A, Pietschmann MF, Muller PE, Horger W, Park J, Crispin A, del Olmo JRG, Weckbach S, Herrmann KA, Reiser MF, Glaser C. MRI of the Knee at 3T First Clinical Results With an Isotropic PDfs-Weighted 3D-TSE-Sequence. *Invest Radiol* 2009;44(9):585-597.
73. Bartha R, Megyesi JF, Watling CJ. Low-grade glioma: Correlation of short echo time H-1-MR spectroscopy with Na-23 MR imaging. *American Journal of Neuroradiology* 2008;29(3):464-470.
74. Jacobs MA, Ouwerkerk R, Kamel I, Bottomley PA, Bluemke DA, Kim HS. Proton, Diffusion-Weighted Imaging, and Sodium (Na-23) MRI of Uterine Leiomyomata after MR-Guided High-Intensity Focused Ultrasound: A Preliminary Study. *Journal of Magnetic Resonance Imaging* 2009;29(3):649-656.
75. Ouwerkerk R, Jacobs MA, Macura KJ, Wolff AC, Stearns V, Mezban SD, Khouri NF, Bluemke DA, Bottomley PA. Elevated tissue sodium concentration in malignant breast lesions detected with non-invasive Na-23 MRI. *Breast Cancer Res Treat* 2007;106(2):151-160.
76. Schepkin VD, Chenevert TL, Kuszpit K. Sodium and proton diffusion MRI as biomarkers for early therapeutic response in subcutaneous tumors. *Magn Reson Imaging* 2006;24(3):273-278.